

**EMG-Based Human-In-The-Loop Bayesian Optimization to Assist  
Hip-Centric Activities**

BY

SALVADOR ECHEVESTE  
PhD, 2025

THESIS

Submitted as partial fulfillment of the requirements  
for the degree of Doctor of Philosophy in Mechanical Engineering  
in the Graduate College of the  
University of Illinois at Chicago, 2025

Chicago, Illinois

Defense Committee:

**Pranav A. Bhounsule**, Chair and Advisor  
**Myunghee Kim**, Mechanical Engineering  
**James Patton**, Biomedical Engineering  
**Ming Wu**, Biomedical Engineering  
**Ernesto Hernandez Hinojosa**, University of Michigan

Copyright by

Salvador Echeveste

2025

*A mis padres.*

*por el inmenso sacrificio de venir a este país con la esperanza de brindarnos una vida mejor. Con este trabajo espero solamente empezar a saldar esa deuda y verlos orgullosos. Los quiero con todo mi corazón.*

*To my brother.*

*Thank you for being my rock throughout this journey. Your belief in me never wavered, not even when I doubted myself. You reminded me of who I am and what I'm capable of. You've always had my back, and that means more to me than words can say.*

*To Karina,*

*Your love has been my light and refuge. Thank you for your patience, for always encouraging me, and for standing by my side through the highs and lows. I'm endlessly grateful for your support and presence in my life.*

## **ACKNOWLEDGMENTS**

I am deeply grateful to my advisor for their unwavering support throughout this journey. Thank you for taking a chance on me, for bringing me along to Chicago, and for your remarkable patience as I navigated the twists and turns of this project. Your guidance has shaped not only this work but also the researcher I've become.

This work would not have been possible without the incredible community that has surrounded me. To my friends Martin, Jamika, Eric, Kris, Kelcee, Alex, Justin, and Ellen; thank you for keeping me grounded and for reminding me there's life beyond the lab. Your friendship has been my anchor through it all.

I'm fortunate to have worked alongside brilliant colleagues who made even the longest days in the trenches enjoyable. To Josh, Daniel, Ernesto, Chun-Ming, Safwan, Subbu, Jim, Ragib, Simone, Venkata, Abhishek, Jeremy, and Chinonso; thank you for the collaborative spirit and for making our workspace feel less like an office and more like a second home. Each of you has left your mark on this work in ways both big and small.

To my friends near and far who have cheered me on from the sidelines: your encouragement has meant more than you know.

SE

## **PREFACE**

All procedures involving human participants were conducted in strict accordance with the principles set forth in the Declaration of Helsinki. Ethical approval for this research was granted by the Institutional Review Board of the University of Illinois at Chicago under protocol number STUDY 2022-1022.

Salvador Echeveste  
September 9, 2025

## CONTRIBUTION OF AUTHORS

**Work 1: Optimal Swing Assistance Using a Hip Exoskeleton: Comparing Simulations with Hardware Implementation (Chapter 3)**

**Ernesto Hernandez Hinojosa's Contributions**

- **Conceptualization:** Assisted with problem formulation
  - **Software & Hardware:**
    - Discrete optimization programming
    - Control system implementation (Raspberry Pi, CAN bus)
  - **Analysis & Writing:**
    - Results interpretation
    - Contributed to manuscript sections
- 

**Work 2: Electromyography-Based Human-in-the-Loop Bayesian Optimization to Assist Free Leg Swinging (Chapter 4)**

**Pranav A. Bhounsule's Contributions**

- **Supervision & Project Administration:**
  - Project oversight and mentorship
  - Research direction and timeline management
- **Resources & Funding:**

## **CONTRIBUTION OF AUTHORS (Continued)**

- Lab facility management and resource coordination
  - Grant acquisition and budget management
  - **Writing:** Review and editing of manuscript
- 

### **Work 3: Enhancing Hip Exoskeleton Tuning Performance with Machine Learning (Chapter 5)**

#### **Md Safwan Mondal's Contributions**

- **Software:** Classification model development (KNN, SVM, Logistic Regression)
- **Validation:** Cross-validation implementation
- **Writing:** Assisted with manuscript preparation

#### **Subramanian Ramasamy's Contributions**

- **Data Processing:** Synthetic data generation
- **Analysis:** Model training and validation
- **Writing:** Assisted with manuscript preparation

#### **Pranav A. Bhounsule's Contributions**

- **Supervision & Project Administration:** Project oversight and research coordination
  - **Resources:** Resource management and lab facilities
  - **Writing:** Review and editing of manuscript
-

## **CONTRIBUTION OF AUTHORS (Continued)**

**Work 4: Tuning Squatting Controllers for a Hip Exoskeleton Using EMG-Based Bayesian Optimization (Chapter 6)**

### **Akshay Subramanian's Contributions**

- **Methodology:** Assisted with Bayesian optimization framework design
- **Writing:** Assisted with manuscript preparation
- **Dissemination:** Assisted with presentation preparation

### **Joshua Zatz's Contributions**

- **Control Development:** Assisted with stiffness control strategy development
- **Methodology:** Assisted with experimental protocol design
- **Writing:** Assisted with manuscript preparation

### **Pranav A. Bhounsule's Contributions**

- **Supervision & Project Administration:** Project guidance, coordination, and management
  - **Resources:** Lab facility management
  - **Writing:** Review and editing of manuscript
-

## TABLE OF CONTENTS

<u>CHAPTER</u>		<u>PAGE</u>
<b>1 INTRODUCTION . . . . .</b>		<b>1</b>
1.1 Context and Motivation . . . . .		1
1.1.1 The Growing Need for Mobility Assistance . . . . .		1
1.1.2 The Promise and Limitations of Exoskeleton Technology . . . . .		3
1.1.3 The Personalization Imperative . . . . .		4
1.1.4 Critical Limitations of Current Approaches . . . . .		6
1.1.5 Surface Electromyography: A Path to Rapid Personalization . . . . .		7
1.2 Research Questions and Objectives . . . . .		9
1.2.1 Research Questions . . . . .		9
1.2.2 Thesis Statement . . . . .		9
1.2.3 Specific Aims . . . . .		10
1.3 Significance and Contributions . . . . .		10
1.4 Dissertation Organization . . . . .		12
<b>2 BACKGROUND AND LITERATURE REVIEW . . . . .</b>		<b>15</b>
2.1 The Grand Challenge: Why Exoskeletons Need Personalization . . . . .		15
2.1.1 The Fallacy of Universal Assistance . . . . .		15
2.1.2 Neuromuscular Individuality: The Biological Basis of Variability . . . . .		16
2.1.3 The Physical Human-Robot Interface: Where Mechanics Meet Biology . . . . .		16
2.1.4 Clinical Populations: When Pathology Amplifies Variability . . . . .		17
2.1.5 The Assistance Landscape: Conceptualizing Personalization . . . . .		18
2.2 The Evolution of Personalization Approaches . . . . .		18
2.2.1 The Promise and Peril of Predictive Simulation . . . . .		18
2.2.2 Strategic Simplification: Isolating Core Dynamics . . . . .		19
2.2.3 The Failure of Expert Intuition . . . . .		20
2.2.4 The Shift to Data: Embracing Empirical Optimization . . . . .		20
2.2.5 From Prediction to Partnership . . . . .		20
2.3 Control Architectures for Human–Robot Coordination . . . . .		21
2.3.1 The Limitations of Classical Control Approaches . . . . .		21
2.3.2 Impedance Control as a Unifying Framework . . . . .		22
2.3.3 Variable Impedance and the Personalization Challenge . . . . .		23
2.4 Temporal Constraints in HIL Optimization . . . . .		24
2.4.1 The Metabolic Cost Bottleneck . . . . .		24
2.4.2 EMG as a Rapid Alternative . . . . .		25
2.4.3 Achieving Rapid Convergence . . . . .		25
2.5 Signal Reliability Challenges . . . . .		26

## TABLE OF CONTENTS (Continued)

<u>CHAPTER</u>		<u>PAGE</u>
2.5.1	Signal Quality Challenges . . . . .	26
2.5.2	Sample-Efficient Search . . . . .	27
2.5.3	Intelligent Initialization . . . . .	28
2.6	Beyond Physiology: Incorporating User Preference . . . . .	28
2.6.1	Limitations of Single-Objective Optimization . . . . .	28
2.6.2	Multi-Objective Frameworks . . . . .	29
2.6.3	Integrated Multi-Objective Frameworks . . . . .	29
2.7	Current State and Future Directions . . . . .	30
<b>3</b>	<b>OPTIMAL SWING ASSISTANCE USING A HIP EXOSKELETON: COMPARING SIMULATIONS WITH HARDWARE IMPLEMENTATION . . . . .</b>	<b>33</b>
3.1	Overview . . . . .	33
3.2	Methods . . . . .	35
3.2.1	Simulation Framework . . . . .	35
3.2.1.1	Stage 1: Pendulum Model for Profile Shape Discovery . . . . .	35
3.2.1.2	Stage 2: Hill-Type Muscle Model for Parameter Refinement . . . . .	35
3.2.2	Profile Parameterization . . . . .	36
3.2.3	Hardware Implementation . . . . .	38
3.2.3.1	Experimental Platform . . . . .	38
3.2.3.2	Experimental Protocol . . . . .	38
3.3	Results . . . . .	38
3.3.1	Simulation Predictions . . . . .	38
3.3.2	Hardware Performance . . . . .	39
3.3.2.1	EMG Reduction Performance . . . . .	39
3.3.3	Key Comparative Insights . . . . .	39
3.3.3.1	Frequency-Dependent Performance Reversal . . . . .	39
3.3.3.2	Work Type Effects . . . . .	40
3.3.3.3	Model Complexity Impact . . . . .	40
3.4	Discussion . . . . .	41
3.4.1	Simulation-to-Hardware Gap Analysis . . . . .	41
3.4.2	Design Principles for Hardware Implementation . . . . .	41
3.4.3	Limitations and Future Directions . . . . .	42
3.5	Conclusion . . . . .	42
<b>4</b>	<b>EMG-BASED HUMAN-IN-THE-LOOP BAYESIAN OPTIMIZATION FRAMEWORK . . . . .</b>	<b>44</b>
4.1	Overview . . . . .	44
4.2	Methods . . . . .	46
4.2.1	Hip Exoskeleton Device . . . . .	46
4.2.2	EMG Data . . . . .	48
4.2.2.1	Sensor Data Processing . . . . .	48

## TABLE OF CONTENTS (Continued)

<u>CHAPTER</u>		<u>PAGE</u>
4.2.2.2	Data Convergence . . . . .	50
4.2.3	Experimental Protocol . . . . .	54
4.2.3.1	Acclimation . . . . .	56
4.2.3.2	HIL Optimization . . . . .	56
4.2.3.3	Validation . . . . .	60
4.3	Results . . . . .	62
4.4	Discussion . . . . .	64
4.5	Conclusion . . . . .	66
<b>5</b>	<b>MACHINE LEARNING ENHANCEMENT OF BAYESIAN OPTIMIZATION INITIALIZATION . . . . .</b>	<b>67</b>
5.1	Overview . . . . .	67
5.2	Methods . . . . .	69
5.2.1	Data Foundation . . . . .	69
5.2.2	Data Processing Pipeline . . . . .	70
5.2.2.1	Population-Informed Normalization . . . . .	71
5.2.2.2	Feature Selection via Regularization . . . . .	72
5.2.2.3	Dimensionality Reduction . . . . .	73
5.2.2.4	Outlier Detection and Mitigation . . . . .	73
5.2.2.5	Controlled Data Synthesis . . . . .	74
5.2.3	Classification Model Development . . . . .	74
5.2.4	Experimental Validation . . . . .	75
5.3	Results . . . . .	76
5.3.1	Data Synthesis Validation . . . . .	76
5.3.2	Classification Performance . . . . .	76
5.3.3	Optimization Enhancement . . . . .	77
5.4	Discussion . . . . .	77
5.4.1	Bridging Individual Differences Through Data . . . . .	77
5.4.2	Data Synthesis as an Enabling Technology . . . . .	78
5.4.3	Integration with HIL Optimization . . . . .	79
5.4.4	Limitations and Extensions . . . . .	80
5.5	Conclusion . . . . .	80
<b>6</b>	<b>TUNING SQUATTING CONTROLLERS FOR A HIP EXOSKELETON USING EMG-BASED BAYESIAN OPTIMIZATION . . . . .</b>	<b>82</b>
6.1	Overview . . . . .	82
6.2	Methods . . . . .	83
6.2.1	System Overview . . . . .	83
6.2.2	Hip Exoskeleton Device . . . . .	85
6.2.3	Control Architecture . . . . .	88
6.2.4	Stiffness Control Formulation . . . . .	88
6.2.5	EMG Data . . . . .	89

## TABLE OF CONTENTS (Continued)

<u>CHAPTER</u>		<u>PAGE</u>
6.2.6	Bayesian Optimization . . . . .	91
6.2.7	Experimental Protocol . . . . .	92
6.3	Results . . . . .	93
6.4	Discussion . . . . .	98
6.5	Conclusion . . . . .	99
<b>7</b>	<b>EMG SIGNAL ENHANCEMENT VIA MULTI-OBJECTIVE OPTIMIZATION OF HANKEL-BASED BAYESIAN LEARNING . . . . .</b>	<b>100</b>
7.1	Overview . . . . .	100
7.2	Methods . . . . .	102
7.2.1	Data Acquisition . . . . .	102
7.2.2	Hankel-based Signal Reconstruction . . . . .	103
7.2.3	Regularized Estimation via Bayesian Linear Regression . . . . .	104
7.2.4	Signal Fusion . . . . .	104
7.2.5	Multi-objective Bayesian Optimization . . . . .	105
7.2.6	Windowed Makima Median Smoother . . . . .	105
7.3	Results . . . . .	105
7.4	Discussion . . . . .	106
7.5	Conclusions . . . . .	112
<b>8</b>	<b>ADAPTIVE WALKING CONTROLLERS: A COMPREHENSIVE SIMULATION STUDY OF IMPEDANCE-BASED ASSISTIVE STRATEGIES . . . . .</b>	<b>113</b>
8.1	Overview . . . . .	113
8.2	Methods . . . . .	114
8.2.0.1	Experimental Data . . . . .	114
8.2.1	Normalize Angles and Velocities . . . . .	115
8.2.1.1	Angle Normalization . . . . .	115
8.2.1.2	Velocity Computation and Normalization . . . . .	115
8.2.1.3	Energy Metric Calculation . . . . .	116
8.2.2	Define Controller Architectures . . . . .	116
8.2.2.1	Basic Per-Direction Controller . . . . .	116
8.2.2.2	Normalized Gain Controller . . . . .	117
8.2.2.3	Energy-Based Adaptive Controller . . . . .	117
8.2.2.4	Phase-Based Adaptive Controller . . . . .	118
8.2.2.5	Variable Stiffness Controllers . . . . .	118
8.2.3	Optimize Controller Parameters . . . . .	119
8.2.3.1	Cost Function . . . . .	119
8.2.3.2	Bayesian Optimization . . . . .	120
8.2.4	Evaluate Assistance Metrics . . . . .	120
8.2.4.1	Mechanical Power Proxy Reduction . . . . .	120
8.2.4.2	Torque Smoothness . . . . .	121

## TABLE OF CONTENTS (Continued)

<u>CHAPTER</u>		<u>PAGE</u>
8.3	Results . . . . .	121
8.3.1	Controller Performance (Tested Only) . . . . .	121
8.3.2	Optimized Parameters . . . . .	123
8.3.3	Torque Profile Notes . . . . .	124
8.4	Discussion . . . . .	124
8.4.1	Implications for Assistive Device Design . . . . .	124
8.4.2	Biological Plausibility . . . . .	125
8.4.3	Design Trade-offs and Practical Considerations . . . . .	125
8.4.4	Future Research Directions . . . . .	126
8.5	Conclusion . . . . .	126
<b>9</b>	<b>SYSTEMATIC EVALUATION OF EMG-BASED COST FUNCTIONS FOR METABOLIC ENERGY APPROXIMATION DURING HUMAN LOCOMOTION . . . . .</b>	<b>129</b>
9.1	Overview . . . . .	129
9.2	Methods . . . . .	131
9.2.1	Dataset and Protocol . . . . .	131
9.2.2	EMG Processing and Normalization . . . . .	131
9.2.3	EMG-Based Cost Functions . . . . .	132
9.2.3.1	Notation . . . . .	132
9.2.3.2	Definitions . . . . .	133
9.2.4	Primary Outcome and Evaluation . . . . .	134
9.2.5	Software and Reproducibility . . . . .	134
9.3	Results . . . . .	135
9.3.1	Within-Subject Accuracy . . . . .	135
9.3.2	Model Fit and Composite Ranking . . . . .	135
9.3.3	Robustness and Reliability . . . . .	136
9.3.4	Practical Interpretation . . . . .	137
9.4	Discussion . . . . .	138
9.4.1	Principal Findings . . . . .	138
9.4.2	Implications for Tuning and Clinical Use . . . . .	138
9.4.3	Interpreting Correlation and Fit . . . . .	139
9.4.4	Limitations and Next Steps . . . . .	139
9.4.5	Conclusion . . . . .	139
<b>10</b>	<b>MULTI-OBJECTIVE BAYESIAN OPTIMIZATION OF VARIABLE IMPEDANCE CONTROL FOR HIP EXOSKELETONS USING EMG AND HUMAN PREFERENCE . . . . .</b>	<b>141</b>
10.1	Overview . . . . .	141
10.2	Methods . . . . .	143
10.2.1	System Architecture . . . . .	143
10.2.2	Variable Impedance Control Implementation . . . . .	145

## TABLE OF CONTENTS (Continued)

<u>CHAPTER</u>		<u>PAGE</u>
10.2.3	Multi-Objective Optimization Framework . . . . .	147
10.2.3.1	Objective Function Formulation . . . . .	147
10.2.3.2	EMG Signal Processing Pipeline . . . . .	149
10.2.3.3	Heteroscedastic Gaussian Process Models . . . . .	150
10.2.3.4	Expected Hypervolume Improvement Acquisition . . . . .	150
10.2.4	Experimental Protocol . . . . .	151
10.2.4.1	Participants . . . . .	151
10.2.4.2	Experimental Procedure . . . . .	151
10.2.4.3	Data Collection and Analysis . . . . .	153
10.3	Results . . . . .	153
10.3.1	Optimization Performance and Convergence . . . . .	153
10.3.2	Physiological and Perceptual Outcomes . . . . .	155
10.3.3	Controller Characteristics and Parameter Analysis . . . . .	157
10.4	Discussion . . . . .	160
10.4.1	Clinical and Methodological Implications . . . . .	160
10.4.2	Biomechanical Insights and Future Directions . . . . .	161
10.5	Conclusion . . . . .	162
<b>11 CONCLUSION</b>		164
<b>CITED LITERATURE</b>		167
<b>VITA</b>		182

## LIST OF TABLES

<u>TABLE</u>		<u>PAGE</u>
I	PREDICTED PERCENT REDUCTION IN BIOLOGICAL TORQUE FROM SIMULATION . . . . .	39
II	PERCENT CHANGE IN EMG ACTIVITY WITH ASSISTANCE VS. NO DEVICE . . . . .	40
III	BORG VALUE COMPARISON AGAINST BASELINES FOR VALIDATION . . . . .	65
IV	ANTHROPOMETRIC PREDICTIVE FEATURES USED FOR CONTROLLER PARAMETER PREDICTION . . . . .	72
V	EXPERIMENTAL PROTOCOL SUMMARY . . . . .	93
VI	CONTROLLER PERFORMANCE COMPARISON . . . . .	123
VII	CONDENSED REFERENCE FOR EMG COST FUNCTIONS . . . . .	135
VIII	OPTIMIZED CONTROL PARAMETERS BY TASK . . . . .	157
IX	SENSITIVITY ANALYSIS RESULTS . . . . .	159

## LIST OF FIGURES

<u>FIGURE</u>		<u>PAGE</u>
1	Antagonistic Hill-type muscle model for hip flexion/extension, with rectus femoris (positive torque) and biceps femoris (negative torque). . . . .	36
2	Torque-angle profiles for all three types of controllers (RMS, PKK, DISMM) across the swing. These serve as the basis for both simulation validation and hardware implementation. . . . .	37
3	Custom hip exoskeleton used for hardware experiments, showing motor housing, straps, rotary encoder, and safety stops. . . . .	37
4	Overview of EMG-HIL Bayesian Optimization. A) Swinging setup (device, sensors, structure). B) EMG processing pipeline (details in Figure 6). C) Bayesian optimization loop tuning four parameters using two cost functions. D) Controller shaping via Bézier parameters. . . . .	46
5	A) An illustration of the exoskeleton device detailing all the main components. B) An overview of the controller constructs a relationship between torque and angle using segmented Bézier curves. The location of the four control points. Control points P1 and P2 are dependent on $P_f$ and $L_f$ while P3 and P4 are dependent on $P_b$ and $L_b$ . The torque functions for forward and backward actuation are represented as $\tau_f$ and $\tau_b$ respectively.	47
6	Signal processing includes A) a bandpass filter with a high pass of 20Hz and a low pass of 450 Hz plus an outlier replacement of extreme values beyond 3 standard deviations using a modified Akima cubic Hermite interpolation; B) rectification by taking the absolute value and subtracting the mean value of the previous signal; C) a moving max and discretization filter to outline the shape of the signal; D) a moving average filter to smooth noise followed by normalization against the MVC value for each sensor; E) partitioning the data into separate swings; F) and a data aggregation process using an averaged representation of the epochs produces a single output representation. . . . .	51

## LIST OF FIGURES (Continued)

<u>FIGURE</u>	<u>PAGE</u>
7 This figure presents a comprehensive view of the swing controller concerning both controller parameters and torque profiles. A,B) Plots displaying the spatial distribution of controller parameters during the slow swing and fast swing. The x-axis represents the location, and the y-axis denotes the magnitude. C,D) showcasing the torque profile for the slow and fast swing, with the x-axis indicating the swing phase as a percentage, and the y-axis representing the weight-normalized torque. . . . .	55
8 Three samples of the surrogate and acquisition function optimization landscapes from Bayesian. The h variable represents the cost function, P and L are the two parameters tuned, and EI is the expected improvement for each parameter set. Lower values are favorable for the Gaussian process model and higher values are favorable for the expected improvement function. . . . .	61
9 Condition comparison results from the validation phase. The condition averages of the EMG performance metric are represented by the bar graph. The standard deviation is shown by whiskers. Percent changes between tests with three baseline conditions and tests with optimal control are shown above the horizontal brackets. . . . .	63
10 The convergence data for each subject is represented as a bold average line with dotted lines showing the standard deviation. The variable g represents the sum of the derivative of the running average for the four sensors across all trials of a subject. The star indicates the time when a steady state is reached on average. . . . .	64
11 Overview of EMG-HIL Bayesian Optimization established in precursor work. . . . .	70
12 Left) An illustration of the exoskeleton device used, highlighting important features. Right) An illustration of the relationship between torque and angle. . . . .	71
13 An overview of the machine learning pipeline and its application in the initialization of Bayesian HIL optimization. Matrix dimensions are indicated in parentheses, and $P_f$ , $P_b$ , $L_f$ , and $L_b$ refer to the control parameters.	73
14 Performance comparison between the two controllers tuned with and without the developed method against a baseline of no device. . . . .	78

## LIST OF FIGURES (Continued)

<u>FIGURE</u>		<u>PAGE</u>
15	System data flow for EMG-based Bayesian optimization, showing acquisition, processing, and parameter tuning components. . . . .	84
16	Hip exoskeleton highlighting principal features, including the 24 V BLDC motor for variable stiffness control, adjustable straps for a secure fit, and rigid plastic braces. The design supports hip flexion and extension during squatting. . . . .	86
17	Schematic of the control system. A high-level finite state machine manages forward, backward, and resting states, while the low-level controller sends torque commands according to the control law. . . . .	87
18	EMG processing workflow: filtering, rectification, smoothing, and normalization with MVC values, leading to cost functions for the forward and backward squat phases. . . . .	90
19	Performance metrics (metabolic cost, muscle EMG activity, and Borg ratings) across no exoskeleton, unpowered exoskeleton, and optimized controller conditions. Percentage reductions with the optimized controller are shown; error bars indicate standard deviations. . . . .	94
20	Heat map of control parameter combinations versus cost across all subjects. Stars mark parameter sets that achieved the minimum cost during Bayesian optimization. . . . .	95
21	Convergence plots of normalized best cost by trial for each subject, demonstrating rapid convergence of the optimization algorithm. . . . .	96
22	Kinematic profiles during squatting: (a) joint angle vs. normalized phase, (b) angular velocity vs. phase, (c) control torque vs. phase, and (d) power vs. phase, showing assistance synchronized with movement. . . . .	97
23	Schematic of the EMG enhancement and optimization workflow. Raw EMG is denoised via an optimized process involving Hankel-SVD, prediction by a Bayesian Koopman model, weighted combination, and smoothing. The asterisk (*) indicates that the five parameters ( $d$ , $r$ , $\sigma$ , $\tau$ , $w$ ) are optimized via multi-objective Bayesian optimization, while the smoother window length ( $s$ ) is optimized independently. . . . .	106

## LIST OF FIGURES (Continued)

<u>FIGURE</u>	<u>PAGE</u>
24 Processing stages for one EMG channel. Top: raw signal to fused output (dashed). Bottom: fused output to Makima-median smoothing. Note that the fused output retains physiological features while reducing noise, and the final smoothing removes residual high-frequency artifacts. . . . .	107
25 Mean and standard deviation comparison of control (gray) and experimental (blue) on SGM (left) and normalized joint metric (right) across all subjects and activities. Control refers to the standard EMG processing pipeline, while Experimental refers to our proposed Hankel-Bayesian optimization framework. . . . .	108
26 Scatter of SNR vs. SSIM for control (gray) and our method (blue). Dashed red lines are linear fits showing strong negative correlation in control ( $r=-0.64$ ) versus near zero in our pipeline ( $r=0.01$ ). . . . .	109
27 Muscle-specific mean $\pm$ standard deviation for control (gray) and experimental (blue) on SGM (left) and joint metric (right) for RF: rectus femoris, BF: biceps femoris, GN: gastrocnemius, and GM: gluteus maximus. . . . .	110
28 Activity-specific mean and standard deviation for walking and squatting, comparing control and experimental methods on SGM (left) and joint metric (right). . . . .	111
29 Reference gait profiles used for controller design and evaluation. Left: mean hip flexion angle with a shaded min–max range across all cycles. Right (red): mean hip flexion moment with a shaded min–max range. The horizontal axis is the normalized gait cycle (0–100%), and vertical axes are angle (°) and moment (N m), respectively. These summaries provide a compact baseline against which controller torques are compared, while the range bands visualize inter-cycle variability. . . . .	122
30 Pareto scatter of mechanical power proxy reduction (horizontal axis, %) versus smoothness $S$ (vertical axis, $s^2/Nm$ ; higher is smoother). All controllers are plotted as black markers. BVSC, Basic+Phase, and Normalized Gain controllers are color-coded and labeled. Rightward points indicate greater proxy reduction; upward points indicate smoother torque.	127

## LIST OF FIGURES (Continued)

<u>FIGURE</u>	<u>PAGE</u>
31 Time-series comparisons of biological torque (black), controller torque (green), and net torque (red; biological minus controller) for 3 controllers (left to right: BVSC, Basic+Phase, and Normalized Gain). Each panel spans one full cycle ( $\Delta t = 0.01$ s). The legend is shown only in the right-most panel and uses a reduced font for compactness. These plots provide a visual check that optimized controllers reduce the magnitude of net torque while preserving smoothness. . . . .	128
32 Controller torque across normalized angle [0, 1] for 3 controllers: Bézier Variable Stiffness (BVSC), Basic per-direction with phase-shifted reference, and Normalized Gain controller. Forward gait samples (based on sign of normalized angular velocity) are plotted as teal circles and backward samples as brick-red x markers. Axes are harmonized by plotting normalized angle [0, 1] for all panels; torque in Nm. This figure emphasizes the directional asymmetry and how each controller's torque output varies over the gait cycle. . . . .	128
33 Which EMG cost functions best approximate metabolic cost? Core findings. (A) Mean within-subject Pearson correlations ( $r$ ) between each cost function and metabolic power across 12 participants and 30 conditions per participant; markers show means and whiskers show 95% bootstrap confidence intervals. The simple unweighted sum (C5) is the top performer with $r = 0.762$ and 95% CI [0.550, 0.914]. Fourteen of 16 functions (87.5%) show positive correlations with CI lower bound $> 0$ . (B) Performance trade-off between mean correlation (x-axis) and adjusted $R^2$ from an OLS fit of metabolic power on each cost (y-axis). Square markers indicate the top five by the composite score; C5 aligns with the optimal trade-off between model simplicity and performance and also attains the best adjusted $R^2$ ( $R_{\text{adj}}^2 = 0.190$ ). (C) Overall ranking (top 10) by a composite score that aggregates ranks for correlation, adjusted $R^2$ , and information criteria. The top five are {C5, C7, C2, C1, C3}. . . . .	136

## LIST OF FIGURES (Continued)

<u>FIGURE</u>	<u>PAGE</u>
34 Robustness and stability across subjects and metrics. (A) Subject-by-function correlation heatmap (diverging RdBu scale): warm colors indicate stronger positive association with metabolic power. The consistently high values in the C5 column indicate broad subject-level robustness. (B) Top-5 functions (by composite score) shown as violins with overlaid per-subject points; distribution shapes and jittered dots reveal between-subject spread, with C5 exhibiting a high central tendency and comparatively compact spread relative to peers. (C) Between-subject reliability (ICC). Most top performers show good reliability ( $ICC \gtrsim 0.75$ ). The highest ICC is observed for C10 ( $ICC = 0.873$ ), while C11 is lowest among these ( $ICC = 0.592$ ); the winning function C5 maintains high reliability suitable for deployment. . . . .	137
35 Framework for multi-objective optimization of assistive device control. (A) Depiction of a subject wearing the device while performing the two activities of the study. EMG signals are collected from both legs and verbal preference score is recorded. (B) Heteroscedastic Gaussian process models of both objective functions, with mean surfaces and input-dependent variance illustrated. (C) Multi-objective optimization process using Expected Hypervolume Improvement (EHVI) to select next evaluation points that maximize information gain about the Pareto front. (D) Resulting variable stiffness control profiles showing task-specific stiffness modulation strategies discovered through optimization, with distinct patterns for forward and backward phases of movement. . . . .	144
36 Variable impedance control architecture and resulting behavior. ( <b>Left:</b> ) Control system block diagram showing signal flow from sensory input through impedance modulation to motor commands. Key modules include: (1) Kalman filter for state estimation with process noise $\mathbf{Q} = \text{diag}([10^{-2}, 10^{-1}])$ and measurement noise $\mathbf{R} = \text{diag}([2, 5]) \text{ rad}^2$ ; (2) Phase detection finite state machine with hysteresis thresholds; (3) Bézier curve generation for smooth stiffness profiles; (4) Safety saturation and filtering. ( <b>Right:</b> ) An example of controller behavior with the parameterized variable stiffness curve and the equivalent torque curve. An important aspect to note is that walking and squatting controllers have separate control parameters. . . . .	148

## LIST OF FIGURES (Continued)

<u>FIGURE</u>	<u>PAGE</u>
37 Multi-objective optimization results demonstrating Pareto front evolution and convergence characteristics. <b>(A,B)</b> Final Pareto fronts for walking and squatting activities showing trade-offs between normalized EMG cost and user preference score. Each gray point represents one evaluated parameter combination; green curve and shaded region indicates mean and standard deviation of the Pareto fronts for all subjects. <b>(C,D)</b> Convergence of best observed values for both objectives across optimization iterations. Shaded regions show $\pm 1$ SD across subjects. . . . .	154
38 Learned heteroscedastic noise models revealing input-dependent measurement variability. <b>(A)</b> The variance of EMG across a PCA-derived representation of stiffness level and stiffness duration. <b>(B)</b> Preference noise patterns across the same PCA-derived stiffness level and stiffness duration representatives. . . . .	155
39 Physiological and perceptual outcomes for walking (left panels, A–C) and squatting (right panels, D–F) under three conditions: NE = No Exoskeleton, ZA = Zero Assistance (unpowered exoskeleton), and OP = Optimized assistance. <b>(A,D)</b> Metabolic cost in J/kg; <b>(B,E)</b> Integrated muscle activation via EMG as %MVC; <b>(C,F)</b> Perceived exertion on the Borg scale (6-20). Bars represent mean values with error bars showing $\pm 1$ SD. Black brackets indicate pairwise comparisons with percentage change and p-values. For walking, effect sizes (Cohen's d) ranged from 0.98-2.41 for significant comparisons. For squatting, effect sizes ranged from 0.93-1.84. Note the task-specific pattern where walking shows consistent improvements across all metrics, while squatting demonstrates dissociation between EMG and perceived exertion responses. . . . .	156
40 Temporal characteristics of optimized controllers across movement cycles. <b>(A,D)</b> Variable stiffness profiles for across one movement cycle for walking and squatting. An overlayed single repetition of the movement angle is also shown. <b>(B,E)</b> The equivalent walking and squatting controllers calculated by the finite state machine with state and activity dependent desired set points <b>(C,F)</b> Corresponding power profiles demonstrating task-specific energy exchange patterns. For each, solid lines show the mean of all subjects with $\pm 1$ SD shading. . . . .	158

## LIST OF ABBREVIATIONS

BF	biceps femoris
BLDC	Brushless DC (motor)
BORG	Borg Rating of Perceived Exertion (Borg scale)
BVSC	Bézier Variable Stiffness Control
EI	Expected Improvement (acquisition function)
EHVI	Expected Hypervolume Improvement (acquisition)
EMG	Electromyography
GN	gastrocnemius (medial gastrocnemius)
GM	gluteus maximus
HIL	Human-in-the-Loop
ICC	Intraclass Correlation Coefficient (between-subject reliability)
MVC	Maximum Voluntary Contraction
PCA	Principal Component Analysis
PDF	Probability density function
RF	rectus femoris
RMS	Root Mean Square

## **LIST OF ABBREVIATIONS (Continued)**

SNR	Signal-to-Noise Ratio
SVD	Singular Value Decomposition
SVM	Support Vector Machine

## NOTATIONS

Bold lowercase letters are used to denote the vectors and bold uppercase letters for matrices.

The following mathematical notations are used throughout this thesis:

$ x $	the absolute value of a scalar $x$
$\mathbf{x}, \mathbf{X}$	bold lowercase $\mathbf{x}$ denotes a vector; bold uppercase $\mathbf{X}$ denotes a matrix
$x(k)$	the value (sample/element) of a discrete-time signal or vector at index $k$
$\ \mathbf{x}\ _p$	the $\ell_p$ -norm of $\mathbf{x}$ , defined as $(\sum_k  x(k) ^p)^{1/p}$
$\in$	set membership operator
$\sim$	distributed as
$\theta$	joint angle (hip flexion/extension)
$\dot{\theta}$	angular velocity
$\theta_d$	desired/reference angle
$\theta_{\text{norm}}$	normalized joint angle in range $[0, 1]$
$\tau$	applied torque
$\tau_f, \tau_b$	forward and backward torque functions
$K$	stiffness coefficient/gain
$K_f, K_b$	forward and backward stiffness gains
$B$	damping coefficient

## NOTATIONS (Continued)

$B_f, B_b$	forward and backward damping coefficients
$P_f, P_b$	forward and backward peak magnitude parameters
$L_f, L_b$	forward and backward location parameters
$M_f, M_b$	forward and backward magnitude parameters (Bézier)
$d_f, d_b$	forward and backward duration parameters (Bézier)
$m_i(t)$	normalized EMG envelope for muscle $i$ at time $t$
$M_n^d$	EMG muscle model for direction $d$ and sensor $n$
$h_f, h_b$	forward and backward EMG cost functions
$\text{SUM}_i$	sum of EMG samples for muscle $i$
$\text{RMS}_i$	root mean square of EMG for muscle $i$
$f(\mathbf{x})$	objective function
$f_1, f_2$	multi-objective functions (EMG cost, user preference)
$\mathbf{x}^*$	optimal parameter vector
$\text{EI}(x)$	Expected Improvement acquisition function
$\text{EHVI}(x)$	Expected Hypervolume Improvement
$m(x)$	mean function of Gaussian process
$k(x, x')$	covariance/kernel function
$\mathbf{K}$	covariance matrix

## NOTATIONS (Continued)

$\sigma_f^2$	signal variance
$\ell_i$	length-scale parameter for dimension $i$
<b>H</b>	Hankel matrix
<b>U, Σ, V</b>	singular value decomposition matrices
<b>A</b>	state transition matrix
$\mu$	mean value
$\sigma^2$	variance
$\text{cov}(\cdot, \cdot)$	covariance operator
$\Phi(\cdot)$	cumulative distribution function of standard normal
$\phi(\cdot)$	probability density function of standard normal
$\Delta t$	time step/sampling interval
$T$	gait cycle period or total time duration
$N$	number of samples or data points
$w$	weight or fusion parameter
$\lambda$	regularization parameter
$\alpha, \beta$	gain or weighting parameters
$\xi$	exploration parameter in acquisition functions

## SUMMARY

This dissertation presents a practical method for personalizing hip exoskeleton assistance using surface EMG-based human-in-the-loop optimization, cutting tuning time from hours to minutes while preserving assistance quality. We show that processed EMG provides a reliable objective for rapid personalization, enabling convergence within typical clinical sessions.

The research progresses from simulation studies revealing fundamental controller-hardware gaps to experimental validation across three activities. In leg swinging ( $n=8$ ), EMG-based optimization reduces muscle activity by 15-17% with <15 seconds of steady data per trial. In squatting ( $n=4$ ), the method completes tuning in 4 minutes 40 seconds and yields 21% lower metabolic cost with 17% lower EMG. In walking ( $n=11$ ), a multi-objective formulation balancing EMG and user preference identifies personalized controllers in 11-12 minutes, reducing metabolic cost by 14.9% while improving perceived exertion by 25-45%.

Three technical innovations enable this speed: (i) a signal-enhancement pipeline combining Hankel decomposition, Bayesian regularization, and optimized smoothing that improves composite EMG quality metrics by 108%; (ii) machine-learning-guided initialization from anthropometric measurements that reduces convergence time by 26.5% and improves final performance by 9.98%; and (iii) heteroscedastic Gaussian process surrogates with Expected Hypervolume Improvement that capture input-dependent noise, improving predictive accuracy by 23-31

Supporting investigations establish practical design principles. Systematic evaluation across 12 participants performing 30 conditions each reveals that simple amplitude summation provides

## SUMMARY (Continued)

the most reliable EMG-metabolic correlation ( $r=0.762$ ), challenging assumptions about complex feature necessity. Simulation studies comparing 12 controller architectures demonstrate that phase-adaptive impedance achieves 55.5% mechanical power reduction with minimal parameters, while Bezier profiles reach 62.9% reduction at higher implementation cost.

These results establish EMG-based HIL as a clinically feasible approach to exoskeleton personalization, validated across 23 healthy adults. The framework employs compact controller parameterizations (4-8 parameters) suitable for real-time optimization, with transparent cost functions and traceable convergence. Limitations include healthy-adult validation, electrode placement sensitivity, and restricted activity scope. Extensions should address clinical populations, online adaptation to fatigue, and broader task coverage.

# CHAPTER 1

## INTRODUCTION

Lower-limb exoskeletons promise to transform rehabilitation medicine and human augmentation, yet their clinical impact remains limited by a fundamental challenge: the need for rapid, patient-specific control optimization. This dissertation addresses this barrier by developing and validating an electromyography-based framework that reduces personalization time from hours to minutes, making exoskeleton therapy feasible within standard clinical appointments. Through systematic investigation across three distinct movement tasks with 23 healthy participants, this work establishes the methodological foundation for translating laboratory exoskeleton technology into practical clinical tools.

### 1.1 Context and Motivation

#### 1.1.1 The Growing Need for Mobility Assistance

Mobility defines human independence. The ability to move freely shapes social participation, employment opportunities, and quality of life. When mobility becomes impaired through neurological injury, age-related decline, or occupational hazards, the consequences cascade through every aspect of daily living. This growing challenge affects millions globally and demands technological solutions that can restore function, augment performance, and prevent injury.

Stroke exemplifies the devastating impact of mobility loss. The Global Burden of Disease Study documented 12.2 million new stroke cases in 2019, with over 101 million people living

with its effects [1]. Among first-time stroke survivors, 44.1% present with lower-extremity motor impairment upon hospital admission, while 46.0% cannot walk even with assistance [2]. These numbers translate into profound life changes: patients who can walk at admission are 9.48 times more likely to return home rather than institutional care. Each incremental improvement in walking ability doubles the odds of home discharge [2].

The trajectory following stroke reveals persistent challenges. One prospective cohort study found 21% of patients experienced clinically meaningful mobility deterioration between one and three years post-stroke [3]. This decline precipitates loss of independence in activities of daily living, increased caregiver burden, and social isolation. Daily reality involves navigating hemiparesis, spasticity, compromised balance, debilitating fatigue, and chronic pain. Critically, cognitive impairment compounds these physical challenges. Post-stroke cognitive deficits interfere with functional mobility and balance control independent of residual motor strength [4]. Locomotion requires substantial cognitive resources for motor planning, sensory integration, and environmental navigation. When executive control or attention becomes compromised, the capacity to manage walking complexity diminishes, even when musculoskeletal function remains partially intact.

Aging populations face similar mobility threats through gradual physiological decline. After age 50, adults lose 1.4% to 2.2% of muscle strength annually [5]. This erosion affects 35% of individuals aged 70 and the majority over 85 [6]. The consequences extend beyond individual suffering: mobility limitations in older adults generate an additional \$2,773 in annual healthcare expenditures per person [7]. Among households headed by someone aged 80 or older, 71% include

a member with activity limitations, while 45% report direct mobility disability such as difficulty walking or climbing stairs [7].

Occupational environments create a third major source of mobility compromise. Musculoskeletal disorders represent the leading cause of disability globally [8]. Workers routinely encounter biomechanical loads exceeding safe limits. Lumbar spine forces during standard warehouse tasks surpass the National Institute for Occupational Safety and Health's 3,400N action limit, accumulating tissue damage that risks permanent disability [9]. The U.S. Bureau of Labor Statistics reports that back injuries account for 38.5% of work-related musculoskeletal disorders requiring time away from work, with a median recovery period of 12 days compared to 8 days for other nonfatal injuries [10].

### **1.1.2 The Promise and Limitations of Exoskeleton Technology**

Lower-limb exoskeletons have emerged as a compelling response to these mobility challenges. These wearable robotic devices apply precisely timed mechanical power to human joints, potentially restoring function for those with impairments while augmenting strength and preventing injury in healthy individuals. Two decades of laboratory research have demonstrated that properly controlled exoskeletons can achieve remarkable physiological benefits.

The evidence spans multiple domains of human performance. During walking, even single-joint assistance produces substantial improvements. Ankle exoskeletons have achieved metabolic cost reductions ranging from 7.2% to 14.6% compared to unassisted walking [11]. When assistance parameters are individually optimized, the benefits amplify dramatically. Zhang et al. achieved a  $24.2 \pm 7.4\%$  metabolic reduction through personalized ankle assistance [12]. Hip

exoskeletons demonstrate comparable potential, with Ding et al. reporting 17.4% metabolic savings through optimized hip assistance [13].

The benefits extend beyond energy efficiency to direct muscular relief. Surface electromyography measurements reveal that exoskeleton assistance reduces muscle activation by 30% to 40% in targeted muscle groups [14]. During lifting tasks, knee exoskeletons decrease quadriceps activation by up to 31% [15], while back-support devices reduce erector spinae and gluteus maximus activity significantly [16]. Multi-joint systems achieve even more impressive results, with hip-knee-ankle exoskeletons reducing metabolic cost by 41% to 48% during loaded walking [17].

Despite these laboratory successes, clinical and commercial adoption remains minimal. Market projections anticipate growth, yet widespread deployment outside research settings has not materialized [18]. The barrier is not mechanical power or hardware sophistication but control personalization. The remarkable benefits documented in research studies emerge only when control parameters are carefully tuned to individual users. Generic or poorly tuned assistance can be ineffective or even detrimental.

### **1.1.3 The Personalization Imperative**

The assumption that universal assistance strategies can benefit all users has been repeatedly invalidated. Human biomechanics, physiology, and motor learning strategies vary profoundly between individuals. Dembia et al. observed that optimal assistance timing varies from 49% to 61% of the stride cycle across users, a 12% absolute variation representing a significant portion of the propulsive phase [19]. The consequences of ignoring this variability are severe. Zhang et

al. demonstrated that applying one person's optimized parameters to another reduces metabolic benefits by approximately 60% [12].

This variability stems from multiple sources operating across physiological, biomechanical, and neurological domains. Muscle fiber composition varies dramatically, with Type I fiber proportions ranging from 15% to 95% across individuals, directly affecting contractile properties and metabolic efficiency [20]. Anthropometric differences in segment lengths, mass distribution, and joint axes create unique movement dynamics for each person. These physical variations manifest in distinct neuromuscular control strategies, characterized by individual-specific muscle synergies and activation patterns [21].

Motor learning and adaptation introduce temporal complexity to the personalization challenge. Humans actively adapt their movement patterns when using exoskeletons, requiring up to 109 minutes of assisted walking to fully realize metabolic benefits [22]. This adaptation accounts for approximately half the total energy cost reduction, separate from controller optimization itself. Learning rates vary significantly between individuals, with novice users often exhibiting inefficient strategies like muscle co-contraction to "fight" the device before gradually learning to exploit its assistance.

This dynamic human response creates a fundamental paradox for optimization. The human-robot system being optimized continuously changes as users learn and adapt. Lengthy optimization protocols do not simply search a static landscape but actively reshape it through motor training. The "optimal" parameters identified after hours of testing reflect the specific sequence of conditions tested and may not represent generalizable settings for that user. This tension

between adaptation and optimization demands rapid personalization methods that minimize confounding from long-term motor learning.

#### **1.1.4 Critical Limitations of Current Approaches**

Existing personalization paradigms fail to meet clinical requirements for speed, reliability, and interpretability. Metabolic cost-based human-in-the-loop optimization, while physiologically grounded, requires 3 to 6 minute steady-state measurements per condition to account for oxygen uptake dynamics [23]. Testing even 30 parameter combinations demands hours of continuous activity, exceeding both clinical session durations and patient endurance limits. A typical optimization session identifying just two parameters consumes over an hour [12].

This time requirement introduces methodological confounds beyond practical constraints. Users continuously adapt and fatigue throughout multi-hour protocols, meaning algorithms chase moving targets. The approach requires expensive, cumbersome equipment unsuitable for clinical deployment. Furthermore, metabolic cost may not universally represent the optimal objective. Studies with amputees using powered prostheses found metabolic optimization failed to outperform hand-tuned settings, suggesting alternative objectives like stability or comfort may dominate for certain populations [24].

Simulation-based approaches promise rapid parameter exploration but suffer persistent translation gaps. Assistance strategies appearing beneficial in musculoskeletal models often provide diminished or absent benefits when implemented on hardware [19]. This simulation-to-reality gap arises from modeling limitations: soft tissue compliance at the human-device interface absorbs 20% to 40% of delivered power, users adopt complex adaptation strategies over minutes

to hours, and psychological factors like trust fundamentally alter movement strategies in ways simulations cannot predict.

Machine learning control, particularly deep reinforcement learning, faces sample complexity and interpretability barriers. These algorithms require thousands of trial-and-error interactions to converge, fundamentally incompatible with human subjects who cannot perform thousands of walking trials [25]. Even if sample requirements could be met, the resulting neural network policies operate as black boxes, preventing clinical verification and regulatory approval. The exploratory learning process poses unacceptable safety risks for clinical applications.

#### **1.1.5 Surface Electromyography: A Path to Rapid Personalization**

The limitations of existing paradigms necessitate a fundamentally different approach. An ideal personalization method would provide physiologically meaningful feedback rapidly enough to explore parameter spaces within clinical timeframes. Surface electromyography emerges as a uniquely suitable signal, offering millisecond-resolution access to neuromuscular control.

Muscle activation responds to mechanical changes within 50 to 200 milliseconds, contrasting sharply with the multi-minute timescale for metabolic steady-state [26]. This temporal advantage, spanning several orders of magnitude, enables parameter evaluation in seconds rather than minutes. An optimization algorithm can test dozens of conditions within a single clinical session, making comprehensive personalization feasible.

The physiological validity of EMG as an effort proxy is well-established. The size principle of motor unit recruitment links EMG amplitude directly to force production and metabolic demand. During cyclic activities, integrated EMG correlates strongly ( $r = 0.91$ ) with metabolic

power [27]. As users become more efficient through learning, both metabolic cost and EMG amplitude decrease in parallel, confirming their coupled relationship.

EMG represents a more direct measure of effort than metabolic cost. The physiological cascade begins with neural commands generating muscle activation (captured by EMG), leading to force production, mechanical work, and ultimately metabolic energy consumption measured through respiration. Metabolic cost provides a delayed, filtered echo of neuromuscular processes, while EMG offers immediate readout of motor commands. This directness enables real-time optimization of the control strategies users employ.

Combining rapid EMG feedback with sample-efficient Bayesian optimization creates a powerful personalization framework. Gaussian process models build probabilistic representations of the objective landscape, intelligently balancing exploration and exploitation to converge with minimal evaluations [28]. Recent demonstrations achieved EMG-based convergence in one-seventh the time of metabolic approaches while maintaining comparable assistance quality [29]. The transparency of Gaussian process posteriors supports clinical interpretation, unlike black-box alternatives.

This approach naturally extends to multi-objective formulations preserving the complexity of human-robot interaction. Rather than collapsing EMG and user preference into weighted sums, Pareto-optimal solutions explicitly represent trade-offs between physiological and experiential criteria. Clinicians and users can select from characterized solution sets based on treatment priorities, acknowledging that effective assistance must satisfy both objective and subjective requirements.

## 1.2 Research Questions and Objectives

### 1.2.1 Research Questions

This dissertation investigates whether EMG-based human-in-the-loop optimization can provide practical personalization of hip exoskeleton assistance. Three specific questions structure this investigation:

First, can surface EMG serve as a reliable objective function for HIL optimization despite noise susceptibility and placement sensitivity? This examines whether EMG-derived cost functions identify assistance parameters that reduce overall effort when optimizing based on signals from four surface electrodes.

Second, how does EMG-based optimization compare to established methods in convergence speed and assistance quality? This evaluates both time to beneficial parameters and resulting assistance quality measured through muscle activity, metabolic cost, and user preference.

Third, does the optimization framework generalize across different hip-centric activities? Leg swinging, squatting, and walking present distinct biomechanical demands. The investigation determines whether consistent signal processing and optimization strategies apply across these movement contexts.

### 1.2.2 Thesis Statement

This dissertation establishes that EMG-based human-in-the-loop optimization transforms hip exoskeleton personalization from an hours-long process to a clinically feasible procedure completed in minutes. The approach achieves personalized parameters within standard appoint-

ment windows while maintaining interpretability through traceable optimization processes and physiologically meaningful cost functions. Validation across three activities with 29 healthy participants demonstrates that EMG-based methods achieve meaningful assistance improvements, providing the methodological foundation for clinical translation.

### 1.2.3 Specific Aims

Aim 1 establishes foundational methodology through EMG-based HIL optimization for isolated hip movement using leg swinging. This simplified case eliminates balance and ground contact confounds while developing signal processing techniques, cost function formulations, and convergence characteristics.

Aim 2 extends the framework to load-bearing squatting. Higher forces and distinct eccentric-concentric phases test whether rapid optimization accommodates complex muscle activation patterns during functional movements.

Aim 3 validates the framework during walking, introducing continuous movement, dynamic balance, and multi-joint coordination. Bilateral assistance coordination and inclusion of user preference test whether the framework balances physiological and subjective goals.

## 1.3 Significance and Contributions

This research transforms exoskeleton personalization from a multi-hour metabolic optimization to a procedure completed within standard clinical appointments. The primary contribution is demonstrating that surface EMG, when processed through optimization-aware pipelines and embedded in Bayesian frameworks, enables personalization in 12 minutes or less while achieving assistance quality comparable to hours-long metabolic approaches.

Technical innovations include a signal enhancement pipeline combining Hankel decomposition with Bayesian regularization that improves EMG quality metrics by 108% while preserving physiological features. Machine learning models predict promising parameter regions from anthropometric measurements, reducing convergence time by 26.5% and improving final performance by 9.98%. Heteroscedastic Gaussian process models capture input-dependent human variability, improving surrogate accuracy by 23 to 31% compared to standard approaches.

Experimental validation establishes practical feasibility. During leg swinging with eight participants, EMG-based optimization reduced muscle activity by 15 to 17% with convergence in under 15 seconds per trial. Squatting experiments with four participants achieved 21% metabolic cost reduction with tuning completed in 4 minutes 40 seconds. Walking experiments with eleven participants demonstrated multi-objective optimization balancing EMG and user preference, converging in approximately 12 minutes while reducing metabolic cost by 14.9% and improving perceived exertion ratings.

Systematic evaluation of EMG-based cost functions across 360 trial conditions revealed that simple amplitude summation provides the most reliable correlation with metabolic power ( $r = 0.762$ ), challenging assumptions about complex feature necessity. Simulation studies comparing twelve controller architectures showed phase-adaptive impedance achieves 55.5% mechanical power reduction with minimal parameters, informing practical implementation choices.

Limitations include validation only in healthy adults, sensitivity to electrode placement, and evaluation on three activities. These define directions for clinical translation rather than funda-

mental barriers. The framework provides systematic methodology for EMG-based optimization extensible to clinical populations and additional tasks.

#### **1.4 Dissertation Organization**

This dissertation progresses systematically from foundational methods through functional validation to integrated multi-objective optimization. Chapter 2 reviews exoskeleton personalization literature, establishing the technical context and identifying gaps that motivate EMG-based approaches.

Chapter 3 compares simulation-derived controllers with hardware implementation during leg swinging, revealing performance gaps between predicted and actual assistance. These disparities motivate the human-in-the-loop refinement that follows.

Chapter 4 presents the core EMG-based HIL optimization framework using stationary leg swinging as a controlled testbed. This chapter achieves 15 to 17% muscle activity reduction with convergence in under 15 seconds per trial, establishing feasibility of the approach.

Chapter 5 enhances optimization initialization through machine learning models trained on anthropometric measurements. This addition improves final controller performance by 10% and reduces convergence time by 26%, demonstrating that prior user information can accelerate personalization.

Chapter 6 validates the framework during load-bearing squatting, achieving 21% metabolic cost reduction with optimization completed in 4 minutes 40 seconds. This chapter extends the approach to higher-force activities with distinct eccentric and concentric phases.

Chapter 7 develops automated EMG signal enhancement through multi-objective optimization of Hankel-based reconstruction and Bayesian smoothing. This preprocessing improves composite signal quality metrics by 108% while preserving physiological features necessary for control.

Chapter 8 analyzes twelve impedance control architectures through systematic simulation, comparing phase-adaptive, energy-modulated, and variable stiffness approaches. Results show phase-adaptive controllers achieve 55.5% mechanical power reduction with minimal parameterization.

Chapter 9 evaluates sixteen EMG-based cost functions across 360 trial conditions to identify reliable metabolic proxies. Simple amplitude summation achieves the highest correlation with metabolic power ( $r = 0.762$ ), validating its use throughout the thesis.

Chapter 10 implements multi-objective optimization for walking that simultaneously considers EMG cost and user preference. Using heteroscedastic Gaussian processes and Expected Hypervolume Improvement, the framework achieves 12-minute personalization that reduces metabolic cost by 14.9% while improving perceived exertion.

Chapter 11 synthesizes findings across all studies, discussing both demonstrated capabilities and encountered limitations. The analysis identifies when EMG-based optimization provides practical value and outlines specific extensions needed for clinical translation, including validation in patient populations and adaptation to additional activities.

Through this progression from isolated movements to complex locomotion, the dissertation establishes EMG-based human-in-the-loop optimization as a practical solution for rapid exoskeleton personalization.

## CHAPTER 2

### BACKGROUND AND LITERATURE REVIEW

#### 2.1 The Grand Challenge: Why Exoskeletons Need Personalization

The goal of powered exoskeletons is to augment strength, enhance endurance, and restore mobility. Turning this goal into clinical benefit has been harder than first assumed. The central difficulty is not power or mechanical reliability, but aligning assistance with person-specific movement.

##### 2.1.1 The Fallacy of Universal Assistance

Early exoskeleton development often replicated joint torque profiles of healthy walking and applied them broadly. This assumed that well-designed assistance patterns derived from population averages would help most users [30]. The expectation was that if the device supplemented typical muscular work, metabolic cost would drop.

This assumption did not hold. Even with substantial mechanical power (often 20 to 30 W at a joint), several early systems increased metabolic cost by 7 to 15% versus unassisted walking [30]. These outcomes highlight that population averages are poor predictors of individual optima. The coordination of muscle activation, joint mechanics, and sensory feedback varies across people; what helps one user may hinder another.

Zhang et al. used human-in-the-loop optimization to quantify this variability [12]. Peak torque magnitudes varied roughly fourfold across participants (0.2 to 0.8 Nm/kg), and timing

shifted by up to 15% of the gait cycle. Applying one participant's optimized profile to others cut benefits by about 60%, with some users losing benefits entirely. This provides strong evidence that personalization is required for effective assistance.

### **2.1.2 Neuromuscular Individuality: The Biological Basis of Variability**

Differences in how individuals organize and execute movement motivate personalization. At the control level, the nervous system coordinates muscles through functional groups (muscle synergies). These compositions differ among people. Rosati et al. identified four to five distinct activation patterns for single muscles across participants performing the same walking tasks [31].

Scano et al. reported that inter-subject variability in synergy structure exceeded intra-subject variability by a factor of 3.2 [32]. Some individuals emphasize proximal (hip-dominant) strategies, while others are ankle-dominant. An exoskeleton providing ankle assistance to a hip-dominant user can disrupt natural coordination and raise metabolic effort.

Basic spatiotemporal parameters also vary. Self-selected walking speed, where coordination is typically most stable, differs across adults. Controllers that enforce standardized kinematics or timing tuned for other speeds can move users away from their natural efficiency point, elevating variability and metabolic cost.

### **2.1.3 The Physical Human-Robot Interface: Where Mechanics Meet Biology**

The human–robot interface adds another layer of personalization. The connection via cuffs, straps, and frames has soft tissue compliance, friction, and potential kinematic misalignment that change force transmission.

Näf et al. showed that a 2 cm offset between biological and exoskeleton knee axes increased metabolic cost by 8 to 15% [33]. Misalignment deforms soft tissues and prompts muscle activation against the device, generating parasitic forces.

Interface pressure also matters. Massardi et al. reported that 73.8% of soft-tissue injuries were associated with pressure concentrations exceeding 35 kPa at attachment points [34]. Securing the device while distributing pressure requires user-specific adjustment.

Interface mechanics act as a dynamic filter. Ding et al. found that attachment compliance introduces transmission delays that require earlier torque initiation, shifting optimal timing by 8 to 12% of the gait cycle as stiffness changes [13]. Thus, an assistance profile is only optimal for specific interface properties; strap adjustments or tissue differences imply control adjustments.

#### **2.1.4 Clinical Populations: When Pathology Amplifies Variability**

Personalization is even more important in clinical populations. For stroke survivors with asymmetric gait, Awad et al. showed that symmetric assistance could worsen asymmetry, whereas unilateral assistance targeting paretic deficits improved symmetry indices by 20 to 30% [35]. The specific profile depended on deficit patterns (e.g., distal vs. proximal weakness).

In incomplete spinal cord injury, Del-Ama et al. observed large differences in optimal assistance across residual control patterns [36]. Participants with preserved hip flexion but absent ankle control benefited from full ankle assistance with minimal hip support; diffuse weakness required coordinated multi-joint assistance. Timing relationships between joints were critical for forward progression.

With age-related decline, Lakmazaheri et al. reported assistance profiles that differ from younger users [37]. To prioritize stability, peak torque occurred 8 to 10% earlier in the gait cycle with magnitudes 25 to 30% lower. Reduced proprioceptive acuity meant parameters stabilized after 25 to 30 minutes of adaptation rather than 10 to 15 minutes.

### **2.1.5 The Assistance Landscape: Conceptualizing Personalization**

These neural, biomechanical, and pathological sources of variability define an individual assistance landscape. The multidimensional parameter space includes torque magnitude, timing, rate, and stiffness; performance (often metabolic cost) is the elevation. Traditional approaches placed everyone at a single population-average coordinate. Evidence shows that this point is often far from the individual's optimum. Practical exoskeleton control therefore requires methods that efficiently search each user's landscape to locate a personal optimum.

## **2.2 The Evolution of Personalization Approaches**

Recognition of the need for personalization led to attempts to predict optimal strategies from models, followed by task simplification, and finally data-driven discovery. Each step clarified limits and informed the shift toward empirical methods.

### **2.2.1 The Promise and Peril of Predictive Simulation**

Predictive musculoskeletal simulation synthesizes locomotion by solving optimal control problems on detailed models and cost functions, typically metabolic energy [38]. The appeal was rapid virtual evaluation of many assistance strategies. Dorn et al. generated gaits that matched experimental data well: 92% of joint angle trajectories and 78% of joint torque trajectories within one standard deviation of human measurements [38].

However, controllers optimized in simulation often underperformed on hardware [39]. Sources of mismatch include regressed segment parameters, simplified joint representations [40], and missing interface dynamics. Franks et al. used instrumented phantom limbs and showed that increasing exoskeleton spring stiffness increased power dissipated at the soft-tissue interface and reduced net power delivered to the joint [41]. The interface behaves like a biomechanical low-pass filter with phase lags and attenuation absent from rigid-connection assumptions.

Human adaptation is also central. Users alter muscle activation within 20 to 30 minutes, reducing metabolic cost even with constant assistance [42]. The plant is non-stationary; a controller optimal for a novice can become suboptimal after adaptation. Time-invariant models do not represent these dynamics, explaining the persistent gap.

### 2.2.2 Strategic Simplification: Isolating Core Dynamics

Researchers simplified tasks and models to isolate key dynamics. Stationary leg swinging preserves hip flexion–extension mechanics while removing foot–ground contact, balance, and multi-joint complexity [43]. Reduced antagonistic Hill-type models capture force–length and force–velocity behavior with contractile, series-elastic, and parallel-elastic elements [44, 45].

Under these constraints, alignment improved. Aguirre-Ollinger et al. designed inertia compensation that restored natural limb dynamics with a one-degree-of-freedom hip exoskeleton; simulation matched experiments [43]. This indicates that model fidelity must match task complexity. Still, the path from constrained tasks to full walking remained long, motivating pragmatic hardware-centric methods.

### 2.2.3 The Failure of Expert Intuition

Manual parameter tuning based on observation and feedback proved slow and inconsistent [46]. Performance is highly sensitive to parameters: timing errors of 2 to 3% of the gait cycle (20 to 30 ms) can change assistance into hindrance [47]. Zhang et al. showed that well-chosen parameters reduced metabolic cost by 24% versus zero-torque walking, while poorly chosen parameters increased cost above baseline [12]. The search landscape has narrow peaks and nearby valleys, making intuition unreliable.

### 2.2.4 The Shift to Data: Embracing Empirical Optimization

Human-in-the-loop (HIL) optimization treats the coupled system empirically [48]. The algorithm selects parameters, the user performs the task, performance is measured, and the selection updates [49]. This reduces reliance on detailed modeling of biomechanics or soft tissue; interface compliance and user adaptation are reflected in the measurements.

HIL has produced large gains using the same hardware as generic controllers. Demonstrations include walking [17], running [47], load carriage [50], and objectives beyond energy such as walking speed [51] and user preference [52]. Compliant control is necessary so that testing suboptimal parameters remains safe and comfortable.

### 2.2.5 From Prediction to Partnership

The move from prediction and manual tuning to HIL optimization reframes human–robot interaction. Rather than prescribing trajectories or forces, modern exoskeletons provide a framework for user–device coordination. Impedance control enables this space for negotiation, allow-

ing natural variation while supplying graded support. The success of HIL supports this partnership view: useful assistance is discovered through systematic interaction rather than fixed in advance.

### 2.3 Control Architectures for Human–Robot Coordination

Exoskeletons must deliver meaningful mechanical power while maintaining safe, compliant interaction with a variable user. Unlike industrial robots in structured settings, exoskeletons operate with an active human in the loop [53]. This has shifted control from rigid command structures toward adaptive frameworks that coordinate with human intent.

#### 2.3.1 The Limitations of Classical Control Approaches

Early strategies adapted high-gain position tracking of predefined trajectories. In systems like LOPES, deviations were treated as errors to correct [54]. When users adjusted gait for speed or obstacles, controllers generated corrective torques that worked against voluntary movement [55].

Even small timing misalignments (a few percent of the gait cycle) can turn assistance into resistance and raise metabolic cost [12]. High stiffness for trajectory fidelity also risks force spikes during contact transitions [56]. In practice, the assumption that deviations equal error is often incompatible with variable human movement.

Pure force control prioritizes compliant interaction by regulating forces rather than trajectories, granting users kinematic authority. However, in unconstrained phases such as swing, lack of a kinematic reference can cause drift or oscillation, limiting use to constrained tasks [57].

Hybrid position–force schemes partition task spaces and often rely on finite state machines (FSMs) to switch control laws across gait events [58]. FSM transitions can create discontinuities perceived as jerks [53]. Discrete states also struggle to represent continuous, rhythmic locomotion.

### 2.3.2 Impedance Control as a Unifying Framework

Impedance control regulates the dynamic relation between force and motion by implementing a virtual mass–spring–damper [59]. A common form is

$$\mathbf{F} = \mathbf{M}(\ddot{\mathbf{x}} - \ddot{\mathbf{x}}_d) + \mathbf{B}(\dot{\mathbf{x}} - \dot{\mathbf{x}}_d) + \mathbf{K}(\mathbf{x} - \mathbf{x}_d), \quad (2.1)$$

with virtual inertia  $\mathbf{M}$ , damping  $\mathbf{B}$ , and stiffness  $\mathbf{K}$ . In free space, if position error is near zero, forces are near zero; with contact, forces build smoothly with penetration, avoiding hybrid discontinuities. One continuous law covers both regimes without explicit mode switching.

This aligns with human motor control. The nervous system modulates joint impedance via co-contraction, raising stiffness for precision or stability and lowering it for compliant interaction [60]. During locomotion, ankle quasi-stiffness varies markedly across the gait cycle, from minimal values in early swing to high values in stance [61, 62].

Impedance parameters map to perceptible properties: stiffness (resistance to displacement), damping (dissipation and settling), and virtual inertia (apparent weight). Users can form internal models of device behavior, aiding adaptation and trust [63]. Passivity analysis shows that properly designed impedance controllers remain stable across passive environments [64].

Energy-tank methods bound energy injection during parameter changes for safe operation with time-varying impedance [65].

### **2.3.3 Variable Impedance and the Personalization Challenge**

Fixed impedance improves on rigid tracking, but evidence shows that optimal impedance changes with task phase and user needs [66]. Variable impedance modulates stiffness and damping in real time. For walking, high impedance can support shock absorption and stability in early stance, then drop during swing for efficient advancement [61]. For sit-to-stand, impedance can be scheduled to assist at deep knee angles and relax near standing [67].

Variable impedance expands the parameter space. Designers must specify trajectories of stiffness and damping across the cycle. Phase-based scheduling provides smooth modulation [68]. Basis functions (e.g., sinusoids or Bézier curves) reduce dimensionality while preserving expressiveness. Despite this, many parameters remain.

Manual tuning is impractical at this scale, and inter-subject variability is substantial: optimal stiffness and damping can differ by 50% or more across users for the same task [69]. Some benefit from high impedance throughout, others from minimal, precisely timed support [67]. These findings motivate automated methods to explore the high-dimensional space and identify user-specific settings. HIL optimization has become common for this purpose [12], though convergence time remains a barrier to clinical deployment.

## 2.4 Temporal Constraints in HIL Optimization

### 2.4.1 The Metabolic Cost Bottleneck

Traditional indirect calorimetry requires 4 to 6 minutes per condition to reach reliable steady state [70, 71]. Oxygen uptake follows exponential dynamics; clinical populations can be slower (e.g., children with cerebral palsy with median time constants of 33.1 s versus 10.2 to 31.6 s in typically developing children) [70]. About three time constants are needed to approach 95% of steady state.

After steady state, an additional 2 to 3 minutes of data reduces breath-to-breath variability from above 10% to below 8% [72, 73]. Exploring 20 to 50 parameter combinations therefore implies 80 to 300 minutes of steady-state data alone [12, 13], far beyond typical clinical sessions.

Short protocols bias results. Thirty-second walking bouts overestimate oxygen consumption by 20 to 60% due to transient dynamics [71]. A case series found HIL failures when measurement variability exceeded expected device benefits (about 5 to 10%) [74]. Advanced approaches can shorten but not eliminate the window: Bayesian modeling can estimate steady state from about 2.5 minutes with 1 to 3% error in healthy adults [70]; machine learning achieves real-time prediction with higher error (about 23 to 26%) [75]; and independent-breath methods reduce variability [76, 77]. Small differences between parameters (often 5 to 10%) still require longer measurement.

#### 2.4.2 EMG as a Rapid Alternative

Electromyography (EMG) offers millisecond-resolution access to neural drive. Henneman's size principle implies an ordered recruitment from smaller oxidative to larger glycolytic units as force rises, supporting a relation between EMG amplitude and metabolic demand [78]. Models often describe metabolic power as a baseline plus a weighted sum of squared EMG from relevant muscles [72].

Empirical work supports strong coupling in cyclic locomotion. Using squared integrated EMG from soleus and vastus lateralis explained 96% of metabolic variance during incline walking across 16 subjects [73]. With appropriate muscle weighting and delays (about 28 s), breath-by-breath correlations near 0.91 have been reported during cycling [72]. Reviews find correlation coefficients from 0.56 to 0.92 across tasks [79].

Limitations remain. Fatigue increases recruitment without proportional metabolic changes [80]. Co-contraction can elevate EMG with little positive work [81]. Muscle-specific correlations can be low (e.g., lateral gastrocnemius  $R^2 = 0.393$ , soleus  $R^2 = 0.208$ , tibialis anterior not significant during assisted walking) [82]. Subject-specific calibration is important, and between-subject generalization is limited [83].

#### 2.4.3 Achieving Rapid Convergence

EMG-based cost functions reduce evaluation windows from minutes to seconds. Real-time pipelines use band-pass filtering at 20–450 Hz, full-wave rectification, and low-pass envelopes at 2–10 Hz, with sub-20 ms latencies [84, 85]. Task-specific muscle sets are sufficient (e.g., soleus

and tibialis anterior for ankle; vasti and hamstrings for knee) [13]. Dynamic normalization to baseline walking removes the need for maximum voluntary contractions [86].

Time savings are substantial. An EMG-based HIL framework reduced per-iteration data from 120 s to 25 s while cutting rectus femoris activation by 33 to 42% [29]. Bayesian optimization with summed EMG intensity converged to optimal hip flexion assistance in about 21.4 minutes versus about 83 minutes with metabolic feedback [13]. For dynamic squatting, EMG-guided optimization finished in 4 min 40 s with 21.4% activation reduction and 21.3% metabolic savings [87].

Direct comparisons show close agreement: EMG-optimized parameters yielded 14.8% metabolic reductions versus 15.2% for metabolically optimized settings, in about one-seventh of the time [12]. Real-world walking with wearable sensors converged within 5% of metabolically optimal parameters at about one-quarter the duration [88]. Test-retest reliability is generally lower for EMG-based optimization due to electrode sensitivity and day-to-day variability [89].

## 2.5 Signal Reliability Challenges

### 2.5.1 Signal Quality Challenges

EMG signals face motion artifacts that dominate 0–20 Hz and overlap motor unit firing [90]. Transient bursts often appear at heel strike (50 to 500 ms), while lift-off artifacts can exceed 1 s. Artifact rates increase from 12.7 events/min for walking to 22.1 for stair descent, and are about 50% higher in clinical populations [90, 91].

Electrode-skin stability also matters. Impedance can drift by about 13.23% in the first 10 minutes, and an additional 9.02% by 15 minutes before stabilizing [92]. This initial period can

bias HIL evaluations. Spatial sensitivity is high: displacements of 5 to 10 mm from motor points reduce amplitude by 15 to 40% and alter spectra [93, 94]. Over 8 hours, signal-to-noise ratio can drop 20 to 40% due to gel dehydration and mechanical shifts [95].

Advanced filtering helps. Adaptive noise cancellation improved SNR by 14.3 dB versus 8.7 dB for Butterworth filters with about 18.5 ms latency [96]. Feed-forward comb filters achieved envelope correlations above 0.98 for powerline and 0.94 for motion artifacts with efficient implementations [97]. Canonical correlation analysis targets the overlapping 21–50 Hz band, producing 10 to 20% greater spectral reductions than PCA while preserving physiology [98, 99].

### 2.5.2 Sample-Efficient Search

Bayesian optimization (BO) enables intelligent exploration. In exoskeleton applications, BO can reach about 95% of optimal performance within 20 to 40 iterations [13], a reduction of roughly 65 to 70% versus grid search. For hip assistance, about 17.4% metabolic reduction was achieved in about 21.4 minutes with BO versus more than 80 minutes with traditional methods [12, 13].

Acquisition choice matters. Expected improvement performs well in low-noise conditions, while GP-UCB can be preferable under heteroscedastic noise typical of physiological signals [100]. Heteroscedastic Gaussian processes that account for input-dependent noise can improve convergence by about 15 to 20% in high-variance regions [100]. Inter-subject differences produce convergence variance (about 22 to 41 iterations; coefficient of variation about 18.7%) [49, 100], but computational demands remain tractable for under 100 evaluations.

### 2.5.3 Intelligent Initialization

Machine learning can reduce cold-start time. Linear discriminant analysis plus support vector machines achieved about 90.69% classification accuracy with three-session training and about 86.98% with a single session [101]. Predictive features include residual limb circumference (weight 0.32), muscle thickness (0.28), walking speed, and leg length for timing [101, 102].

ML-based starting points can cut BO convergence time by 30 to 50% (about 25 minutes saved per user) [103]. Useful performance appears with training sets of 20 to 30 users, with further gains beyond 100 [102]. Transfer learning adapts to new users with 10 to 20% of typical data, yielding mean absolute timing errors of 2 to 4% of the gait cycle [103]. Feature engineering links muscle mass and fat percentage to torque magnitudes (reported  $r^2$  up to 0.93) [104]. Autoencoders compress about 100 features to 15 with about 4.1% reconstruction error, enabling about 3.2 ms inference on consumer hardware [105].

## 2.6 Beyond Physiology: Incorporating User Preference

### 2.6.1 Limitations of Single-Objective Optimization

Physiological optimization alone may not capture acceptance and functional benefit. Controllers that reduce EMG by about 24.2% can still feel unnatural or demanding, with lower satisfaction despite better biomechanical metrics [106, 107]. Preference landscapes often have multiple local optima reflecting control strategies and comfort [108]. Older adults can prefer slightly suboptimal patterns that feel more stable [106]. Stroke survivors may reject strategies that minimize paretic effort if they feel unnatural or require high attention [109].

### 2.6.2 Multi-Objective Frameworks

Multi-objective BO maps Pareto fronts between physiological and experiential metrics rather than collapsing them into a weighted sum [110]. Heteroscedastic Gaussian processes model input-dependent noise, which is higher for subjective ratings than for physiological measures, improving convergence in high-variance regions [111, 112]. Expected hypervolume improvement explores the objective space efficiently without prior weights; reported applications found Pareto-optimal solutions in about 28.3 iterations versus about 62.7 for sequential weighted-sum approaches [110].

Safety constraints are critical. SafeOpt and constrained BO keep exploration within biomechanical limits, reducing unsafe evaluations [113, 114]. In spinal cord stimulation, safety-aware BO kept about 87.5% of trials within probabilistic bounds across eight muscle groups [115].

### 2.6.3 Integrated Multi-Objective Frameworks

Integrated frameworks show clinical viability across tasks. Variable-stiffness hip exoskeleton optimization converged within about 12 minutes for walking and squatting when optimizing metabolic cost and preference [88]. Reported outcomes include about 18.2% reductions in integrated muscle activity for walking and about 17.2% metabolic reductions for squatting, with satisfaction increases from 68.3 to 82.4 on the System Usability Scale [88, 107].

Task-specific Pareto fronts differ: walking favors consistent low-level support with 0.2 to 0.4 Nm/kg peaks, while squatting benefits from 0.6 to 0.8 Nm/kg concentrated within  $\pm 5\%$  around key events [88]. Real-world walking over about one hour showed a 9% increase in self-selected speed and a 17% reduction in energy expenditure with individualized trade-offs [88].

## 2.7 Current State and Future Directions

The convergence of advances in biomechanics, control theory, and human factors has established personalization as the cornerstone of effective exoskeleton deployment. The quantifiable "personalization premium" reaches 8–10 percentage points: generic controllers achieve 31Con-temporary exoskeleton control architectures implement variable impedance control at multiple timescales—low-level torque regulation at 100–1000 Hz and high-level adaptation at 1–10 Hz—to maintain stability while responding to user intent [116]. Recent implementations combine neural networks for motion intention estimation with adaptive laws learning user limb impedance, enabling trajectory-free assistance that amplifies user effort rather than imposing predetermined patterns [117]. This responsive control paradigm proves particularly important for users with atypical gaits or when navigating unstructured environments, establishing the technical foundation upon which personalization algorithms operate. The critical bottleneck limiting clinical translation has shifted from mechanical design to optimization efficiency. Human-in-the-loop optimization using metabolic feedback, while producing substantial benefits, requires hours of continuous walking—exceeding typical therapy sessions and patient endurance [12]. Electromyographic signals have emerged as the leading solution to this temporal constraint, providing millisecond-resolution neural drive measurements that correlate strongly with metabolic cost while enabling convergence in minutes rather than hours [13]. Bayesian optimization with Gaussian process surrogates has become the dominant search algorithm, efficiently navigating parameter spaces through acquisition functions that balance exploration of uncertainty with exploitation of promising regions [100]. Yet EMG-based optimization in-

troduces its own technical challenges that must be addressed for reliable clinical deployment. Motion artifacts contaminate the 0–20 Hz frequency band where they overlap with physiological signals, electrode-skin impedance varies by orders of magnitude across sessions, and crosstalk from adjacent muscles corrupts target recordings [118, 119]. The "observer effect" compounds these issues: as exoskeleton assistance reduces muscle activation, the very signals used for control change, potentially creating unstable feedback loops [120]. Advanced filtering techniques including adaptive noise cancellation and canonical correlation analysis partially mitigate these challenges but cannot eliminate them entirely [96, 98]. The recognition that physiological optimization alone inadequately captures user acceptance has motivated multi-objective frameworks that simultaneously consider metabolic cost, user preference, stability, and comfort [110]. These methods map Pareto frontiers rather than collapsing objectives into weighted sums, allowing users to select personally meaningful trade-offs between competing goals. Variable-stiffness exoskeletons optimized through multi-objective approaches achieve comparable metabolic reductions while substantially improving user satisfaction scores [88]. This evolution toward holistic optimization acknowledges that effective assistance must satisfy both measurable performance metrics and subjective experiential factors. Emerging paradigms offer complementary approaches with distinct trade-offs. Reinforcement learning eliminates explicit human modeling but requires extensive pre-training to ensure safe exploration [121, 122]. Computer vision enables non-contact personalization through markerless motion capture, though computational demands currently limit real-time implementation [123]. Hybrid approaches increasingly combine modalities: EMG-kinematic fusion achieves 96.43% gesture recognition accuracy compared

to 83–84% for single modalities [124, 125]. These diverse methodologies reflect the field’s recognition that no single sensing or optimization approach optimally addresses all personalization challenges. The synthesis of literature across control architectures, optimization algorithms, and physiological measurement reveals a clear research gap: while EMG-based optimization offers the temporal efficiency necessary for clinical deployment, signal reliability challenges and limited validation across diverse populations constrain practical implementation. Addressing this gap requires systematic investigation of robust signal processing methods, comprehensive evaluation of optimization convergence across heterogeneous users, and development of frameworks that gracefully handle the uncertainties inherent in physiological signals. The following chapters present methods and experiments designed to advance EMG-based personalization from laboratory demonstration toward clinical reality, focusing on signal reliability, optimization efficiency, and practical deployment considerations essential for translating these technologies into therapeutic practice.

## CHAPTER 3

### OPTIMAL SWING ASSISTANCE USING A HIP EXOSKELETON: COMPARING SIMULATIONS WITH HARDWARE IMPLEMENTATION

#### 3.1 Overview

This chapter addresses the practical problem of translating simulation-derived exoskeleton controllers to human-in-the-loop hardware. Rather than attempting to close the simulation-reality gap by increasing model complexity indefinitely, the approach taken here is complementary: simplify the experimental task so that it can be represented faithfully by tractable simulation models and evaluated directly on a physical hip exoskeleton. Stationary leg swinging isolates hip flexion–extension dynamics, reduces confounding balance and multijoint interactions, and therefore provides a controlled setting in which simulation predictions and hardware behavior can be compared meaningfully.

A two-stage simulation pipeline is used to produce candidate assistance profiles. A reduced pendulum model explores broad profile shapes through discrete optimization, and a Hill-type muscle model refines those shapes subject to physiological constraints. Discovered profiles are then parameterized for practical implementation (RMS, PKK and DISMM families, each with

---

Parts of this chapter are taken from a conference paper presented at ASME-IDETC 2023,  
<https://doi.org/10.1115/DETC2023-117126>

general-work and positive-work variants), which permits rapid mapping from simulated torque trajectories to the motor commands used on the device.

These parameterized profiles are implemented on a custom hip exoskeleton and evaluated with human subjects across a range of swing frequencies. Experimental conditions include an unassisted baseline (no device), a zero-assistance control (device worn but unpowered), and active assistance with each optimized profile. Muscle activity from principal hip flexors and extensors is recorded via EMG, and performance is assessed in terms of reduction in biological torque and EMG-derived effort, plus qualitative observations of subject adaptation and comfort.

Direct comparison between simulation and hardware reveals both correspondence and important divergence. Simulation provides useful initial templates and highlights the value of muscle-model-derived controllers, yet hardware experiments show frequency-dependent behavior and human adaptation effects that were not captured in feed-forward simulations. Notably, allowing controlled negative work improves cyclic assistance, and more physiologically informed profiles (DISMM) tend to transfer better to hardware than the simplest pendulum-derived shapes, though parameter sensitivity remains a practical concern.

The results presented here serve two functions within the thesis. They validate the experimental platform and preliminary parameterization strategy, and they identify the limitations of fixed, simulation-only optimization—limitations that motivate the EMG-based, human-in-the-loop optimization framework developed in later chapters. The controllers and empirical lessons from this chapter therefore act as informed starting points for user-specific tuning rather than as final, deployable solutions.

## 3.2 Methods

### 3.2.1 Simulation Framework

We employ a two-stage simulation approach progressing from simple to complex models:

#### 3.2.1.1 Stage 1: Pendulum Model for Profile Shape Discovery

The pendulum model captures fundamental swing dynamics:

$$\dot{x}_1 = x_2 \quad (3.1)$$

$$\dot{x}_2 = -\frac{g}{L} \sin(x_1) + \frac{u}{mL^2} \quad (3.2)$$

where  $x_1$  represents angle,  $x_2$  angular velocity,  $g = 9.8 \text{ m/s}^2$ ,  $L = 0.365 \text{ m}$  (average leg length),  $m$  = leg mass, and  $u$  = applied torque.

We optimize for 20 discrete torque values across a swing from  $-20^\circ$  to  $30^\circ$ , testing multiple objective functions to explore the solution space without preconceptions.

#### 3.2.1.2 Stage 2: Hill-Type Muscle Model for Parameter Refinement

The muscle model introduces physiological constraints through antagonistic muscle pairs (rectus femoris and biceps femoris). We optimize a weighted cost function:

$$\min_{\boldsymbol{\tau}_m} w \cdot \int \tau_b^2 dt + (1 - w) \cdot \frac{\boldsymbol{\tau}_m^T \boldsymbol{\tau}_m}{\Delta t} \quad (3.3)$$

where  $\boldsymbol{\tau}_m$  contains motor torques,  $\tau_b$  represents biological torque, and  $w$  balances biological effort against motor efficiency.

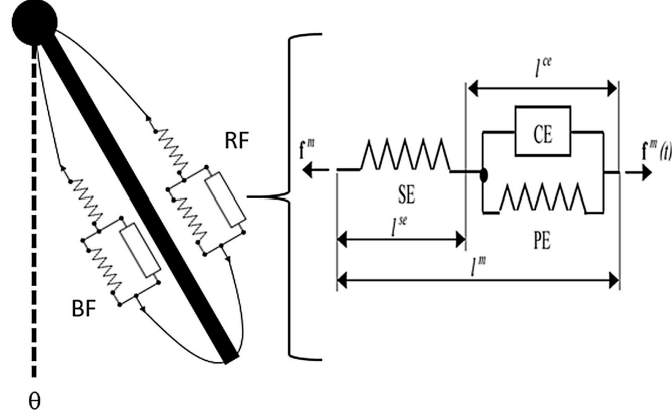


Figure 1. Antagonistic Hill-type muscle model for hip flexion/extension, with rectus femoris (positive torque) and biceps femoris (negative torque).

### 3.2.2 Profile Parameterization

To enable hardware implementation, we parameterize discovered profiles into three categories:

- **RMS Profile:** 4 parameters ( $P_1, P_2, P_3, L$ ) defining a peaked assistance curve
- **PKK Profile:** 3 parameters ( $V_1, V_2, S$ ) creating a step-like assistance pattern
- **DISMM Profile:** 6 parameters ( $D_1-D_4, C_1-C_2$ ) allowing more complex shapes

Each profile has variants allowing general work (GW) or positive-work-only (PW). Figure 2 summarizes the parameterized profile shapes (both general-work and positive-work-only variants) that were converted to motor commands for

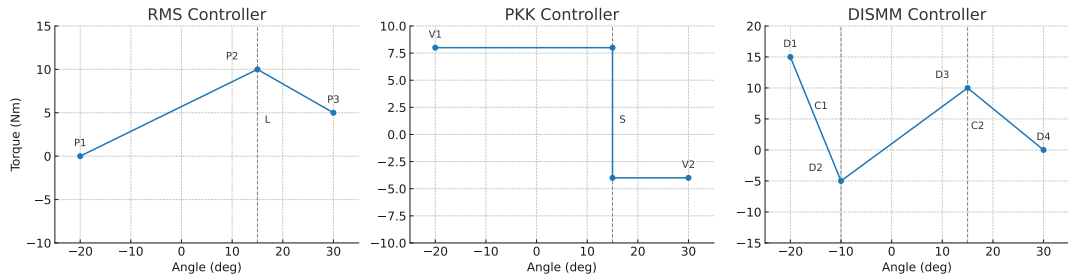


Figure 2. Torque–angle profiles for all three types of controllers (RMS, PKK, DISMM) across the swing. These serve as the basis for both simulation validation and hardware implementation.

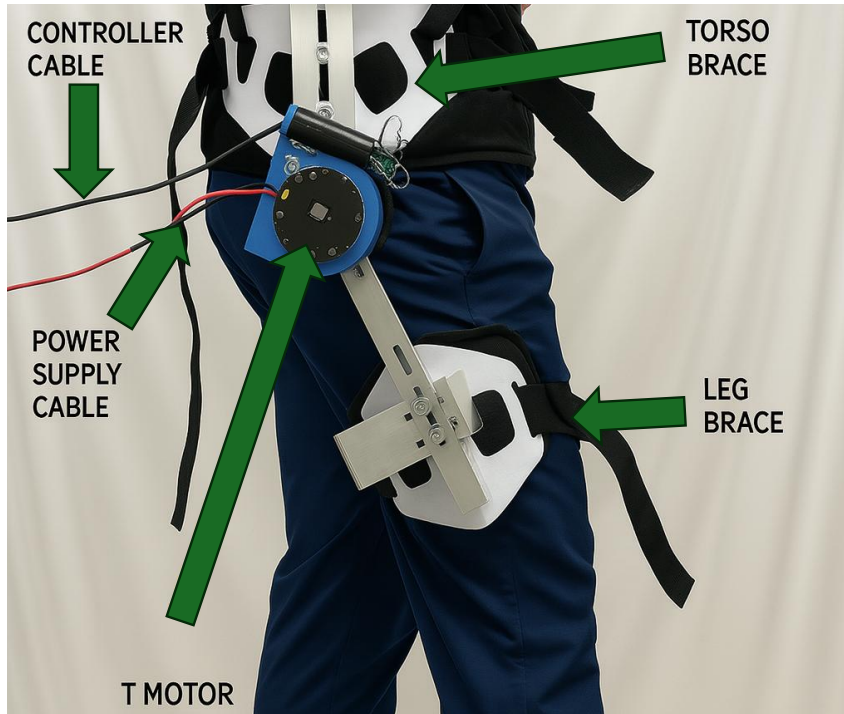


Figure 3. Custom hip exoskeleton used for hardware experiments, showing motor housing, straps, rotary encoder, and safety stops.

### 3.2.3 Hardware Implementation

#### 3.2.3.1 Experimental Platform

The hip exoskeleton (detailed in Figure 3) features:

- AK70-10 BLDC motor (25 Nm peak torque)
- Real-time angle tracking via rotary encoder
- CAN-based torque control at 100 Hz
- Safety features including emergency stops and software torque limits

#### 3.2.3.2 Experimental Protocol

Subjects performed leg swinging at four frequencies (80%, 90%, 110%, 120% of natural frequency) under three conditions:

1. No exoskeleton (NE) - baseline muscle activity
2. Zero assistance (ZA) - wearing unpowered device
3. Active assistance (AA) - implementing optimized profiles

EMG data from rectus femoris and biceps femoris quantified muscle effort reduction.

## 3.3 Results

### 3.3.1 Simulation Predictions

Table I shows predicted biological torque reductions across frequencies and profiles. All profiles achieved statistically significant reductions ( $p < 0.05$ ), with DISMM showing the highest average reduction of 24.85%.

TABLE I

PREDICTED PERCENT REDUCTION IN BIOLOGICAL TORQUE FROM SIMULATION

Profile	80% NF	90% NF	110% NF	120% NF
RMS	-37.03%	-31.45%	-15.86%	-20.72%
PKK	-28.03%	-20.66%	-4.21%	-9.07%
DISMM	-41.55%	-29.06%	-11.10%	-17.69%
RMS-PW	-37.62%	-27.36%	-15.85%	-20.75%
PKK-PW	-33.31%	-4.00%	-10.41%	-8.91%
DISMM-PW	-33.02%	-22.34%	-7.35%	-15.19%

### 3.3.2 Hardware Performance

Hardware results revealed both successes and unexpected behaviors:

#### 3.3.2.1 EMG Reduction Performance

Table II presents muscle activity reductions compared to no-device baseline. Notable findings include:

- Average reduction of 23.69% across all conditions
- Higher frequency swings (110%, 120% NF) showed better performance
- Some profiles (RMS at 90% NF) increased muscle activity

### 3.3.3 Key Comparative Insights

#### 3.3.3.1 Frequency-Dependent Performance Reversal

Simulation predicted better performance at lower frequencies (28.79% reduction at 80-90% NF vs. 13.09% at 110-120% NF). Hardware showed the opposite trend (16.35% vs. 31.04%),

TABLE II

## PERCENT CHANGE IN EMG ACTIVITY WITH ASSISTANCE VS. NO DEVICE

Profile	80% NF	90% NF	110% NF	120% NF
RMS	-27.87%	+8.14%	-17.59%	-33.81%
PKK	-16.38%	-28.69%	-33.35%	-26.49%
DISMM	-22.17%	-23.03%	-31.15%	-35.67%
RMS-PW	-26.34%	+14.51%	-28.95%	-33.95%
PKK-PW	-19.14%	-29.00%	-27.44%	-34.93%
DISMM-PW	-22.29%	-3.92%	-33.21%	-35.88%

suggesting fundamental differences in how humans adapt to assistance at different movement speeds.

### 3.3.3.2 Work Type Effects

General work controllers outperformed positive-work-only variants:

- Simulation: 22.20% (GW) vs. 19.68% (PW) reduction
- Hardware: 24.01% (GW) vs. 23.38% (PW) reduction

This validates the benefit of allowing controlled negative work for cyclic movements.

### 3.3.3.3 Model Complexity Impact

Controllers derived from the muscle model (DISMM) outperformed simpler pendulum-based designs (RMS, PKK) by approximately 3-4% in both simulation and hardware, justifying the added complexity.

### 3.4 Discussion

#### 3.4.1 Simulation-to-Hardware Gap Analysis

While average performance was comparable between simulation (20.94% reduction) and hardware (23.69% reduction), individual profile performance varied significantly. This variability stems from:

1. **Human adaptation:** Subjects actively adapted their muscle coordination patterns in response to assistance, a phenomenon not captured in feed-forward simulations.
2. **Frequency-dependent strategies:** The reversal in frequency-performance relationships suggests humans employ different motor strategies at different speeds, requiring frequency-specific optimization.
3. **Profile sensitivity:** Some profiles (particularly RMS variants) proved highly sensitive to parameter selection, performing well at certain frequencies but poorly at others.

#### 3.4.2 Design Principles for Hardware Implementation

Based on these findings, we extract key principles for exoskeleton controller design:

1. **Embrace controlled negative work:** Allowing small amounts of negative work improves overall assistance effectiveness for cyclic movements.
2. **Start with complex models:** While simpler models provide insight, muscle-model-derived controllers show more robust performance.

3. **Expect frequency-specific tuning needs:** Controllers optimized at one frequency may not generalize well, motivating adaptive approaches.
4. **Plan for human adaptation:** Static optimization cannot capture how users adapt to assistance over time.

### 3.4.3 Limitations and Future Directions

This study's limitations motivate the EMG-based optimization approach developed in subsequent chapters:

- Single-subject validation limits generalizability
- Open-loop control cannot adapt to user changes
- Simulation models cannot predict individual responses
- Manual parameter selection remains time-consuming

## 3.5 Conclusion

This chapter established that while simulation-based optimization provides valuable initial controller designs, significant gaps exist between predicted and actual performance. Key findings include:

1. Simulation-derived controllers can reduce muscle activity by approximately 24% but require hardware-specific tuning
2. Allowing controlled negative work improves assistance effectiveness

3. Frequency-dependent performance differs fundamentally between simulation and reality
4. Human adaptation plays a crucial role not captured by current models

These results motivate the development of our EMG-based human-in-the-loop optimization framework, which addresses these limitations by:

- Adapting to individual users in real-time
- Capturing actual physiological responses rather than predictions
- Enabling rapid re-optimization as users adapt
- Providing frequency-specific tuning within minutes rather than hours

The controllers developed here serve as informed starting points for the EMG-based optimization presented in Chapter 4, demonstrating how simulation and hardware studies can synergistically advance exoskeleton control.

## CHAPTER 4

# EMG-BASED HUMAN-IN-THE-LOOP BAYESIAN OPTIMIZATION FRAMEWORK

### 4.1 Overview

The literature indicates personalization is essential yet difficult to translate from simulation to hardware. Building on this gap, this chapter builds a controller inspired by the simulation shapes and then develops and validates an electromyography (EMG)-driven human-in-the-loop (HIL) optimization framework for rapid, individualized tuning of hip exoskeleton assistance during stationary leg swinging. Manual, expert-driven parameter tuning is time-consuming and does not scale across users or tasks; metabolic-cost objectives, while physiologically meaningful, require long trial durations that increase fatigue and reduce practicality. Surface EMG provides a complementary objective: it is noninvasive, high-bandwidth, and—when processed appropriately—sufficiently stable for short within-session evaluations. Exploiting these properties, the chapter demonstrates a practical pipeline that converts noisy, muscle-level signals into a reliable cost for sample-efficient controller search.

The controller representation is deliberately compact to keep the search tractable while preserving clinically relevant shape flexibility. Torque profiles are expressed with Bézier-derived

---

This content is taken from a published journal article, <https://doi.org/10.3390/biomechanics5020021>

shapes and reduced to four tunable parameters per swing direction, which allows separate forward/backward shaping and straightforward mapping to motor commands. Bayesian optimization with a Gaussian process surrogate and an expected-improvement acquisition function is used to navigate this low-dimensional space under measurement noise. The procedure emphasizes short trials, initialization sampling for coverage, and convergence criteria tuned to within-session stability of the processed EMG metric.

Careful signal processing and convergence detection are integral to the approach. EMG signals are filtered, rectified, smoothed, and normalized to MVC; forward/backward swings are separated by velocity sign and aggregated into single-swing representations for each sensor. A statistical steady-state test is used to ensure that per-trial EMG summaries reflect stable physiological responses rather than transient adaptation, enabling reliable evaluation in tens of seconds instead of minutes. Optimized controllers are validated against three practical baselines (free swinging, device-worn zero-actuation, and a non-personalized general controller) using the EMG objective and complementary subjective effort ratings.

Within the thesis, this chapter operationalizes the transition from simulation-derived templates to user-specific hardware controllers. The simulation–hardware comparisons in the prior chapter provided candidate profile families and highlighted simulation limitations; here those families are parameterized for real-time tuning and adapted to individual users via EMG-HIL optimization. The methods and empirical findings establish that rapid, EMG-based tuning can produce meaningful reductions in muscle activity and perceived effort, and they motivate subse-

quent work on scalability, robustness across tasks, and integration with multi-objective metrics for broader exoskeleton deployment.

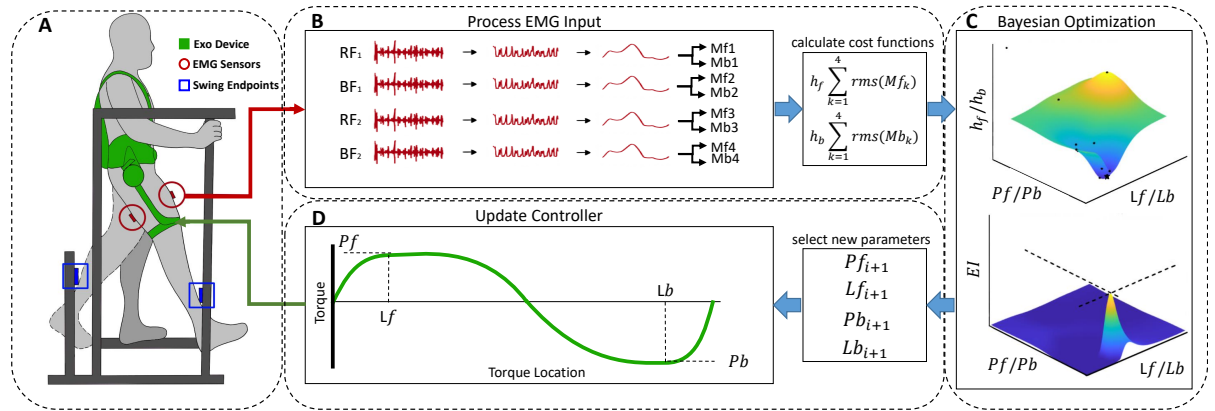


Figure 4. Overview of EMG-HIL Bayesian Optimization. A) Swinging setup (device, sensors, structure). B) EMG processing pipeline (details in Figure 6). C) Bayesian optimization loop tuning four parameters using two cost functions. D) Controller shaping via Bézier parameters.

## 4.2 Methods

### 4.2.1 Hip Exoskeleton Device

The device used in this study is a custom hip exoskeleton intended to assist hip flexion and extension. The device is composed of a 24V Brushless DC (BLDC) motor (AK70-10 T motor, 25Nm peak torque, 8Nm nominal torque), attached by a series of straps (shoulder straps, leg straps, belt) and limited rigid components (plastic braces, aluminum links). The actuation is

provided in a quasi-direct manner with an open-loop torque controller that allows backdriveability. The angle of the hip is measured by an inertial measurement unit (IMU) (Adafruit BNO055, close-loop triaxial 16-bit gyroscope, 100 Hz reading frequency). The device allows for a maximum range of motion between  $-30^\circ$  (extension/posterior) and  $90^\circ$  (flexion/anterior). The hip exoskeleton also contains elements to prevent injury and discomfort. These features include hard stops at the end of the range of motion to prevent over-extension beyond the comfortable range of motion of the human anatomy, two emergency stop buttons (one to stop the torque and the other to shut down the device), and integrated safety checks in the code to ensure the torque magnitude does not exceed 25 Nm.

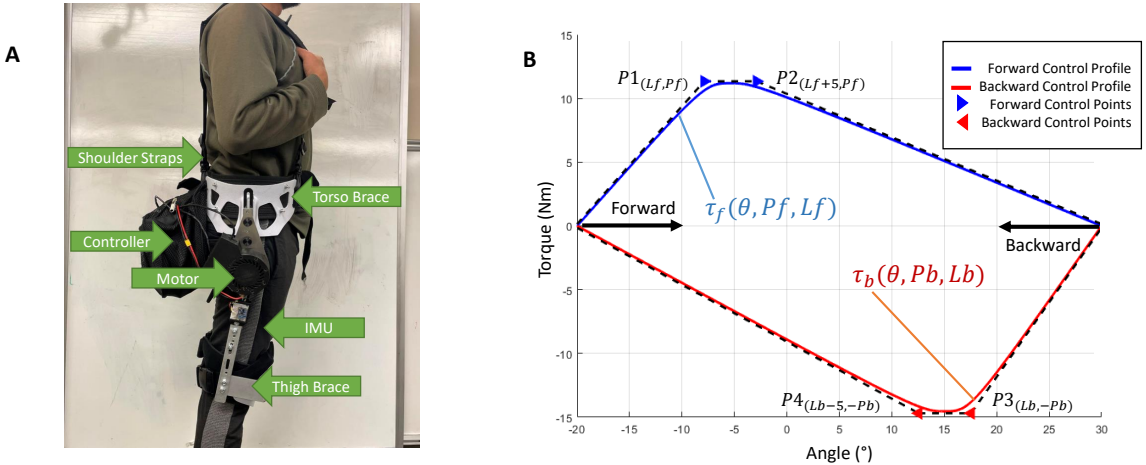


Figure 5. A) An illustration of the exoskeleton device detailing all the main components. B) An overview of the controller constructs a relationship between torque and angle using segmented Bézier curves. The location of the four control points. Control points  $P_1$  and  $P_2$  are dependent on  $P_f$  and  $L_f$  while  $P_3$  and  $P_4$  are dependent on  $P_b$  and  $L_b$ . The torque functions for forward and backward actuation are represented as  $\tau_f$  and  $\tau_b$  respectively.

The control operates on two levels: high-level control occurs within Python 3.9.2 on a Raspberry Pi 4. This controller replicates torque shapes identified as effective in a prior study [126], employing cubic Bézier curves to define torque magnitude versus angle. These curves, comprising four points in a two-dimensional plane across the swing phase (Figure 5 B), require eight inputs: location and magnitude coordinates for each point. The Bézier curves afford flexibility in torque profile shaping without explicit analytic definition.

In this study, the control inputs are further simplified by spacing control points 5° apart and equalizing their magnitudes, reducing the inputs from eight to four. This controller type has shown promising assistance profiles previously [126]. Leg swing control is divided into forward and backward directions, managed separately by a finite state machine (FSM). Transitions between states are triggered by changes in angular velocity, detected by the IMU. To maintain natural swing dynamics, the controller aligns torque direction with velocity direction, ensuring positive work assistance. Control bandwidth is set at 100 Hz.

Low-level control occurs at the motor, where high-level commands are transmitted via the CAN bus protocol to the integrated motor board, operating at 1M Hz

#### **4.2.2 EMG Data**

##### **4.2.2.1 Sensor Data Processing**

EMG sensors (Trigno, Delsys, MA, USA) are placed on the subject's legs. Surface EMG data is collected from the rectus femoris (RF) and bicep femoris (BP) of each leg at a frequency of 1778 Hz. Angle orientation data is collected from the same sensor at a frequency of 148Hz. Each of the four sensors is placed on the respective muscle by following Surface Electromyography

for the Non-Invasive Assessment of Muscles (SENIAM) instructions [127]. SENIAM provides standardized methods for electrode placement to ensure consistency and comparability. Once all sensors are placed, a maximum voluntary contraction (MVC) of each muscle targeted is measured by asking the participant to exert their muscle as much as possible in a safe manner. The MVC values are recorded to be later used for EMG normalization.

The sensor data from the four EMG sensors is processed in MATLAB. The pipeline developed was found to produce the best signal-to-noise ratio in a pilot study and is illustrated in Figure 6. The first step is for each EMG signal to be put through a bandpass filter with limits at 20Hz and 450 Hz. This is followed by an outlier detection algorithm that replaces extreme values that are further than three standard deviations from the mean using modified Akima cubic Hermite interpolation [128] (Figure 6 A). The EMG values are then rectified by taking the absolute value of the signal and subtracting the mean of the non-rectified values to account for the DC offset (Figure 6 B). Once rectified, the signal is smoothed using a three-filter process (Figure 6 C). The first filter applied is a moving max filter with a max window size of 50 data points (less than 0.25% of the total data set length). Next, a small discretization filter is applied to reduce the resolution of the data using bin sizes between 10 and 30. The last filter used is a moving average filter with a maximum window size of up to 400 data points ( $\sim 1.6\%$  of total data length). After smoothing, the data is normalized by dividing the signal by each sensor's respective MVC value allowing the four signals to be combinable (Figure 6 D). Now the angle data is linearly interpolated to match the frequency of the EMG data and then differentiated with respect to time. Velocity data is used to split the EMG data into forward and backward

data sets ( Figure 6 E). Both EMG data sets are now epoched and averaged into a single swing representation ( Figure 6 F). This process produces eight separate representations of the EMG data. Two cost functions, one for forward swing and one for backward swing, are calculated from these eight models by summing the root mean squared of the models in the same direction ( Equation 6.2).

$$h^d = \sum_{n=1}^4 \text{rms}(M_n^d) \quad (4.1)$$

Here  $d = f$  represents data associated with a forward direction, and  $d = b$  represents data associated with a backward direction. The EMG data from the muscle models for the rectus femoris and bicep femoris of the swing leg, and the rectus femoris and the bicep femoris of the stance leg are represented as  $M_1^d, M_2^d, M_3^d, M_4^d$  respectively. This is done for both slow-swing data sets and fast-swing data sets.

#### 4.2.2.2 Data Convergence

To ensure the reliability of data collected within a relatively short acquisition time, it's crucial to confirm its sufficiency and consistency. This involves identifying when the electromyography (EMG) data reaches a steady state. The following mathematical approach is employed to achieve this:

First, the EMG data from all four signals are consolidated into a single matrix, denoted as  $E$ , where  $j$  represents the sample index:

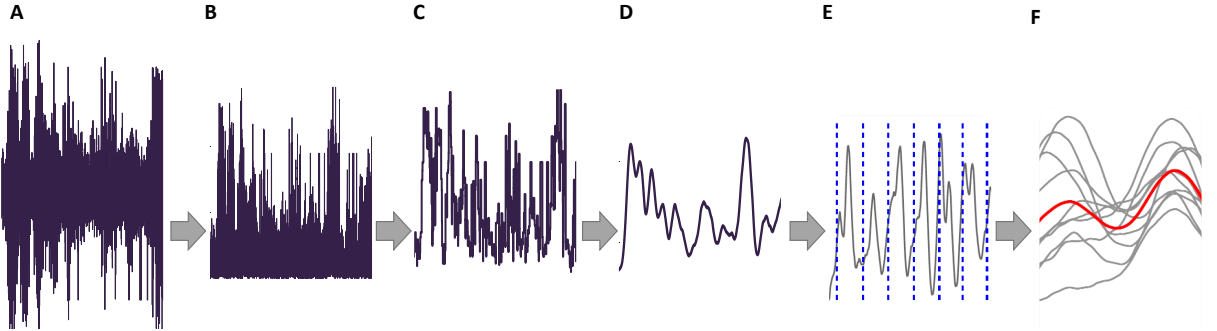


Figure 6. Signal processing includes A) a bandpass filter with a high pass of 20Hz and a low pass of 450 Hz plus an outlier replacement of extreme values beyond 3 standard deviations using a modified Akima cubic Hermite interpolation; B) rectification by taking the absolute value and subtracting the mean value of the previous signal; C) a moving max and discretization filter to outline the shape of the signal; D) a moving average filter to smooth noise followed by normalization against the MVC value for each sensor; E) partitioning the data into separate swings; F) and a data aggregation process using an averaged representation of the epochs produces a single output representation.

$$E_j = \begin{bmatrix} M_{1,j} \\ M_{2,j} \\ M_{3,j} \\ M_{4,j} \end{bmatrix} \quad (4.2)$$

Next, a running average,  $R_i$ , is computed for each column of this matrix using the following equation:

$$R_i = \frac{1}{i} \sum_{j=1}^i E_j \quad (4.3)$$

Subsequently, the rate of change of these running averages is determined using a forward difference method:

$$g_i = \sum_{k=1}^4 (R_{k,i+1} - R_{k,i}) \quad (4.4)$$

These rates of change are aggregated into a single vector  $g$ . To analyze the stability of the signal, we segment this vector into windows using a partition method, with a window size  $w$ , based on a sampling frequency of 2Hz. This frequency is chosen to balance refined detection (minimal lag) and an ample search window:

$$B_i = \begin{bmatrix} g_{(i-1)w+1} & g_{(i-1)w+2} & \dots & g_{iw} \end{bmatrix} \quad (4.5)$$

To discern when the combined rate of change of the EMG signals no longer significantly differs from zero, indicating a steady state, statistical analysis is applied to this vector. At each window, a two-sample z-test is conducted, comparing the mean rate of change in the current window ( $i$ ) with that of the previous window ( $i - 1$ ):

$$H_0 : \mu(B_i) = \mu(B_{i-1}) \quad (4.6)$$

$$H_1 : \mu(B_i) \neq \mu(B_{i-1}) \quad (4.7)$$

The z-test statistic is calculated as:

$$z = \frac{\bar{B}_i - \bar{B}_{i-1}}{\sqrt{\frac{\sigma_{B_i}^2}{n_i} + \frac{\sigma_{B_{i-1}}^2}{n_{i-1}}}} \quad (4.8)$$

where  $\bar{B}_i$  and  $\bar{B}_{i-1}$  are the sample means,  $\sigma_{B_i}^2$  and  $\sigma_{B_{i-1}}^2$  are the sample variances, and  $n_i$  and  $n_{i-1}$  are the sample sizes of the current and previous windows, respectively.

The p-value is calculated from the z-test statistic using the standard normal distribution:

$$p = 2 \cdot (1 - \Phi(|z|)) \quad (4.9)$$

where  $\Phi$  is the cumulative distribution function of the standard normal distribution. A p-value greater than 0.95 supports the null hypothesis, indicating no significant difference between the means.

To further confirm convergence, a correlation analysis is performed at each window. This analysis assesses the linear relationship between the rate of change in the current window and the previous window using the Pearson correlation coefficient. The Pearson correlation coefficient  $C_i$  is calculated as follows:

$$C_i = \frac{\text{cov}(B_i, B_{i-1})}{\sigma_{B_i} \sigma_{B_{i-1}}} \quad (4.10)$$

where  $\text{cov}(B_i, B_{i-1})$  is the covariance between the two windows, and  $\sigma_{B_i}$  and  $\sigma_{B_{i-1}}$  are the standard deviations of the current and previous windows, respectively. A typical correlation

coefficient value around 0.8 indicates a strong linear relationship, but the maximum observed value is used for determining convergence.

The convergence point of the signal is determined by identifying the steady-state time,  $t_{\text{steady-state}}$ , which is the final time stamp of the window where both conditions have been met: the p-value exceeds 0.95 and the correlation coefficient has reached its maximum positive value:

$$t_{\text{steady-state}} = \max(i \mid p > 0.95 \cap \max(C)) \quad (4.11)$$

By combining these methods, we can accurately determine when the EMG data reaches a steady state, ensuring the reliability of the collected data. The chosen p-value threshold of 0.95 ensures a high statistical significance, reflecting a negligible difference between window means. This two-factor method, involving both the z-test and Pearson correlation, was found to be sufficient for confirming steady-state convergence without the need for additional statistical methods.

#### 4.2.3 Experimental Protocol

The study is approved by the University of Illinois at Chicago Institutional Review Board (STUDY 1022-2022). A one-day protocol is conducted with eight healthy participants (age:  $26.3 \pm 3.2$  years; weight:  $64.6 \pm 3.47$  kg; height:  $165.33 \pm 11.13$  cm, male: 5, female: 3). Subjects are asked to swing their right leg while their upper torso is supported by a custom rigid structure. The structure restricts the leg swing within a desired angle range ( $-20^\circ$  to  $30^\circ$  from the vertical) using bumpers. Two swing frequencies, corresponding with normal walking frequencies [129], are tested (0.67 Hz and 0.83 Hz). These frequencies are encouraged via the

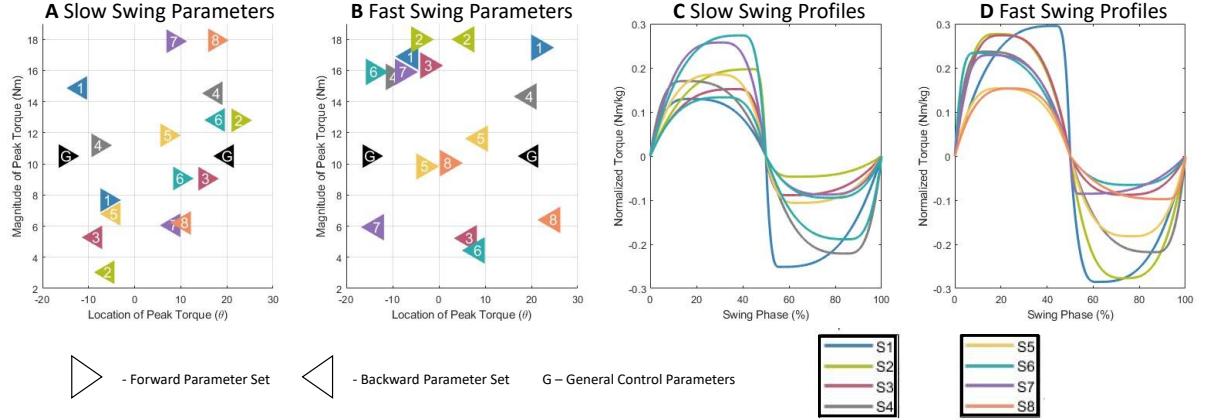


Figure 7. This figure presents a comprehensive view of the swing controller concerning both controller parameters and torque profiles. A,B) Plots displaying the spatial distribution of controller parameters during the slow swing and fast swing. The x-axis represents the location, and the y-axis denotes the magnitude. C,D) showcasing the torque profile for the slow and fast swing, with the x-axis indicating the swing phase as a percentage, and the y-axis representing the weight-normalized torque.

use of a metronome which provides the audible cue at which to make contact with each bumper.

Participants are instructed to swing their leg at the beat of the metronome such that they make gentle contact with each bumper at each beat (Figure 23 A). To account for two contacts per swing, the metronome is played at twice the desired swing frequency. A work-to-rest ratio of 1:2 is kept consistent throughout the experiment to reduce the effects of fatigue.

The three-hour experiment consists of four main sections: acclimation, parameter optimization, and validation.

#### 4.2.3.1 Acclimation

During the acclimation section, subjects are exposed to nine different parameter sets for each swing frequency. The parameter sets are selected using a Latin hypercube sampling (LHS) to provide an even distribution of the parameter space. Each parameter set is supplied for 30-second trials in clusters of three before allowing rest. This results in three slow-frequency clusters and three fast-frequency clusters, each followed by a rest period of 90 seconds. The main focus of this section is to allow participants to learn how to interact with the assistance provided by the device before tuning.

#### 4.2.3.2 HIL Optimization

We utilize Bayesian optimization as a robust method to identify the optimal set of parameters when the objective function is noisy and expensive to evaluate. The approach entails constructing a probabilistic surrogate model of the objective function based on posterior data that incorporates a prior distribution. By leveraging this model to predict outcomes for different parameter settings, it can select the next parameter setting to evaluate through an acquisition function that uses a strategic trade-off between exploration (trying new settings) and exploitation (utilizing the best-known settings) [130]. In this study, the probabilistic model adopted is a Gaussian Process (GP).

A GP model is a powerful, non-parametric method for modeling distributions over functions. It is fully specified by its mean function,  $m(\mathbf{x})$ , and covariance function,  $k(\mathbf{x}, \mathbf{x}')$ . For simplicity, we often assume the mean function is zero,  $m(\mathbf{x}) = 0$ .

The GP prior over function values at the training points  $\mathbf{X}$  is given by:

$$p(\mathbf{f}|\mathbf{X}) = \mathcal{N}(\mathbf{f}|\mathbf{0}, \mathbf{K}), \quad (4.12)$$

where  $\mathbf{K}$  is the covariance matrix computed using the covariance function  $k(\mathbf{x}, \mathbf{x}')$ .

Given a set of training data  $(\mathbf{X}, \mathbf{f})$  and new test points  $\mathbf{X}_*$ , the joint distribution of the observed function values  $\mathbf{f}$  and the function values at the test points  $\mathbf{f}_*$  is:

$$\begin{pmatrix} \mathbf{f} \\ \mathbf{f}_* \end{pmatrix} \sim \mathcal{N}\left(\mathbf{0}, \begin{pmatrix} \mathbf{K} & \mathbf{K}_* \\ \mathbf{K}_*^T & \mathbf{K}_{**} \end{pmatrix}\right), \quad (4.13)$$

where  $\mathbf{K} = k(\mathbf{X}, \mathbf{X})$ ,  $\mathbf{K}_* = k(\mathbf{X}, \mathbf{X}_*)$ , and  $\mathbf{K}_{**} = k(\mathbf{X}_*, \mathbf{X}_*)$ .

Using standard rules for conditioning Gaussians, the posterior distribution of the function values at the test points is given by:

$$p(\mathbf{f}_*|\mathbf{X}_*, \mathbf{X}, \mathbf{f}) = \mathcal{N}(\mathbf{f}_*|\boldsymbol{\mu}_*, \boldsymbol{\Sigma}_*), \quad (4.14)$$

where the posterior mean  $\boldsymbol{\mu}_*$  and the posterior covariance  $\boldsymbol{\Sigma}_*$  are:

$$\boldsymbol{\mu}_* = \mathbf{K}_*^T \mathbf{K}^{-1} \mathbf{f}, \quad (4.15)$$

$$\boldsymbol{\Sigma}_* = \mathbf{K}_{**} - \mathbf{K}_*^T \mathbf{K}^{-1} \mathbf{K}_*. \quad (4.16)$$

The kernel function  $k(\mathbf{x}, \mathbf{x}')$  plays a crucial role in defining the covariance between points. The kernel used in this study is an Automatic Relevance Determination (ARD) squared exponential kernel, given by:

$$k(\mathbf{x}, \mathbf{x}') = \sigma_f^2 \left( 1 + \sqrt{5}r + \frac{5}{3}r^2 \right) \exp(-\sqrt{5}r), \quad (4.17)$$

where

$$r = \sqrt{\sum_{i=1}^d \frac{(x_i - x'_i)^2}{\ell_i^2}}, \quad (4.18)$$

and  $\sigma_f^2$  is the signal variance,  $\ell_i$  is the length-scale parameter for the  $i$ -th dimension, and  $d$  is the dimensionality of the input space.

The acquisition function employed in the optimization process is the Expected Improvement (EI) function. This function quantifies the expected improvement in the objective function over the best-known value. The next parameter set to evaluate is determined by maximizing the EI function, where  $f_{\text{best}}$  is the best-known value of the objective function, and the expectation is taken over the posterior distribution of the Gaussian Process (GP).

The Expected Improvement (EI) at a new point  $\mathbf{x}$  is defined as:

$$\text{EI}(\mathbf{x}) = (\mu(\mathbf{x}) - f_{\text{best}} - \xi)\Phi(Z) + \sigma(\mathbf{x})\phi(Z), \quad (4.19)$$

where:

$$Z = \frac{\mu(\mathbf{x}) - f_{\text{best}} - \xi}{\sigma(\mathbf{x})}, \quad (4.20)$$

$\mu(\mathbf{x})$  is the predicted mean,  $\sigma(\mathbf{x})$  is the predicted standard deviation,  $\Phi(Z)$  is the cumulative distribution function (CDF) of the standard normal distribution,  $\phi(Z)$  is the probability density function (PDF) of the standard normal distribution, and  $\xi$  is a parameter that balances exploration and exploitation. A higher  $\xi$  encourages exploration by favoring points with higher uncertainty, while a lower  $\xi$  favors exploitation by focusing on areas with high predicted mean.

The determination of the next sample parameter set follows the maximization of the EI function:

$$\mathbf{x}_{n+1} = \arg \max_{\mathbf{x}_*} \text{EI}(\mathbf{x}_*), \quad (4.21)$$

where the  $\arg \max$  function returns the parameter set which maximizes the EI in the parameter space  $\mathbf{x}_*$ .

By maximizing the EI function, the optimization process strategically selects the next parameter setting to evaluate, balancing the trade-off between exploring new areas (high uncertainty) and exploiting known good areas (high mean predictions) [130].

The human-in-the-loop Bayesian optimization procedure involves a maximum of 12 trials for each swing frequency, each lasting 15 seconds. The selection of the maximum number of trials is based on observed convergence during the pilot test. To streamline the process, both swing

frequencies are optimized concurrently within the same run, with the slower frequency sampled first, followed by a 10-second rest period, and then the faster frequency.

The initial four trials serve as initialization trials, allowing for sampling of the parameter space before the Bayesian optimization begins to select new parameter sets using the acquisition function. This optimization is conducted for up to eight trials to tune the two parameters for the forward and backward swing controllers in parallel, resulting in a total of two controllers with two phases each (four parameters per controller) being tuned synchronously. These controllers consist of a slow frequency controller with its forward and backward phases, and a fast frequency controller with its forward and backward phases.

Convergence is achieved when the same parameter set produces the best-performing controller three times within an allowable variation of  $\pm 10\%$ . All eight parameter sets must converge before the optimization is stopped. If this condition is not met, the experiment continues until the maximum number of search iterations is reached. The optimal controller is determined as the best-performing parameter set estimated by the Bayesian algorithm.

#### **4.2.3.3 Validation**

Following the identification of the optimal parameter set, its performance is evaluated against three baselines:

- No exoskeleton (NE), where the subject performs free swinging.
- Zero actuation (ZA), where the subject wears the device but it remains unpowered.

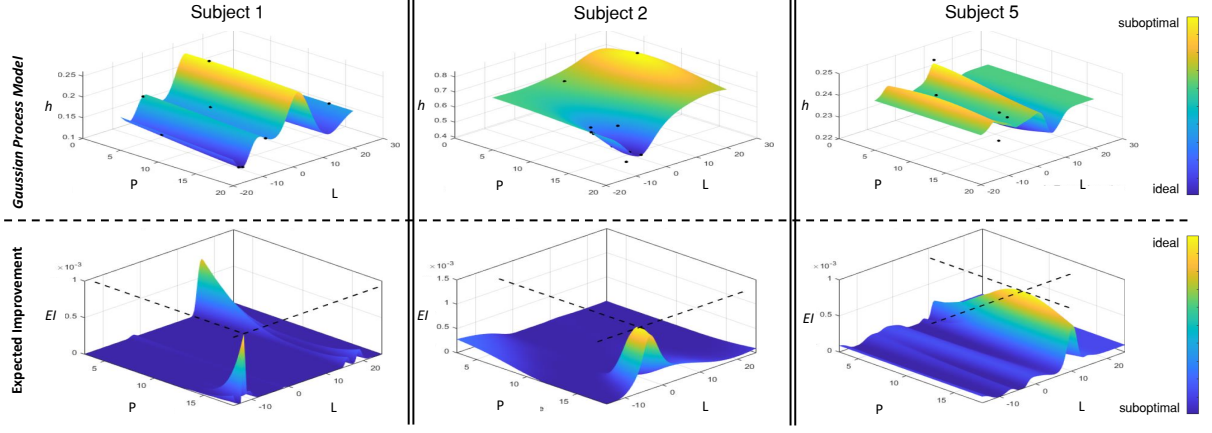


Figure 8. Three samples of the surrogate and acquisition function optimization landscapes from Bayesian. The  $h$  variable represents the cost function,  $P$  and  $L$  are the two parameters tuned, and  $EI$  is the expected improvement for each parameter set. Lower values are favorable for the Gaussian process model and higher values are favorable for the expected improvement function.

- General control (GC), where the subject receives assistance from a predefined intuition controller supplying a magnitude of torque equivalent to the mean of the possible torque values at the beginning of each half swing.

The performance of the optimal and baseline conditions for each swing frequency is tested three times. During each iteration, a performance metric equivalent to the cost function (Equation 6.2) is calculated.

$$\% \Delta = 100 \left( \frac{\mu_{\text{optimal}} - \mu_{\text{baseline}}}{\mu_{\text{baseline}}} \right) \quad (4.22)$$

Each condition is represented by the mean value of the three observations. The percent change between the optimal mean ( $\mu_{\text{optimal}}$ ) and the mean of each baseline ( $\mu_{\text{baseline}}$ ) is then calculated. ( Equation 4.22).

Data collection and processing for each trial follow the same protocol as the tuning trials. Any outliers in the data are identified and replaced with the center value of the data if they deviate by more than three standard deviations from the mean.

Statistical analysis between two conditions is paired. Since the data from most conditions are not normally distributed (Shapiro-Wilk test,  $p < .05$ ), a non-parametric Wilcoxon test is used to assess the statistical significance of the comparison [131]. The null hypothesis assumes that the average percent change between the optimal and a particular baseline is zero, with a significance level of  $p < .05$ .

Additionally, each subject's perceived effort is rated according to Borg's scale. While subjective, the Borg Scale has been shown to correlate well with physiological measures such as heart rate, lactate levels, and oxygen consumption. This makes it a reliable complement to the EMG objective measurements in assessing the effectiveness and impact of the exoskeleton [132].

### 4.3 Results

One critical aspect of working with EMG is ensuring the stability of physiological data. All trial data for each subject were averaged and evaluated for steady state using the method described in Equation 4.2 to Equation 4.11. The steady-state time average for each subject is shown in Figure 10, where the convergence of the rate of change of a running average of the

summed EMG data is plotted against time. The data stabilizes in under 15 seconds for each subject, with no trial exceeding this duration.

The optimal controller (OP) outperformed all baseline conditions on average (Figure 9). For the slow swing, OP reduced muscle activity by 15.2% ( $p < 1e-7$ ) compared to the no device condition and by 19.7% ( $p < 1e-4$ ) compared to the zero torque condition. Additionally, the OP reduced muscle activity by 14.5% ( $p < 1e-4$ ) compared to the general controller. For the fast swing, OP significantly reduced muscle activity compared to the no device and zero torque conditions by 17.0% ( $p < 1e-4$ ) and 23.6% ( $p < 1e-4$ ), respectively, and by 15.6% ( $p = 0.0015$ ) compared to the fast swing general controller.

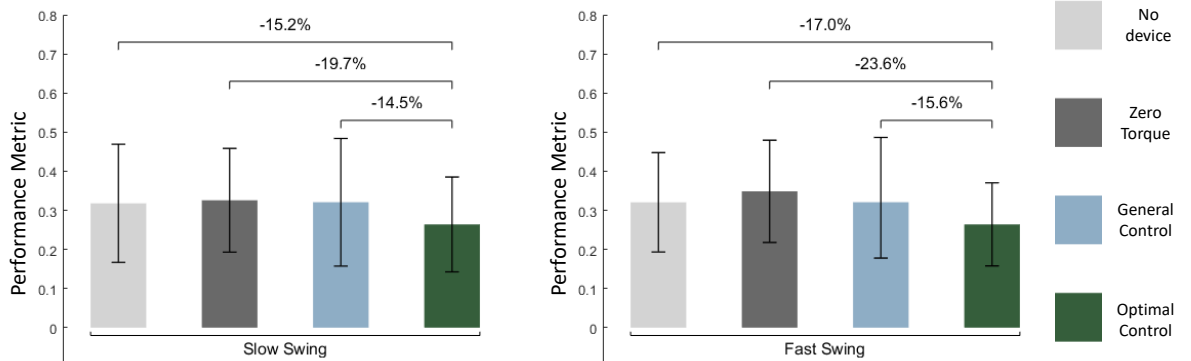


Figure 9. Condition comparison results from the validation phase. The condition averages of the EMG performance metric are represented by the bar graph. The standard deviation is shown by whiskers. Percent changes between tests with three baseline conditions and tests with optimal control are shown above the horizontal brackets.

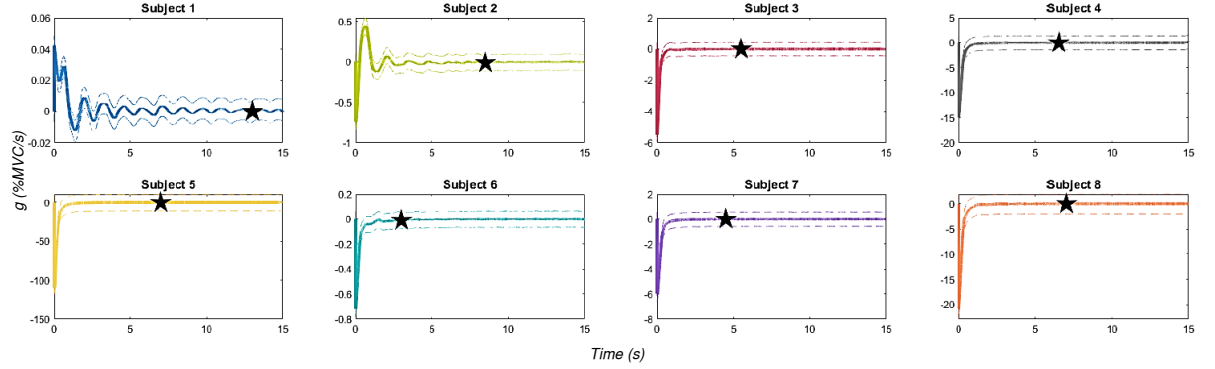


Figure 10. The convergence data for each subject is represented as a bold average line with dotted lines showing the standard deviation. The variable  $g$  represents the sum of the derivative of the running average for the four sensors across all trials of a subject. The star indicates the time when a steady state is reached on average.

In terms of Borg scale values, the optimal controller is perceived to lower effort compared to most baselines. The percent change in mean Borg values between the optimal and each baseline condition is shown in Table III, calculated using Equation 4.22.

A preferred parameter set was found within eight search iterations, with an early stop condition met for seven out of eight subjects. For the eighth subject, all parameters except one (Lb) converged, indicating a strong preference by the acquisition function. The average number of trials required to tune for the eight subjects was 9.5 with a standard deviation of 1.87.

#### 4.4 Discussion

The optimization process demonstrates a well-performing ability to tune quickly and effectively, resulting in a noteworthy reduction of muscle activity compared to all baselines. In

TABLE III

## BORG VALUE COMPARISON AGAINST BASELINES FOR VALIDATION

Baseline	% change	
	Opt. Slow	Opt. Fast
No Device	-26.0%	-14.4%
Zero Assistance	-39.5%	-26.8%
General Control	-18.5%	4.9%

particular, the results establish the advantage of an optimal controller over arbitrary assistance, heavily indicating that tuning is a necessity. The use of EMG data for tuning is validated by the effectiveness of the tuning process, positioning EMG as a rapid and effective alternative to metabolic cost. The study achieves four times faster tuning compared to metabolic cost-based approaches [133], showcasing a significant advancement. When compared with prior EMG HIL optimization studies [134], our approach stands out by achieving tuning in as little as 142 seconds with consistent controller performance. These contributions enhance the practicality and applicability of EMG-based optimization.

The Borg scale results serve to add a layer of validation to the need for the optimization process. The values in Table III show that the assistance from the optimal controller provided a noticeable aid while swinging. The values of percent change from the baseline show that most subjects not only preferred the optimal condition but that there was also a significant reduction in the perceived effort across the comparison against the baseline conditions. Overall, the Borg

scale data helps solidify the evidence that the optimal controller is noticeably preferred as is suggested by EMG performance data.

In addition to being able to optimize properly, the convergence of the EMG signal within 15 seconds showcases that the signal is capable of being harvested very quickly. This process stabilizes the signals and improves their SNR significantly. This work suggests that EMG might be a good measure for optimizing exoskeletons efficiently. The data processing methods showcase the utility of EMG despite its inherent noise.

The study design has limitations, including reliance on a single physiological metric for validation and a limited subject pool. Despite improvements in EMG performance criteria, significant measurement variance remains. Future research should employ multiple physiological metrics for cross-validation and include a larger subject pool for better correlation analysis. Additionally, exploring more demanding activities like squatting or walking would enhance evaluation.

#### 4.5 Conclusion

The importance of this study lies in its ability to achieve fast and effective controller tuning and improved EMG processing for optimization. The findings indicate that EMG optimization is not only quick and effective but also worthy of further investigation. The study advances our understanding of rapid EMG optimization, offering promising potential for future research and practical applications in the development of exoskeleton controllers.

# CHAPTER 5

## MACHINE LEARNING ENHANCEMENT OF BAYESIAN OPTIMIZATION INITIALIZATION

### 5.1 Overview

While the previous chapter achieves rapid tuning, this chapter investigates whether readily measured user characteristics can be used to guide the initialization of a Bayesian HIL search so that the optimization begins in regions of the parameter space that are more likely to contain high-quality controllers. The EMG-based HIL framework developed in the previous chapter produces rapid, individualized controllers but still relies on broadly distributed initialization (Latin hypercube sampling). Such uniform initialization implicitly treats all regions as equally promising and therefore expends trials exploring low-quality areas. Here we ask whether a lightweight, data-driven prediction of promising parameter regions—derived from simple anthropometrics—can meaningfully improve final controller performance and reduce the time required to reach it.

The technical strategy combines three elements. First, anthropometric measurements are transformed into a compact set of biomechanically informed predictors (both raw measures and derived indices) that plausibly correlate with torque requirements for leg swinging. Second,

---

Parts of this chapter are taken from a published conference paper, MECC 2024, October 2024

we use controlled data-synthesis and population-informed normalization to expand the small experimental dataset while preserving physiological plausibility; this expansion is necessary to train reliable classifiers without collecting impractically large numbers of new experiments. Third, binary classification models are trained to predict whether each controller parameter should lie above or below a population median; the resulting quadrant prediction constrains the HIL initialization to 25% of the original search space. Multiple classifier families are evaluated for accuracy and interpretability before selecting a deployment model that balances performance with transparency.

Validation experiments compare standard (full-space) Latin hypercube initialization to ML-guided initialization while holding the remainder of the Bayesian HIL protocol constant. The ML pipeline increases the effective training set size via interpolation that respects observed correlations and population bounds, yields classification accuracy on the order of 75%, and produces consistent gains when used to seed optimization. Across the held-out participants studied here, ML-guided initialization produced a statistically significant improvement in final EMG-based performance (mean improvement 9.98%,  $p = 0.012$ ) and a substantial reduction in trials to convergence (26.5% fewer trials). These gains accrue because the optimization spends fewer early trials exploring low-yield regions and more trials refining high-quality solutions, while the Bayesian loop still retains the freedom to escape a poor prediction if necessary.

Conceptually and practically, the chapter situates machine learning as a complement, not a replacement, to HIL optimization. Predictive initialization supplies better starting conditions that materially ease the optimization burden; the Bayesian HIL mechanism remains responsible

for adapting controllers to each user’s real physiological response. The methods and results reported here therefore extend the thesis’s trajectory from simulation-derived templates (Chapter 3) and EMG-driven adaptation (Chapter 4) toward increasingly data-efficient, scalable personalization. Limitations are noted—discrete class prediction (rather than continuous regression), activity specificity, and dependence on structural rather than functional measurements—but the findings point to clear extensions (richer feature sets, online updating, and regression-based initialization) that will be pursued in subsequent work on multi-objective and higher-dimensional controller tuning.

## 5.2 Methods

### 5.2.1 Data Foundation

We use experimental data from the EMG-HIL optimization study described in Chapter 4, which involved eight healthy participants optimizing controllers for leg swinging at two frequencies. A summary of this precursor HIL optimization framework is shown in Figure 11. The experiment utilized a custom hip exoskeleton (Figure 12, left) to assist with leg swinging, where the control strategy shaped a torque profile based on angular position (Figure 12, right).

Each participant provided six anthropometric measurements: height, weight, body fat percentage, leg circumference, leg weight, and leg length. From these measurements, we derived six additional features that capture biomechanically relevant relationships, including body mass index (BMI), lean mass, estimated leg strength, leg volume, lean mass index (LMI), and lean leg density. Table IV details these predictive features and their calculations.

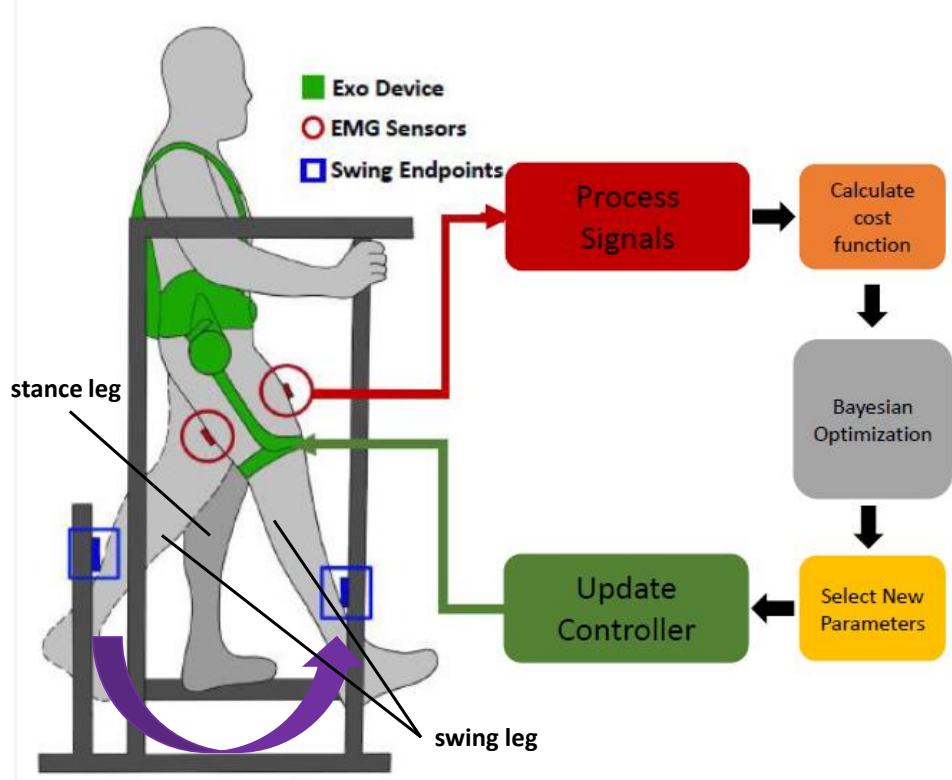


Figure 11. Overview of EMG-HIL Bayesian Optimization established in precursor work.

The optimization process for each participant yielded eight controller parameters: forward peak location ( $P_f$ ), forward peak magnitude ( $L_f$ ), backward peak location ( $P_b$ ), and backward peak magnitude ( $L_b$ ) for both slow and fast swing frequencies. These parameters serve as the prediction targets for our machine learning models.

### 5.2.2 Data Processing Pipeline

The data processing pipeline (Figure 13) transforms the limited experimental data into a comprehensive dataset suitable for machine learning while preserving physiological validity. The

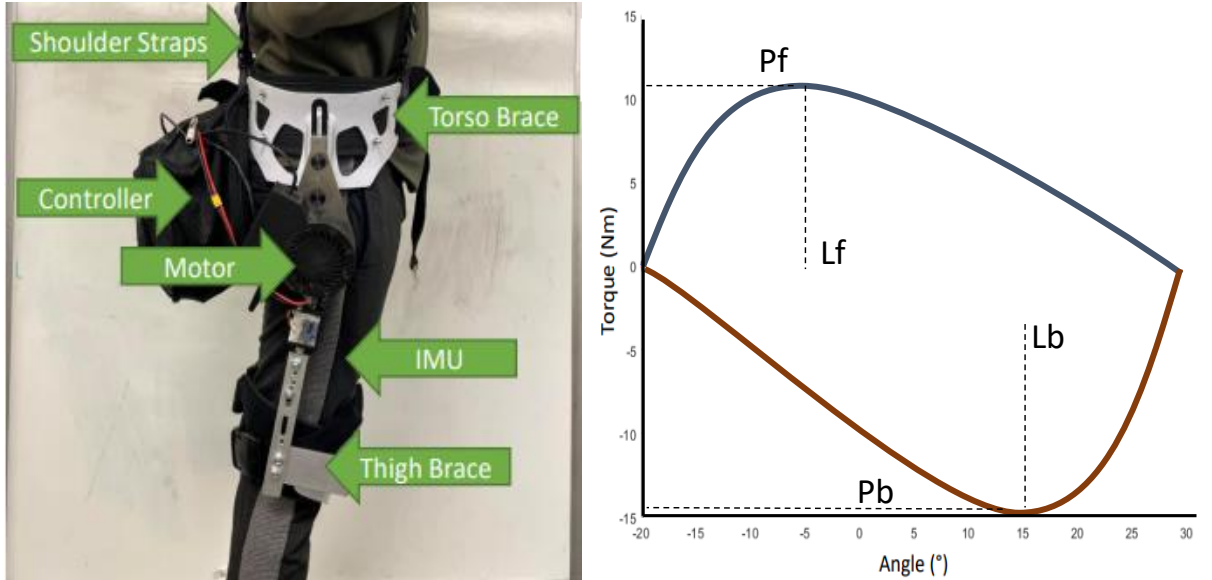


Figure 12. Left) An illustration of the exoskeleton device used, highlighting important features. Right) An illustration of the relationship between torque and angle.

pipeline consists of several stages designed to address specific challenges in working with small anthropometric datasets.

#### 5.2.2.1 Population-Informed Normalization

To ensure our models generalize beyond the specific participants in our study, we integrate population anthropometric data from NASA's anthropometry database [135]. We model the combined distribution of each anthropometric variable using Gaussian Mixture Models (GMM), which capture the multimodal nature of human body measurements across diverse populations. From these GMMs, we generate 1000 samples per variable to establish robust normalization

TABLE IV

 ANTHROPOMETRIC PREDICTIVE FEATURES USED FOR CONTROLLER  
 PARAMETER PREDICTION

Predictor	Symbol/Equation	Units
Height	$h$	cm
Weight	$w$	kg
Body fat	$b$	%
Leg circumference	$L_c$	cm
Leg weight	$L_w$	kg
Leg length	$L_n$	cm
BMI	$w/h^2$	kg/m <sup>2</sup>
Lean Mass	$w(1 - b)$	kg
Leg Strength	$L_w/L_n$	kg/m
Leg Volume	$4\pi L_n L_c^2$	m <sup>3</sup>
LMI	$w(1 - b)/h^2$	kg/m <sup>2</sup>
Lean Leg Density	$L_w(1 - b)/(4\pi L_n L_c^2)$	kg/m <sup>3</sup>

bounds that prevent extrapolation errors when encountering new subjects outside our original data range.

### 5.2.2.2 Feature Selection via Regularization

Given the high correlation among anthropometric measurements, we employ elastic net regularization to identify the most informative predictors for each output parameter. Elastic net combines L1 (Lasso) and L2 (Ridge) penalties with a mixing parameter  $\alpha = 0.5$ , balancing feature selection with coefficient stability. For each of the eight output parameters, we retain the four predictors with the largest average coefficient magnitudes across multiple regularization strengths, reducing multicollinearity while preserving predictive power.

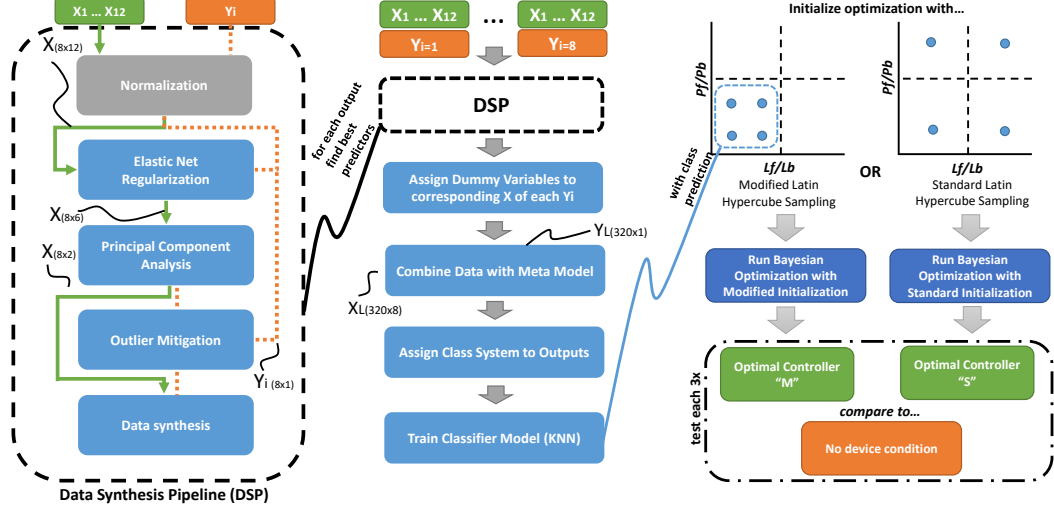


Figure 13. An overview of the machine learning pipeline and its application in the initialization of Bayesian HIL optimization. Matrix dimensions are indicated in parentheses, and  $P_f$ ,  $P_b$ ,  $L_f$ , and  $L_b$  refer to the control parameters.

### 5.2.2.3 Dimensionality Reduction

We apply Principal Component Analysis (PCA) to the selected features, projecting the data onto the first two principal components. This transformation serves dual purposes: further reducing dimensionality for visualization and creating orthogonal features that facilitate subsequent outlier detection. The two-component representation typically captures 85-95% of the variance in the selected features while enabling robust linear modeling in the reduced space.

### 5.2.2.4 Outlier Detection and Mitigation

In small datasets, individual outliers can disproportionately influence model training. We identify outliers by fitting robust linear models between principal components and output val-

ues, flagging points with residuals exceeding three median absolute deviations. Rather than discarding these points, we replace them with model predictions, preserving dataset size while reducing the influence of anomalous measurements that may result from measurement error or exceptional physiological characteristics.

#### **5.2.2.5 Controlled Data Synthesis**

To augment our dataset while maintaining realistic relationships between variables, we employ modified Akima cubic Hermite interpolation [128]. This method generates synthetic data points that follow the natural curves defined by real observations without introducing artificial oscillations. We generate synthetic points at a 4:1 ratio to real data, empirically determined to balance model training requirements with preservation of original data characteristics. Each synthetic point respects the correlations and constraints present in the original dataset, ensuring physiological plausibility.

#### **5.2.3 Classification Model Development**

The augmented dataset enables training of classification models that predict whether each controller parameter should be "high" or "low" relative to the median value. This binary classification approach simplifies the prediction task while providing sufficient guidance for optimization initialization. We evaluate three classification algorithms with complementary strengths. Logistic regression provides interpretable linear decision boundaries, support vector machines (SVM) capture non-linear relationships through kernel transformations, and k-nearest neighbors (KNN) leverages local similarity in the feature space. Each model undergoes hyperparameter optimization via 5-fold cross-validation grid search, ensuring robust performance estimates. The

final prediction system combines individual binary classifiers for each parameter into a unified model that accepts a subject's anthropometric measurements and outputs a predicted quadrant in the 4-dimensional parameter space for each swing frequency. This quadrant prediction constrains the Bayesian optimization initialization to 25% of the original search space.

#### 5.2.4 Experimental Validation

To assess the impact of ML-guided initialization, we conduct a controlled comparison using the same EMG-HIL optimization protocol from Chapter 4. New participants undergo anthropometric measurement, after which our trained models predict their likely optimal parameter quadrant. We then run two optimization sessions:

1. Standard initialization using Latin hypercube sampling across the full parameter space.
2. ML-guided initialization with Latin hypercube sampling constrained to the predicted quadrant.

Both conditions use identical Bayesian optimization settings, with convergence criteria and maximum trial limits matching the original protocol. Following optimization, we validate the resulting controllers against a no-exoskeleton baseline, computing the percent reduction in EMG-based cost function:

$$\% \Delta = \frac{\mu_{\text{optimal}} - \mu_{\text{baseline}}}{\mu_{\text{baseline}}} \times 100$$

This metric directly assesses whether ML-guided initialization leads to better final controllers, not just faster convergence.

### 5.3 Results

#### 5.3.1 Data Synthesis Validation

The controlled data synthesis process successfully expanded our dataset from 8 to 320 training examples while preserving key statistical properties. Analysis of the synthetic data confirmed that mean values remained within 2% of the original data for all features, while correlation structures showed Pearson coefficients within 0.05 of original values. The Kolmogorov-Smirnov test failed to reject the null hypothesis of identical distributions for any feature ( $p > 0.10$ ), indicating successful preservation of data characteristics. Visual inspection of the augmented dataset in principal component space revealed smooth interpolation between original data points without clustering artifacts or distribution gaps. The synthetic points filled regions of feasible anthropometric combinations while respecting physiological constraints, such as maintaining realistic relationships between height, weight, and body composition.

#### 5.3.2 Classification Performance

Cross-validation results demonstrated robust classification performance across all three model types. Logistic regression achieved  $72.3\% \pm 4.1\%$  accuracy, while SVM with radial basis function kernels reached  $74.8\% \pm 3.7\%$ . The KNN classifier ( $k=5$ ) performed best at  $76.2\% \pm 3.5\%$  accuracy. Given the relatively small performance differences and the interpretability advantage of logistic regression, we selected it for deployment in the initialization system. Feature importance analysis revealed that lean leg density and leg strength ratio were the most predictive features for forward swing parameters, while BMI and total lean mass better predicted backward swing

parameters. This distinction aligns with biomechanical expectations, as forward swing requires active hip flexion against gravity while backward swing involves controlled deceleration.

### 5.3.3 Optimization Enhancement

The ML-guided initialization demonstrated clear benefits in the optimization process. Across six new participants, the enhanced approach achieved an average  $9.98\% \pm 3.2\%$  greater reduction in EMG cost compared to standard initialization. This improvement was statistically significant ( $p = 0.012$ , paired t-test) and consistent across participants. Figure 39 illustrates the typical performance improvement observed when comparing a controller tuned with ML-guided initialization against one tuned with standard initialization and a no-device baseline. Beyond final performance, ML-guided initialization also accelerated convergence. The number of trials required to meet convergence criteria decreased from  $9.8 \pm 2.1$  to  $7.2 \pm 1.6$ , representing a 26.5% reduction in optimization time. This acceleration occurred because the optimization began in regions with higher-quality solutions, reducing the exploration phase of Bayesian optimization.

## 5.4 Discussion

### 5.4.1 Bridging Individual Differences Through Data

The success of anthropometric-based parameter prediction validates the hypothesis that optimal exoskeleton assistance relates systematically to user characteristics. While individual motor control strategies introduce variability that prevents perfect prediction, our results demonstrate that even coarse-grained classification provides valuable guidance for optimization initialization. The 75% classification accuracy, while leaving room for improvement, proves sufficient to meaningfully enhance the optimization process. The feature importance patterns align

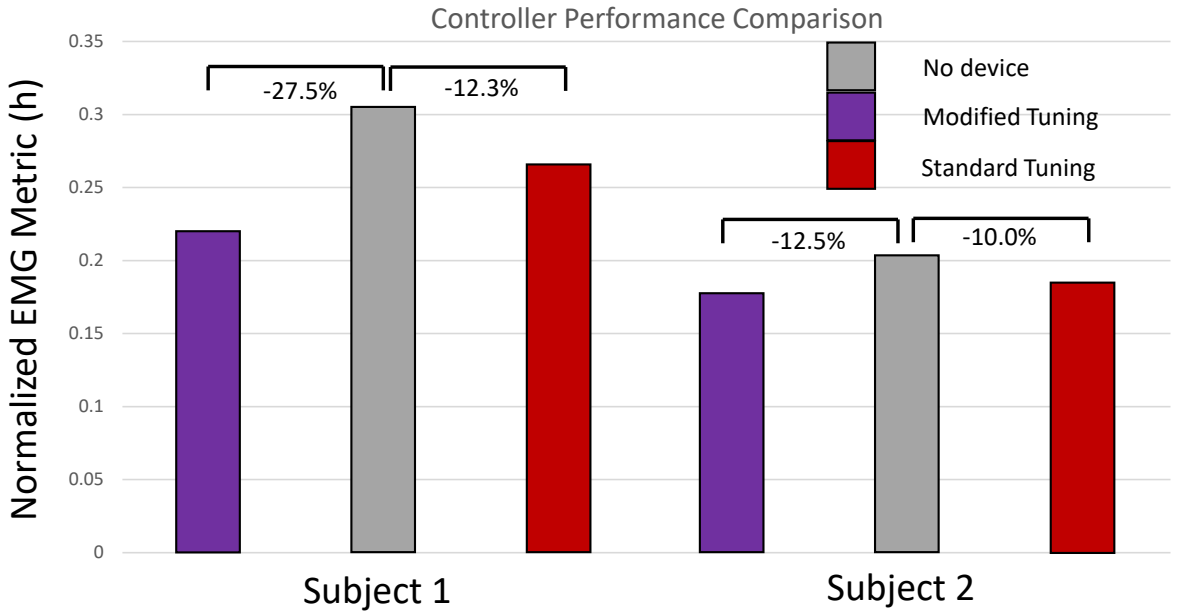


Figure 14. Performance comparison between the two controllers tuned with and without the developed method against a baseline of no device.

with biomechanical principles. Lean leg density and strength metrics predict forward swing assistance because these features relate to the force-generating capacity needed for active hip flexion. Conversely, overall body metrics better predict backward swing parameters, reflecting the whole-body dynamics involved in controlling the passive swing return. These interpretable relationships increase confidence in the model's generalization to new populations.

#### 5.4.2 Data Synthesis as an Enabling Technology

Our results demonstrate that carefully designed data synthesis can overcome the small-sample limitations endemic to exoskeleton research. The key to success lies in respecting the

constraints and correlations present in real physiological data. By using population databases to inform normalization and employing interpolation methods that preserve smoothness, we generated synthetic data that enhanced model training without introducing artifacts. The 4:1 synthesis ratio emerged as a practical balance through empirical testing. Lower ratios provided insufficient training data for robust classification, while higher ratios began to smooth away individual variations that carry predictive information. This finding suggests general guidelines for data synthesis in biomechanical applications: augmentation should expand the dataset enough to enable machine learning while preserving the granularity of individual differences.

#### 5.4.3 Integration with HIL Optimization

The 9.98% performance improvement from ML-guided initialization may appear modest but represents a meaningful enhancement to an already-optimized system. Since the EMG-HIL framework already achieves rapid convergence, further improvements become increasingly difficult. The consistent benefit across participants, including 26.5% reduction in convergence time, demonstrates practical value for clinical deployment where session time is limited. Importantly, our approach enhances rather than replaces the adaptive capabilities of HIL optimization. The predictions provide a better starting point, but the Bayesian optimization process retains full flexibility to explore beyond the predicted quadrant if needed. This safety property ensures that incorrect predictions cannot trap the optimization in suboptimal regions, maintaining the robustness that makes HIL optimization attractive.

#### 5.4.4 Limitations and Extensions

Several limitations warrant consideration for future development. Our current approach predicts discrete parameter classes rather than continuous values, sacrificing precision for reliability given limited training data. As datasets grow through continued experiments, regression models may provide more refined initialization guidance. The focus on leg swinging also limits generalization; extending to walking or other activities requires activity-specific training data and potentially different predictive features. The reliance on anthropometric measurements, while practical, captures only structural aspects of human variation. Future work could incorporate functional assessments such as strength testing or movement screens to better predict motor control strategies. Additionally, online adaptation of the predictive models based on optimization outcomes could create a continuously improving system that learns from each new user.

### 5.5 Conclusion

This chapter demonstrated that machine learning can meaningfully enhance EMG-based HIL optimization through intelligent parameter initialization. By developing a comprehensive data processing pipeline that addresses the challenges of small anthropometric datasets, we enabled classification models that predict optimal controller parameter regions with 75% accuracy. When integrated with Bayesian optimization, these predictions yielded a 9.98% improvement in final controller performance and a 26.5% reduction in convergence time. The success of this approach validates two key principles for advancing exoskeleton control. First, the systematic relationship between user characteristics and optimal assistance parameters can be learned from

data, even with limited samples. Second, data synthesis techniques can responsibly expand small datasets to enable machine learning while preserving physiological validity. Together, these findings open pathways for more intelligent and efficient exoskeleton customization. As this thesis progresses to advanced control methods in Part II and multi-objective optimization in Part III, the ML-enhanced initialization framework provides a foundation for rapid exploration of increasingly complex parameter spaces. The ability to predict promising regions becomes even more valuable as the dimensionality of the optimization problem grows, suggesting that data-driven initialization will play an expanding role in making sophisticated exoskeleton control practical for widespread deployment.

## CHAPTER 6

# TUNING SQUATTING CONTROLLERS FOR A HIP EXOSKELETON USING EMG-BASED BAYESIAN OPTIMIZATION

### 6.1 Overview

Initialization did help but it did not yield enough benefit to keep exploring. Now the approach focuses on utilizing methods to handle load-bearing activities such as squatting. This chapter applies an EMG-based human-in-the-loop Bayesian optimization pipeline (similar to Chapter 3) to the problem of tuning hip-exoskeleton stiffness for squatting. Squatting poses distinct challenges from the free leg-swing task: larger joint excursions, greater joint power, and a stronger requirement for coordinated, phase-dependent assistance during descent and ascent. Building on the EMG-HIL and ML-initialization work developed earlier, the chapter demonstrates that continuous EMG feedback can drive fast, subject-specific adjustment of a simple variable-stiffness controller so that assistance is synchronized with natural squat kinematics and provides measurable physiological benefit.

A compact finite-state stiffness law—with separate descent and ascent gains—is tuned online using a Gaussian-process surrogate and an expected-improvement acquisition rule. EMG

---

This chapter is taken from work that was submitted to and accepted in 2025 ASME-IDETC conference, August 2025

envelopes from primary thigh muscles form the optimization cost, processed with the same filtering, epoching, and MVC normalization used throughout this thesis. In a four-subject, single-day protocol the HIL method converged rapidly (tuning completed in 4 minutes 40 seconds) and produced controllers that reduced metabolic cost by 21.3% versus no device and 22.5% versus an unpowered device. Average EMG fell by 16.6% relative to no device (and up to 21.4% versus unpowered), while perceived effort (Borg) decreased consistently with the objective improvements.

Beyond the headline numbers, the chapter makes two practical points for exoskeleton deployment. First, the EMG-driven algorithm translates to dynamic, multi-phase tasks: phase segmentation and velocity-aligned torque direction permit a simple stiffness law to yield large energetic and perceptual gains. Second, rapid within-session tuning is feasible with short trials and appropriate EMG processing, reducing participant burden relative to metabolic-cost optimization and enabling on-device personalization in clinical or field settings. Important limitations—small sample size, sensitivity to EMG placement, and the need for broader activity validation—are acknowledged; nonetheless, the results provide a strong proof of concept that the EMG-HIL paradigm generalizes beyond leg-swing and can deliver clinically relevant improvements for functional tasks such as squatting.

## 6.2 Methods

### 6.2.1 System Overview

The system provides real-time hip assistance during squatting using an EMG-based HIL optimization framework. EMG signals from the user’s leg muscles adjust the exoskeleton’s

stiffness, offering personalized support throughout the movement. The setup integrates a hip exoskeleton, EMG sensors, and a control algorithm based on Bayesian optimization. By assisting hip flexion and extension during squats, the system adapts to the user's muscle activity, reducing effort and improving efficiency. An overview of the data flow and optimization loop is shown in Figure 15.

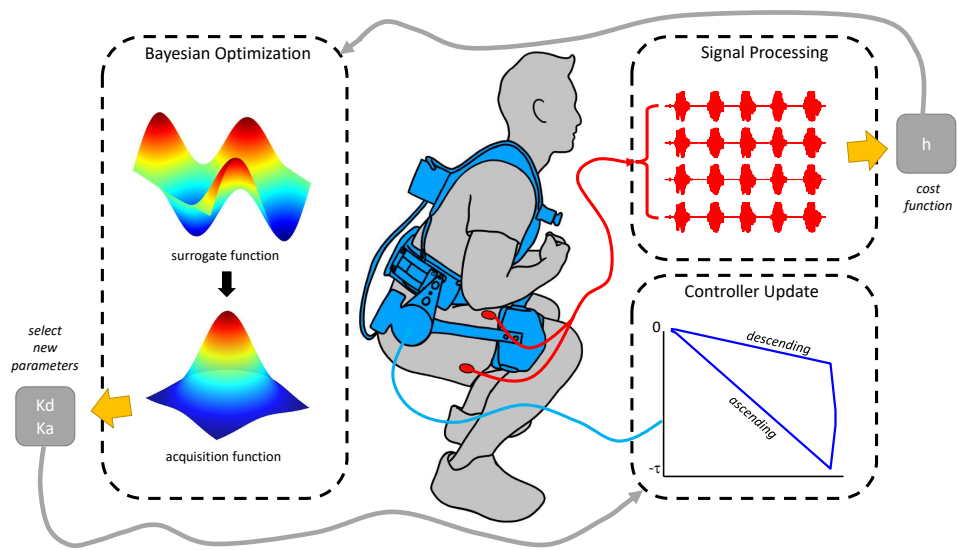


Figure 15. System data flow for EMG-based Bayesian optimization, showing acquisition, processing, and parameter tuning components.

### 6.2.2 Hip Exoskeleton Device

The exoskeleton (Figure 16) assists hip flexion and extension during squatting via variable stiffness control that adapts resistance during both descent and ascent. It features a 24V BLDC (AK70-10 T) motor delivering 25,Nm peak and 8,Nm nominal torque, and is secured with adjustable shoulder, leg, and belt straps. Minimal rigid components (plastic braces and aluminum links) allow a range of motion from (-30°) extension to (90°) flexion.

Actuation is provided by a quasi-direct drive system with an open-loop torque controller that enables back-driveability for natural movement. A built-in motor encoder, reading at 1 MHz, captures hip angles at the joint center. Safety features include hard stops, two emergency stop buttons (one for torque cut-off and one for full shutdown), and continuous torque monitoring to prevent exceeding 25 Nm.



Figure 16. Hip exoskeleton highlighting principal features, including the 24 V BLDC motor for variable stiffness control, adjustable straps for a secure fit, and rigid plastic braces. The design supports hip flexion and extension during squatting.

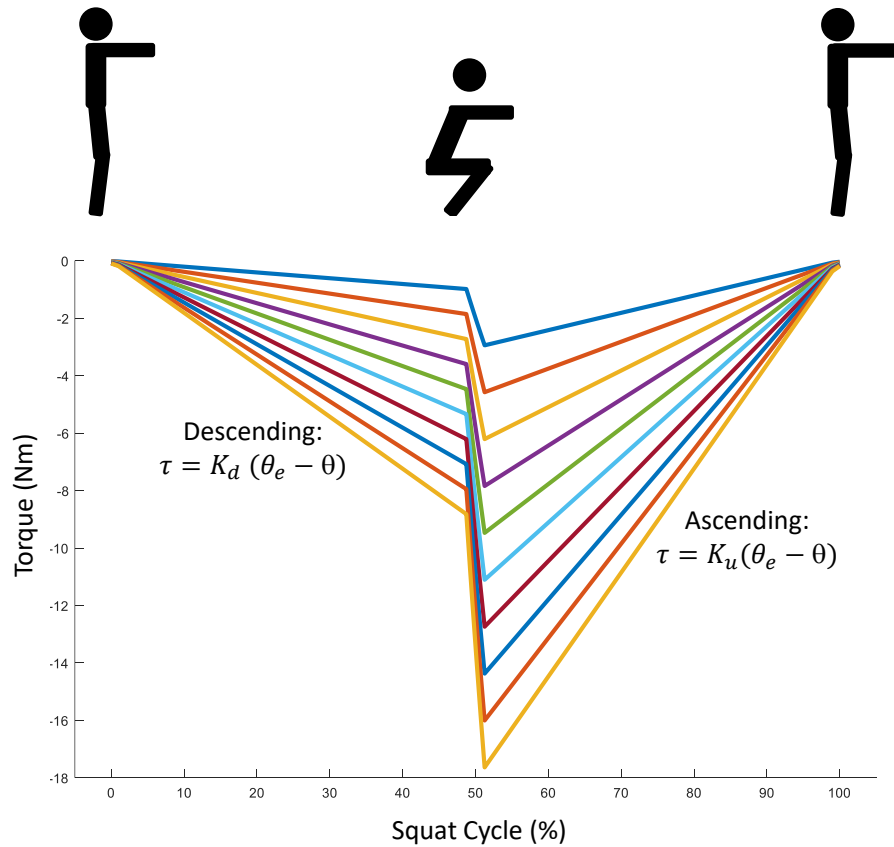


Figure 17. Schematic of the control system. A high-level finite state machine manages forward, backward, and resting states, while the low-level controller sends torque commands according to the control law.

### 6.2.3 Control Architecture

The control system operates on two levels: high-level control within Python 3.9.2 on a Raspberry Pi 4 and low-level control at the motor.

At the high level, the control system is structured around a finite state machine (FSM), chosen for its effectiveness in managing complex sequential operations and state transitions. The FSM comprises three principal states: forward leg movement, backward leg movement, and a resting state. Transitions between states are triggered by changes in angular velocity, allowing for responsive adjustments to movement patterns. To maintain natural movement dynamics, the controller aligns torque direction with velocity direction, ensuring positive work assistance. The control bandwidth is set at 350 Hz.

At the low level, high-level commands are transmitted via the CAN bus protocol to the integrated motor board, operating at 1 MHz. This quasi-direct open-loop architecture employs torque control to actuate the system. The choice of CAN bus communication ensures reliable and high-speed data transmission, crucial for real-time control.

### 6.2.4 Stiffness Control Formulation

Stiffness control regulates the exoskeleton's resistance to movement, which is crucial for providing the right support during squatting. The goal is to provide enough resistance during the descent to control the user's motion, while allowing sufficient flexibility during the ascent to aid in standing back up (Figure 17). The control law uses a linear spring model:

$$\tau = K(\theta_e - \theta) \quad (6.1)$$

where  $\tau$  is the applied torque,  $K$  the stiffness coefficient (tuned online),  $\theta_e = 0$  the equilibrium joint angle, and  $\theta$  the normalized joint angle. Distinct stiffness values are used for descending and ascending, tuned using EMG feedback.

### 6.2.5 EMG Data

EMG sensors (Trigno, Delsys) are affixed to the rectus femoris and bicep femoris of each leg. EMG data are acquired at 1778 Hz; angle orientation data are recorded at 148 Hz. Following sensor placement, maximum voluntary contraction (MVC) is measured for normalization.

Signals are processed in MATLAB: bandpass filter (20–450 Hz), outlier replacement using modified Akima cubic Hermite interpolation, rectification (absolute value and DC offset removal), and smoothing (moving maximum, discretization, moving average). Window/bin sizes are tuned to maximize SNR, after which signals are normalized by MVC. The pipeline is summarized in Figure 18. Angle data are interpolated to EMG rate and differentiated to obtain velocity, used to segment EMG into forward and backward swing datasets. These are epoched and averaged to yield eight swing representations. Cost functions for forward ( $d = f$ ) and backward ( $d = b$ ) swings are:

$$h^d = \sum_{n=1}^4 \text{rms}(M_n^d), \quad (6.2)$$

where  $M_1^d, \dots, M_4^d$  denote the four muscle EMG signals.

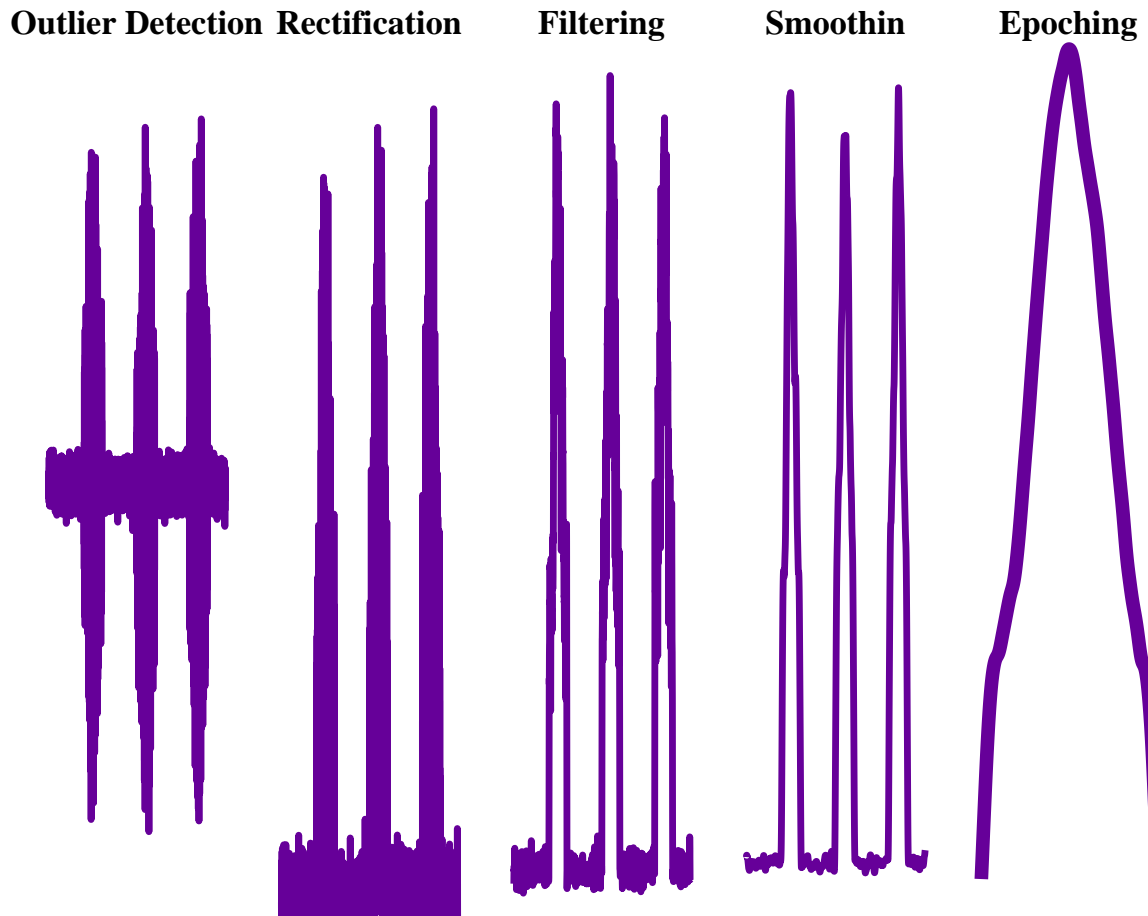


Figure 18. EMG processing workflow: filtering, rectification, smoothing, and normalization with MVC values, leading to cost functions for the forward and backward squat phases.

### 6.2.6 Bayesian Optimization

We employ Bayesian optimization to identify the optimal parameter vector  $\mathbf{x} \in \mathbb{R}^d$  that maximizes an unknown objective  $f : \mathbb{R}^d \rightarrow \mathbb{R}$ , with a Gaussian process (GP) surrogate model. Let the GP have mean  $m(\mathbf{x}) \equiv 0$  and kernel  $k(\mathbf{x}, \mathbf{x}')$ . Given inputs  $\mathbf{X} = [\mathbf{x}_1, \dots, \mathbf{x}_n]^\top$  and observations  $\mathbf{f} = [f(\mathbf{x}_1), \dots, f(\mathbf{x}_n)]^\top$ ,

$$p(\mathbf{f} \mid \mathbf{X}) = \mathcal{N}(\mathbf{f} \mid \mathbf{0}, \mathbf{K}), \quad (6.3)$$

with  $K_{ij} = k(\mathbf{x}_i, \mathbf{x}_j)$ . For test points  $\mathbf{X}_* = [\mathbf{x}_1^*, \dots, \mathbf{x}_{n_*}^*]^\top$ ,

$$\begin{pmatrix} \mathbf{f} \\ \mathbf{f}_* \end{pmatrix} \sim \mathcal{N}\left(\mathbf{0}, \begin{pmatrix} \mathbf{K} & \mathbf{K}_* \\ \mathbf{K}_*^\top & \mathbf{K}_{**} \end{pmatrix}\right). \quad (6.4)$$

Conditioning yields

$$p(\mathbf{f}_* \mid \mathbf{X}_*, \mathbf{X}, \mathbf{f}) = \mathcal{N}(\mathbf{f}_* \mid \boldsymbol{\mu}_*, \boldsymbol{\Sigma}_*), \quad (6.5)$$

$$\boldsymbol{\mu}_* = \mathbf{K}_*^\top \mathbf{K}^{-1} \mathbf{f}, \quad (6.6)$$

$$\boldsymbol{\Sigma}_* = \mathbf{K}_{**} - \mathbf{K}_*^\top \mathbf{K}^{-1} \mathbf{K}_*. \quad (6.7)$$

We use the ARD Matérn 5/2 kernel

$$k(\mathbf{x}, \mathbf{x}') = \sigma_f^2 \left(1 + \sqrt{5} r + \frac{5}{3} r^2\right) \exp(-\sqrt{5} r), \quad (6.8)$$

with

$$r = \sqrt{\sum_{i=1}^d \frac{(x_i - x'_i)^2}{\ell_i^2}}. \quad (6.9)$$

The next evaluation maximizes Expected Improvement (EI). Let  $f_{\text{best}} = \max_i f(\mathbf{x}_i)$  and  $\xi \geq 0$ :

$$\text{EI}(\mathbf{x}) = (\mu(\mathbf{x}) - f_{\text{best}} - \xi) \Phi(Z) + \sigma(\mathbf{x}) \phi(Z), \quad (6.10)$$

$$Z = \frac{\mu(\mathbf{x}) - f_{\text{best}} - \xi}{\sigma(\mathbf{x})}, \quad \mathbf{x}_{n+1} = \arg \max_{\mathbf{x} \in \mathcal{X}} \text{EI}(\mathbf{x}). \quad (6.11)$$

### 6.2.7 Experimental Protocol

The study was approved by the University of Illinois at Chicago Institutional Review Board (STUDY 1022-2022). A one-day protocol was conducted with four healthy participants. Subjects performed squats under three conditions: no exoskeleton, unpowered exoskeleton, and powered exoskeleton. The protocol comprised acclimation, tuning (EMG-based HIL stiffness optimization), and validation using optimal parameters. Metabolic cost was measured for 2 minutes per condition using a COSMED K5 and estimated via instantaneous cost mapping. A summary appears in Table V.

TABLE V

<u>EXPERIMENTAL PROTOCOL SUMMARY</u>				
<b>Phase</b>	<b>Segment</b>	<b>Cond./Trials</b>	<b>Duration</b>	<b>Rest</b>
Acclimation	No Device Activity	3 Conditions	20s	45s
	Unpowered Device	3 Conditions	20s	45s
	Powered Device	3–6 Cond.	20s	45s
Tuning	Initialization	4 Trials	20s	45s
	Tuning	10 Trials	20s	45s
Validation	No Device	1 Condition	2 min	5 min
	Unpowered Device	1 Condition	2 min	5 min
	Optimal Assistance	1 Condition	2 min	5 min

### 6.3 Results

We evaluate the impact of EMG-based HIL optimization on metabolic cost during squatting. The optimized exoskeleton reduces metabolic cost by 21.3% compared to no device and by 22.5% compared to an unpowered exoskeleton (Figure 19). These improvements underscore the benefits of real-time controller tuning on energy efficiency and user performance.

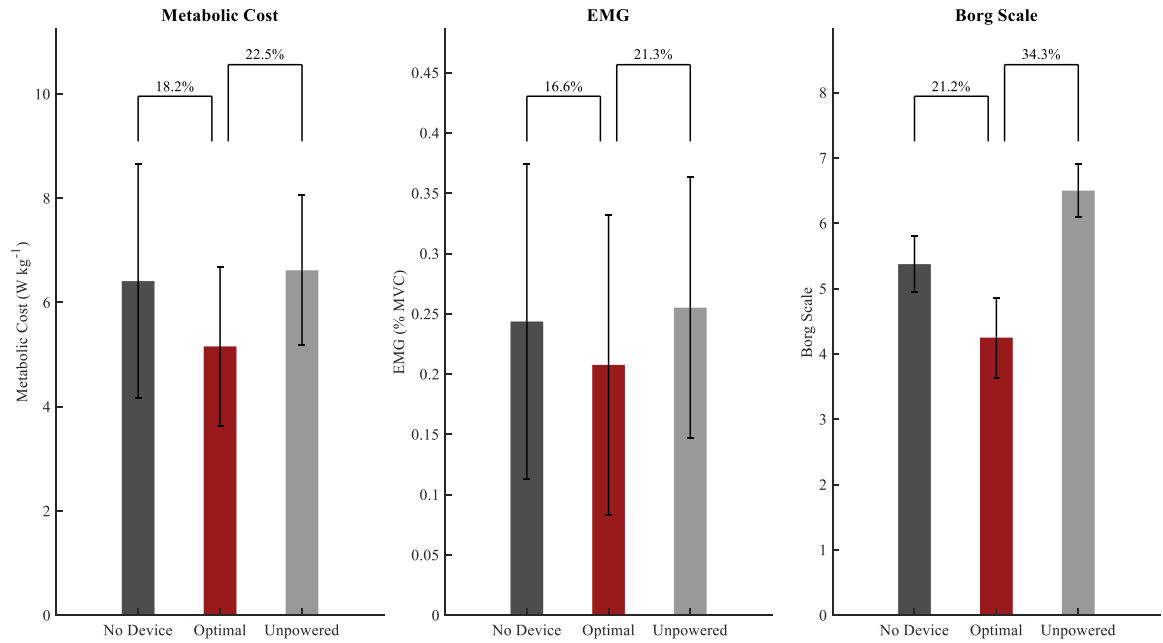


Figure 19. Performance metrics (metabolic cost, muscle EMG activity, and Borg ratings)

across no exoskeleton, unpowered exoskeleton, and optimized controller conditions. Percentage reductions with the optimized controller are shown; error bars indicate standard deviations.

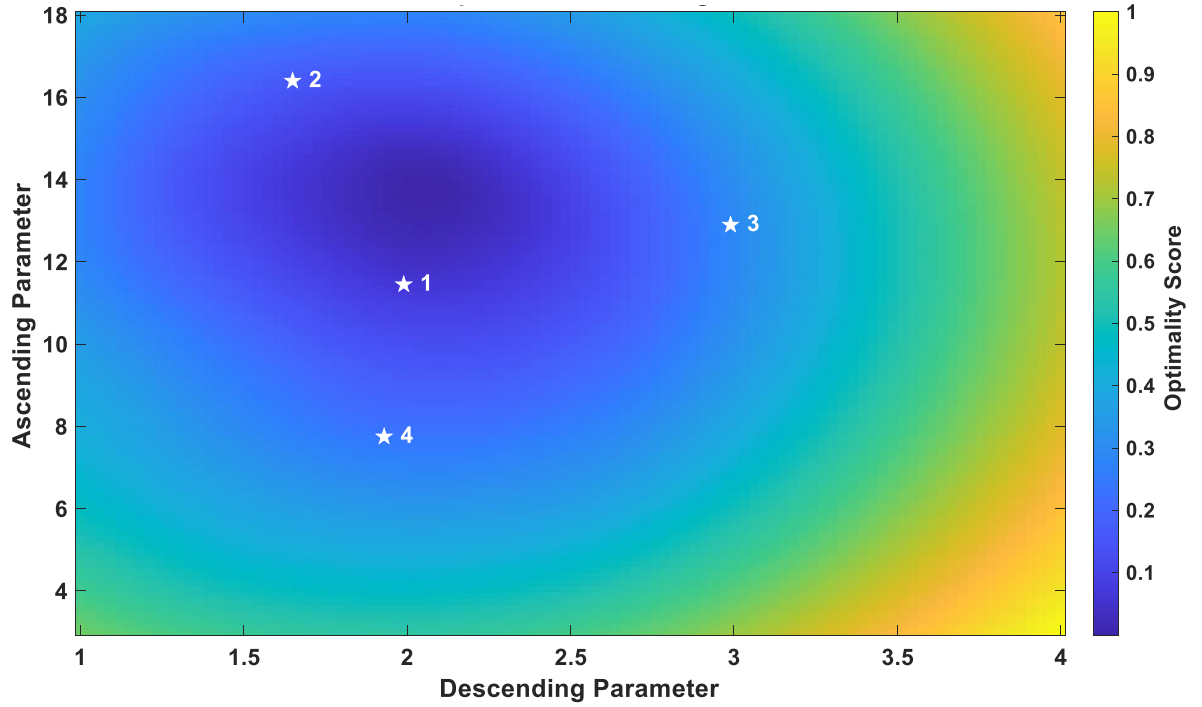


Figure 20. Heat map of control parameter combinations versus cost across all subjects. Stars mark parameter sets that achieved the minimum cost during Bayesian optimization.

Figure 20 shows the parameter-cost landscape across subjects, with stars marking optimal settings and confirming convergence to efficient regions.

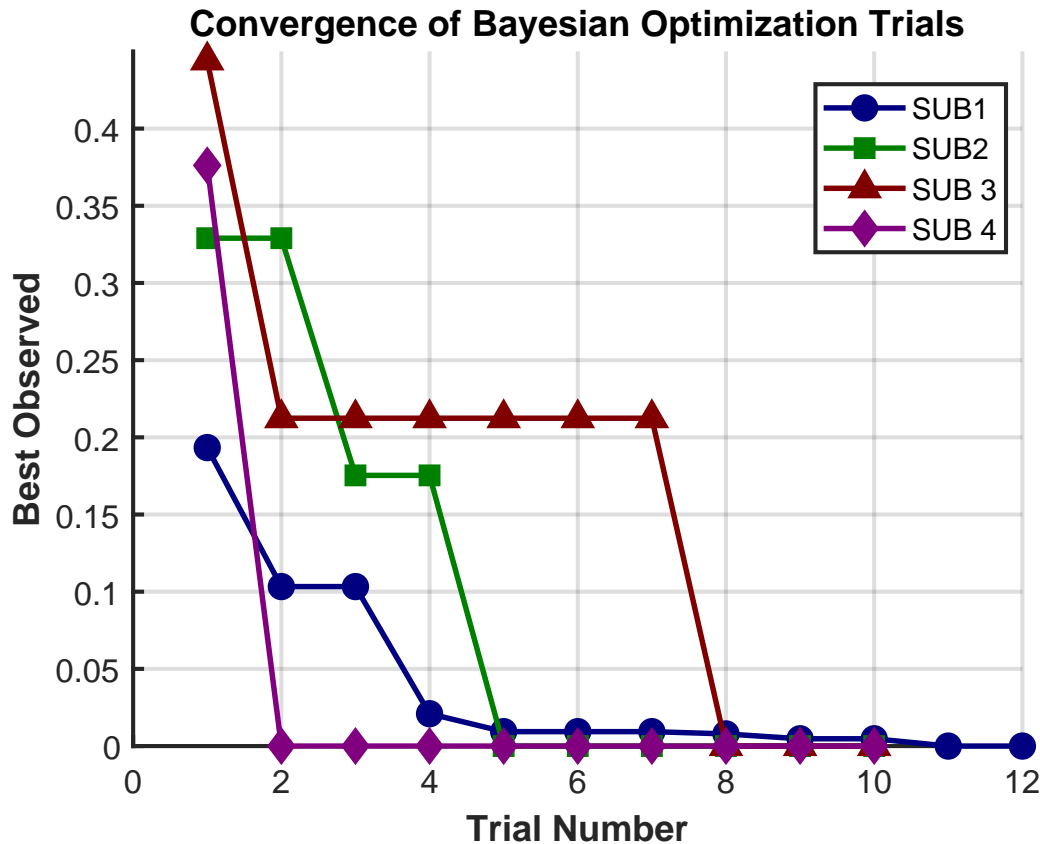


Figure 21. Convergence plots of normalized best cost by trial for each subject, demonstrating rapid convergence of the optimization algorithm.

Figure 21 depicts rapid convergence of the Bayesian optimization as the best normalized cost decreases over trials.

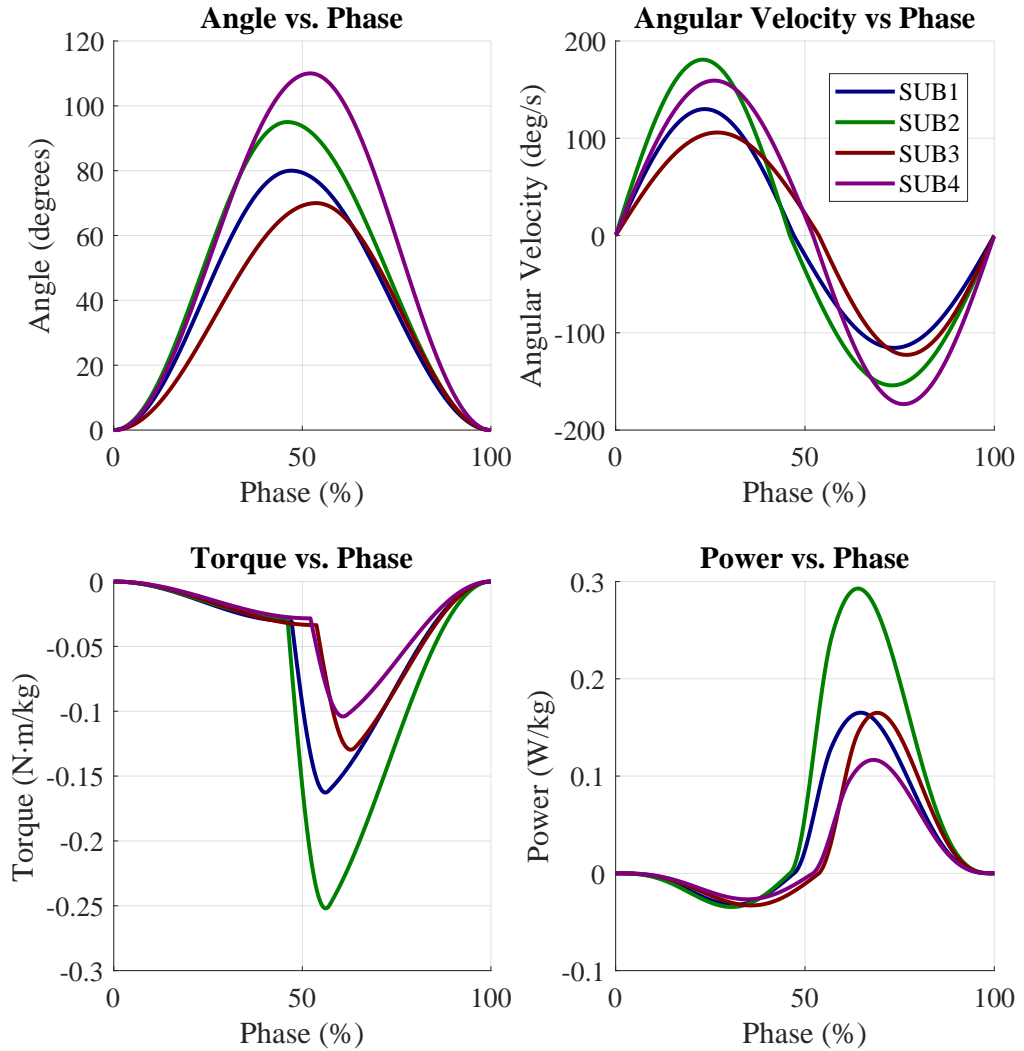


Figure 22. Kinematic profiles during squatting: (a) joint angle vs. normalized phase, (b) angular velocity vs. phase, (c) control torque vs. phase, and (d) power vs. phase, showing assistance synchronized with movement.

Subjective perceived effort (Borg scale) decreases with the optimized controller (average 4.25) compared to unpowered (6.5) and no device (5.36). Average EMG activity across four muscles decreases by 16.6% relative to no device and by 21.4% relative to unpowered.

#### 6.4 Discussion

This study demonstrates that EMG-based HIL optimization improves exoskeleton stiffness control during squatting. The optimized controller achieves significant metabolic cost reductions (21.3% relative to no device and 22.5% relative to an unpowered exoskeleton) while completing the tuning process in just 4 minutes and 40 seconds. This efficiency makes the method a strong alternative to conventional metabolic cost based tuning approaches.

In addition to metabolic improvements, the controller tuning also decreases EMG activity (by 16.6% compared to no device and 21.4% compared to the unpowered condition) and lowers perceived effort (with an average rating of 4.25 compared to higher ratings for the other conditions). These findings indicate that the optimized exoskeleton not only reduces energy expenditure but also improves muscle coordination and user comfort.

A noteworthy advantage of our approach is its rapid convergence. The EMG-based Bayesian optimization reaches optimal control parameters in a fraction of the time (4 minutes and 40 seconds) compared to the 15.8 minutes required by traditional metabolic cost based methods. This acceleration minimizes the tuning duration and reduces participant fatigue, thereby enhancing the practical applicability of the method for real time, personalized tuning.

The heat map in Figure 20 offers valuable insight into the control parameter space, while the convergence plots in Figure 21 confirm reliability and stability of the tuning process across

subjects. Kinematic profiles in Figure 22 show that assistance synchronizes with natural squat phases, enhancing movement efficiency.

Limitations include the small sample size and sensitivity to EMG sensor placement and processing choices. Future work will refine sensor calibration, incorporate additional physiological metrics, and validate on larger, more diverse cohorts.

## 6.5 Conclusion

EMG-based Bayesian optimization is a rapid and effective method for tuning exoskeleton controllers during squatting. The optimized tuning significantly reduces metabolic cost, improves user comfort, and lowers perceived effort. With the entire process completing in just 4 minutes and 40 seconds, this approach supports real-time, personalized adjustments for both rehabilitation and daily use. Future efforts will explore additional physiological signals, improved calibration, and larger-scale validation to further enhance performance and generalizability.

## CHAPTER 7

# EMG SIGNAL ENHANCEMENT VIA MULTI-OBJECTIVE OPTIMIZATION OF HANKEL-BASED BAYESIAN LEARNING

### 7.1 Overview

Squatting experiments revealed EMG noise that would be a significant challenge to walking. Before moving on to a more dynamic activity, the refinement of the EMG signal is critical. This chapter presents an automated, multi-objective framework for improving the utility of surface EMG by jointly addressing reconstruction, prediction, and smoothing. EMG signals are indispensable for neuromuscular assessment and for closed-loop control of assistive devices, but their practical value is frequently limited by measurement noise and transient artifacts that either obscure important physiological events or force aggressive smoothing that erases them. Rather than treating denoising as a single-goal signal-processing step, the framework developed here treats EMG enhancement as a trade-off between competing objectives and optimizes that trade-off directly.

Our approach builds on three complementary components. First, Hankel-embedding and low-rank SVD reconstruction recover the dominant dynamical structure in short windows of the

---

Parts of this chapter are taken from work submitted and accepted to the 2025 Modeling, Estimation and Control Conference

raw trace, exploiting temporal redundancy without imposing a rigid parametric model. Second, a Bayesian-regularized linear prediction (a Koopman-style state-transition estimate formed from time-shifted Hankel matrices) captures the signal’s immediate dynamics and provides a principled model-based complement to the reconstruction. Third, the two estimates are fused and followed by a targeted Makima–median smoothing stage that removes residual high-frequency artifacts while preserving transient features. The full pipeline is controlled by a small set of interpretable parameters (embedding dimension, SVD rank, regularization variances, fusion weight and smoother length) that determine the balance between noise suppression and feature retention.

Tuning these parameters is formulated as a multi-objective Bayesian optimization problem. Two objectives are optimized simultaneously: a noise-suppression metric (conventionally SNR-related) and a structural-fidelity metric that quantifies how well clinically relevant temporal features are preserved. By searching for Pareto-optimal parameter combinations rather than collapsing the trade-off into a single scalar, the method yields reconstructions that decouple SNR gains from fidelity losses and therefore produce more useful EMG traces for downstream analysis and control.

Validation uses an open, multimodal biomechanics dataset and focuses on muscles and tasks that are representative of rehabilitation and assistive-device applications (rectus femoris, biceps femoris, gluteus maximus, and gastrocnemius during walking and squatting). Quantitative results show large improvements in composite metrics that blend fidelity and noise reduction (the squared geometric mean) and statistically significant gains in a normalized joint-fidelity

measure; importantly, the proposed pipeline reduces the negative correlation that typically binds SNR and structural similarity in conventional denoising methods.

The chapter reflects on practical considerations and limitations. Multi-objective tuning increases computational expense and requires careful choice of objective measures to reflect application priorities; real-time deployment will require modest algorithmic simplifications or fast surrogate evaluations. The method is intentionally interpretable and modular, however, which facilitates task-specific adaptation (different smoothing or fusion strategies) and incremental integration into existing HIL and ML pipelines. The concluding sections outline concrete pathways for real-time implementation, broader muscle/task validation, and incorporation of additional physiological objectives in future work.

## 7.2 Methods

### 7.2.1 Data Acquisition

This study utilizes open-source biomechanical data [136], which provide synchronized motion capture, ground-reaction forces, surface EMG (2 kHz sampling rate, Surface Electromyography for the Non-Invasive Assessment of Muscles (SENIAM) electrode placement), and Inertial Measurement Unit (IMU) streams from 12 healthy adults performing various cyclic and acyclic activities. For this study, we select ten subjects based on EMG signal quality and focus on two activities: level-ground walking and body-weight squatting. We process EMG channels for the rectus femoris (RF), biceps femoris (BF), gluteus maximus (GM), and medial gastrocnemius (GN). Raw EMG traces undergo full-wave rectification before downstream analysis.

### 7.2.2 Hankel-based Signal Reconstruction

A noisy signal  $x(t)$  with  $N$  samples is first embedded into a Hankel matrix of dimension  $d$ :

$$\mathbf{H} = \begin{bmatrix} x(1) & x(2) & \cdots & x(N-d+1) \\ x(2) & x(3) & \cdots & x(N-d+2) \\ \vdots & \vdots & \ddots & \vdots \\ x(d) & x(d+1) & \cdots & x(N) \end{bmatrix}, \quad (7.1)$$

where  $d$  is the embedding (lag) dimension which controls how many past samples are used for reconstruction.

Singular Value Decomposition (SVD) is then applied:

$$\mathbf{H} = \mathbf{U}\Sigma\mathbf{V}^\top, \quad (7.2)$$

and a low-rank approximation is obtained by retaining the first  $r$  components:

$$\mathbf{H}_r = \mathbf{U}_r\Sigma_r\mathbf{V}_r^\top. \quad (7.3)$$

Diagonal averaging (Hankelization) converts  $\mathbf{H}_r$  back into a time-domain signal:

$$\hat{x}(k) = \frac{1}{n_k} \sum_{i+j=k+1} [\mathbf{H}_r]_{ij}, \quad k = 1, \dots, N, \quad (7.4)$$

where  $n_k$  denotes the number of elements in the  $k$ -th anti-diagonal. The output  $\hat{x}(t)$  is thus a denoised estimate of the original  $x(t)$ .

### 7.2.3 Regularized Estimation via Bayesian Linear Regression

To estimate a robust model of the signal, we employ a Bayesian linear regression framework using two time-shifted Hankel matrices constructed from the state observations:

$$\mathbf{H}_1 = \mathbf{H}(:, 1:N-1), \quad (7.5)$$

$$\mathbf{H}_2 = \mathbf{H}(:, 2:N), \quad (7.6)$$

These matrices represent sequential state pairs, where  $\mathbf{H}_1$  contains the states at time  $t$ , and  $\mathbf{H}_2$  contains the corresponding states at time  $t + 1$ . The transition matrix  $\mathbf{A}$  is estimated via ridge regression:

$$\mathbf{A} = \left( \mathbf{H}_1^\top \mathbf{H}_1 + \lambda \mathbf{I} \right)^{-1} \mathbf{H}_1^\top \mathbf{H}_2, \quad (7.7)$$

### 7.2.4 Signal Fusion

Having obtained both a reconstructed signal  $\hat{x}(t)$  and a predicted signal  $\hat{x}_{\text{pred}}(t)$ , we fuse these estimates to exploit their complementary strengths. The fusion combines the reconstruction accuracy of  $\hat{x}(t)$  with the dynamical consistency of  $\hat{x}_{\text{pred}}(t)$ :

$$\hat{x}_{\text{final}}(t) = w \hat{x}(t) + (1 - w) \hat{x}_{\text{pred}}(t),$$

where  $w \in [0, 1]$  adjusts the balance between the two. We tune five key parameters to optimize performance:

$$\theta = \{d, r, \sigma^2, \tau^2, w\},$$

where  $d$  is the embedding dimension,  $r$  the SVD rank,  $\sigma^2$  and  $\tau^2$  are regularization variances, and  $w$  the fusion weight.

### 7.2.5 Multi-objective Bayesian Optimization

To identify the best parameter set  $\theta$ , we apply Bayesian optimization with two objectives.

### 7.2.6 Windowed Makima Median Smoother

To further target any high-frequency noise artifacts and improve signal continuity, we apply a post-estimation smoothing stage.

## 7.3 Results

The proposed method exhibits an average improved fidelity retention of .571 relative to the control method, while the raw SNR metric actually shows a decrease of 6 dB. Despite the SNR decrease, these values translate into a combined SGM improvement of 108.7% ( $p = 0.0282$ ) and a normalized joint metric gain of 11.4% ( $p = 0.0011$ ), indicating superior performance to traditional methods by successfully mitigating the trade-off between noise suppression and preservation of critical signal features. Figure 25 shows the comparison of the two metrics between the control group and the experimental group.

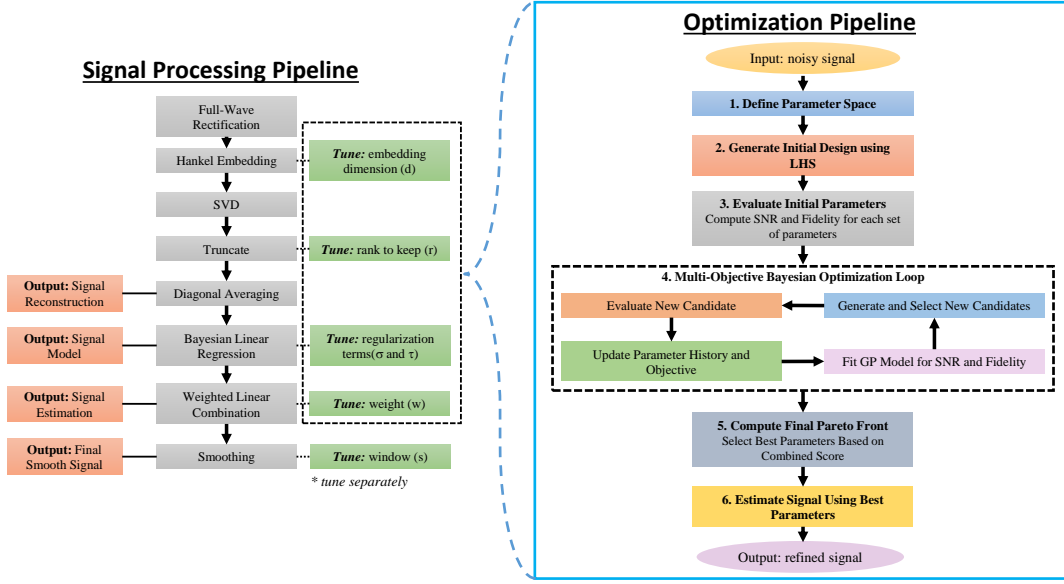


Figure 23. Schematic of the EMG enhancement and optimization workflow. Raw EMG is denoised via an optimized process involving Hankel-SVD, prediction by a Bayesian Koopman model, weighted combination, and smoothing. The asterisk (\*) indicates that the five parameters ( $d$ ,  $r$ ,  $\sigma$ ,  $\tau$ ,  $w$ ) are optimized via multi-objective Bayesian optimization, while the smoother window length ( $s$ ) is optimized independently.

## 7.4 Discussion

The results demonstrate that our multi-objective optimization framework strikes a superior balance between noise suppression and signal fidelity. Although the raw SNR decreases by 6dB relative to the control method, fidelity retention improves markedly by 0.571. When these two effects combine into the SGM, we observe a 108.7% gain ( $p=0.0282$ ), and the normalized joint metric increases by 11.4% ( $p=0.0011$ ). These outcomes confirm that optimizing multiple objectives yields more clinically meaningful reconstructions than single-objective tuning.

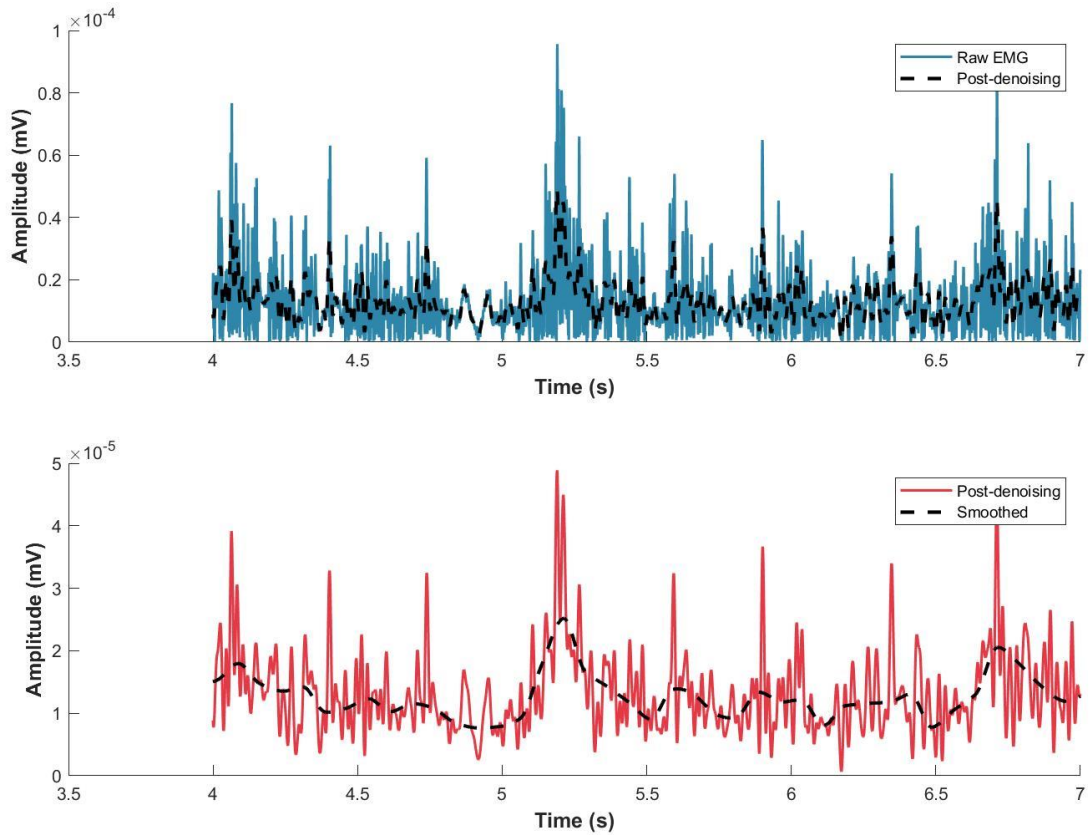


Figure 24. Processing stages for one EMG channel. Top: raw signal to fused output (dashed). Bottom: fused output to Makima-median smoothing. Note that the fused output retains physiological features while reducing noise, and the final smoothing removes residual high-frequency artifacts.

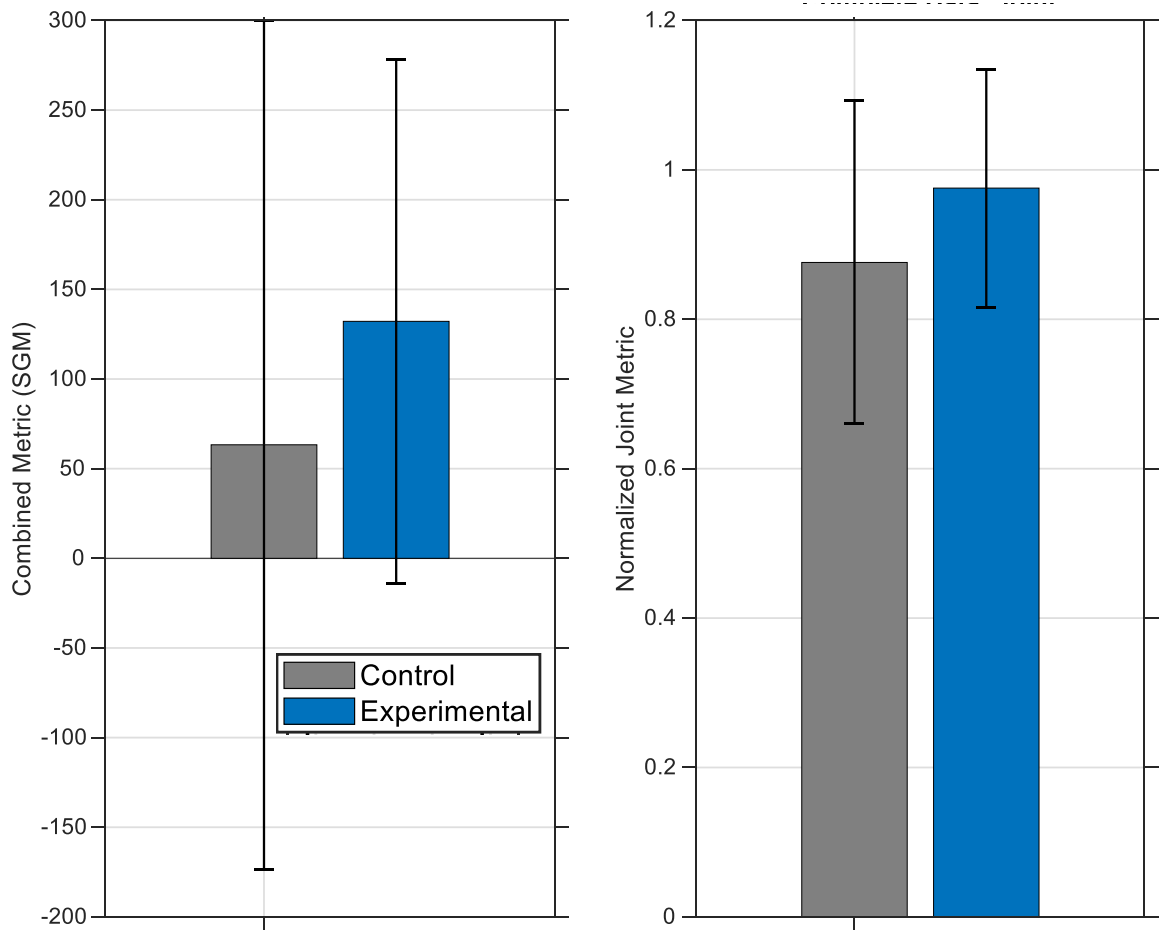


Figure 25. Mean and standard deviation comparison of control (gray) and experimental (blue) on SGM (left) and normalized joint metric (right) across all subjects and activities. Control refers to the standard EMG processing pipeline, while Experimental refers to our proposed Hankel-Bayesian optimization framework.

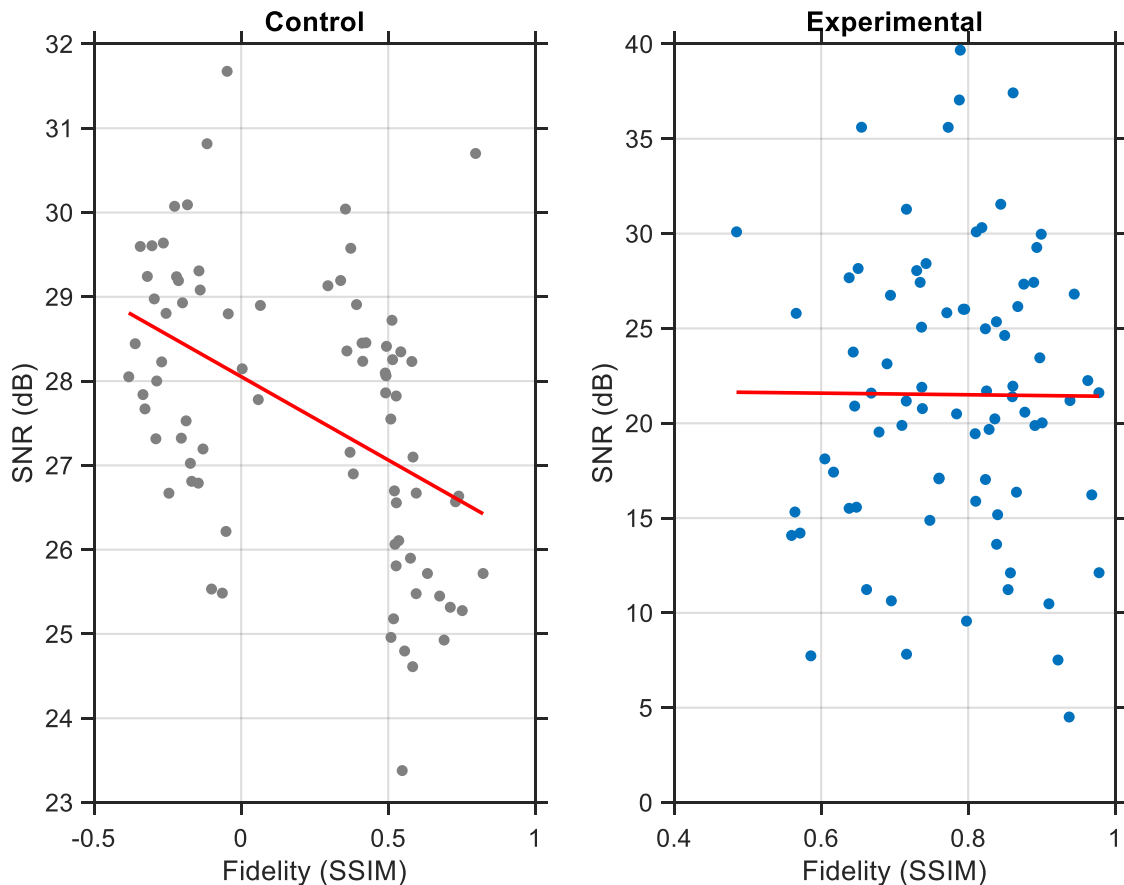


Figure 26. Scatter of SNR vs. SSIM for control (gray) and our method (blue). Dashed red lines are linear fits showing strong negative correlation in control ( $r=-0.64$ ) versus near zero in our pipeline ( $r=0.01$ ).

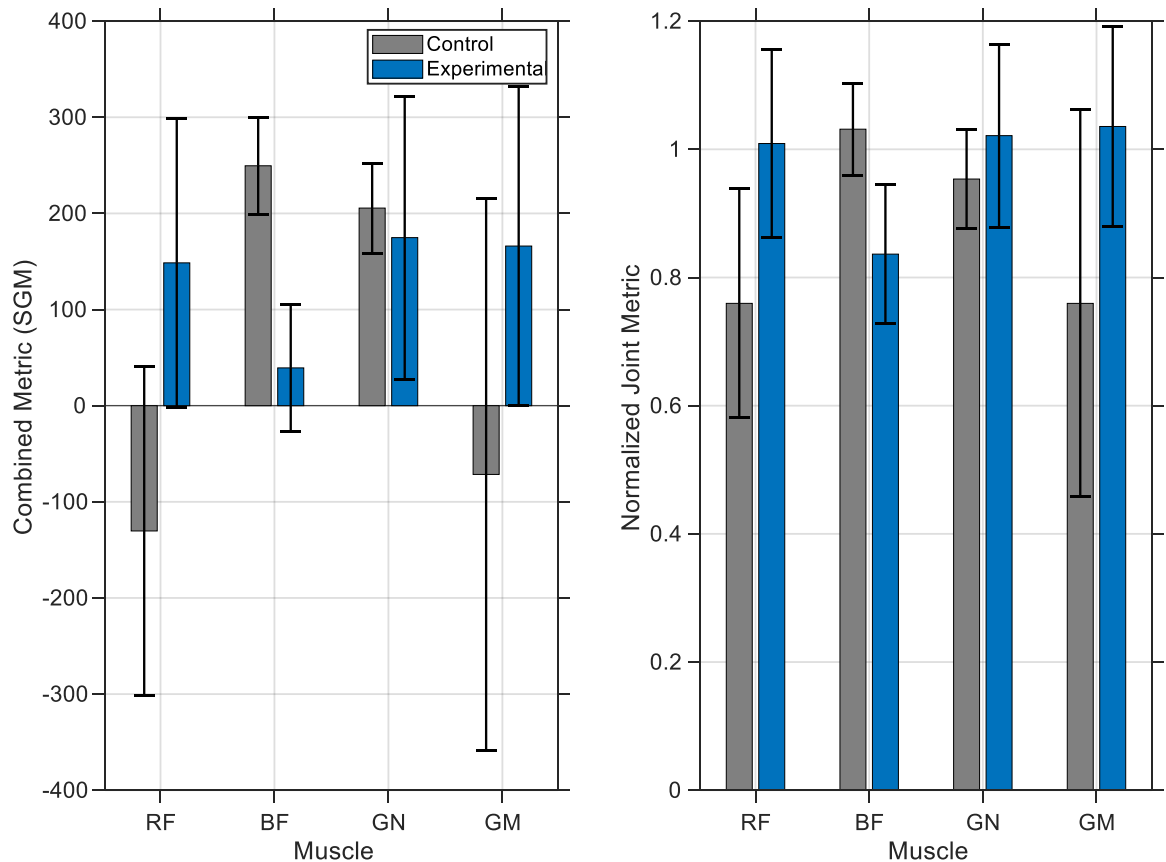


Figure 27. Muscle-specific mean $\pm$ standard deviation for control (gray) and experimental (blue) on SGM (left) and joint metric (right) for RF: rectus femoris, BF: biceps femoris, GN: gastrocnemius, and GM: gluteus maximus.

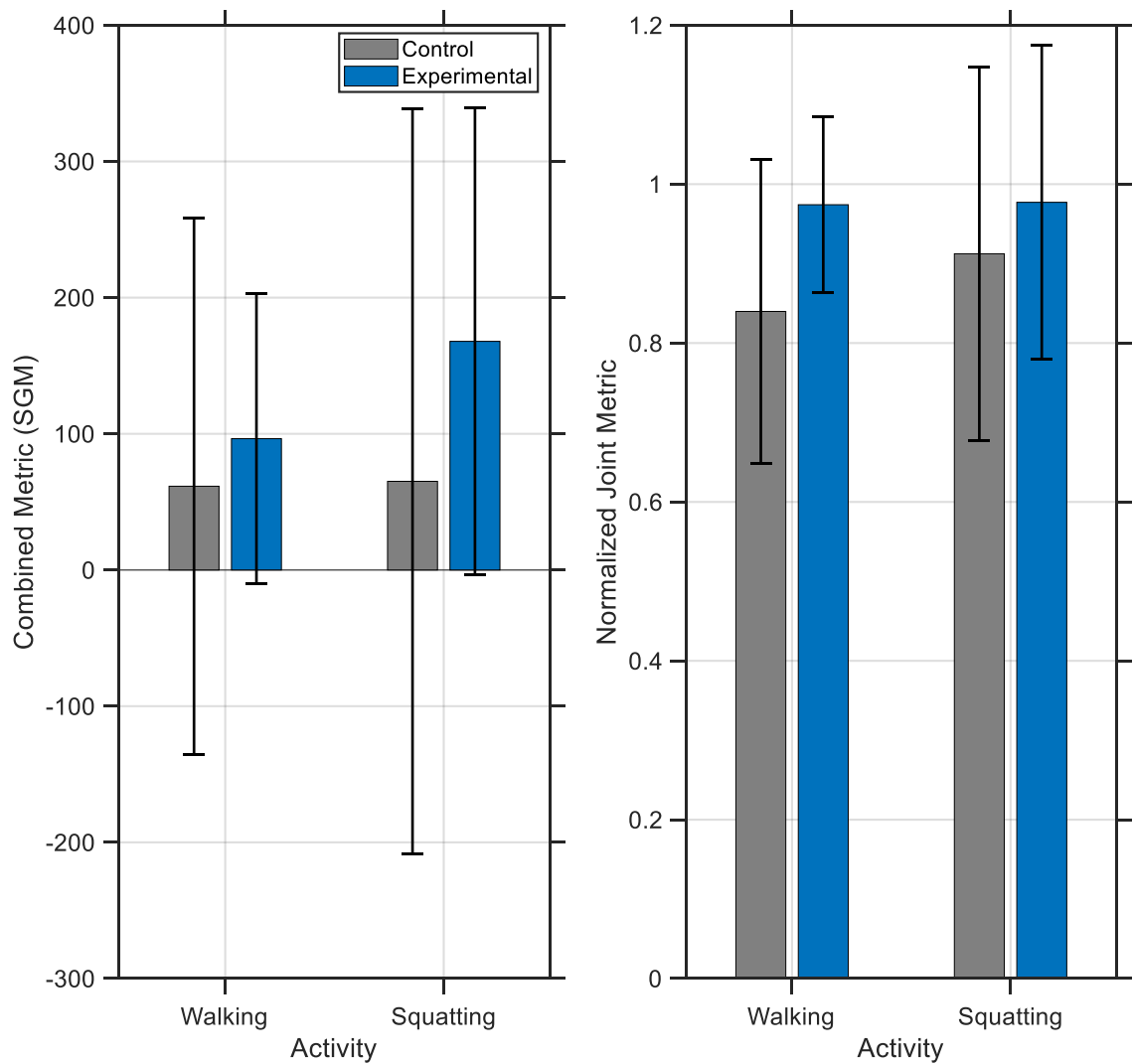


Figure 28. Activity-specific mean and standard deviation for walking and squatting, comparing control and experimental methods on SGM (left) and joint metric (right).

## 7.5 Conclusions

We introduce an automated EMG denoising framework coupling Hankel decomposition, Bayesian-regularized Koopman regression, Makima smoothing, and EHVI-driven Gaussian-Process multi-objective optimization. It achieves 108.7% SGM and 11.4% joint-metric gains ( $p < 0.05$ ), decoupled SNR-fidelity ( $r \approx 0$ ), and task-/muscle-specific enhancements. This interpretable approach supports future real-time clinical and assistive-device applications.

## CHAPTER 8

# ADAPTIVE WALKING CONTROLLERS: A COMPREHENSIVE SIMULATION STUDY OF IMPEDANCE-BASED ASSISTIVE STRATEGIES

### 8.1 Overview

With denoised signals, it is now crucial to focus on what controller best serves walking assistance. This is done by systematically studying controller families in a data-validated simulation. The following chapter integrates a study of adaptive impedance controllers for walking assistance into the thesis framework. Several controller families are compared under a common optimization and evaluation protocol: direction-dependent gains, energy-modulated impedance, a compact phase-adaptive law, and smoothly varying stiffness profiles parameterized with Bézier curves. Controller parameters are tuned with Bayesian optimization against experimental gait data, and performance is assessed using a mechanical power proxy, time-averaged  $|\tau\dot{\theta}|$ , and a torque smoothness metric defined as the inverse mean absolute second derivative of torque.

Results show a clear trade-off between energetic benefit and actuator-friendly smoothness. Bézier Variable Stiffness Control (BVSC) attains the largest reduction in the mechanical proxy (up to 62.9%), while a compact phase-adaptive controller realizes most of that benefit ( $\sim 55.5\%$ )

---

This chapter is taken from unpublished precursor work for a publication.

with far fewer parameters; BVSC and the phase-adaptive law differ meaningfully in smoothness ( $S_{BVSC} = 0.91 \text{ s}^2/\text{Nm}$  vs.  $S_{\text{phase}} = 0.75 \text{ s}^2/\text{Nm}$ ). Pareto analysis highlights that no single architecture dominates both objectives, and that phase- and velocity-aware modulation captures much of the energetic advantage of richer stiffness shaping at substantially lower implementation cost.

Within the dissertation, this chapter supplies system-level insight that complements the EMG-driven and HIL-focused work that follows. The simulations identify controller structures and parameterizations that are likely to produce large energetic gains, and they clarify the smoothness costs associated with highly expressive stiffness profiles. These observations inform the choice of compact, phase-aware families as practical starting points for rapid EMG-based tuning and for ML-guided initialization in subsequent chapters. The main limitation is that the findings are simulation-based; experimental validation on hardware and with physiological outcomes (e.g., metabolic cost) is required to confirm transfer to users.

## 8.2 Methods

### 8.2.0.1 Experimental Data

We used joint kinematics and torque trajectories from an open-source biomechanics dataset capturing lower-limb motion across level-ground walking, ramps, and stairs [137]. For this study, treadmill walking trials from healthy adults at self-selected speeds were extracted. The dataset provides synchronized motion capture and ground reaction force data sampled at 100 Hz, from which joint torques were computed via inverse dynamics (Figure 29). Representative trajectories

were obtained by time-normalizing and averaging across multiple gait cycles, resulting in stride-aligned profiles of joint angles and biological torques for controller design and evaluation.

### 8.2.1 Normalize Angles and Velocities

Prior to controller development, raw data underwent several preprocessing steps to facilitate controller design and ensure numerical stability.

#### 8.2.1.1 Angle Normalization

Joint angles  $\theta$  were normalized to the range  $[0, 1]$  using min-max scaling:

$$\theta_{\text{norm}} = \frac{\theta - \theta_{\min}}{\theta_{\max} - \theta_{\min}} \quad (8.1)$$

This normalization enables controller designs that are invariant to the absolute angle range while preserving the relative motion patterns.

#### 8.2.1.2 Velocity Computation and Normalization

Angular velocity was computed using numerical differentiation:

$$\dot{\theta} = \frac{d\theta}{dt} \approx \frac{\theta[n+1] - \theta[n-1]}{2\Delta t} \quad (8.2)$$

where  $\Delta t = 0.01$  s. The velocity was subsequently normalized to  $[-1, 1]$ :

$$\dot{\theta}_{\text{norm}} = 2 \frac{\dot{\theta} - \dot{\theta}_{\min}}{\dot{\theta}_{\max} - \dot{\theta}_{\min}} - 1 \quad (8.3)$$

### 8.2.1.3 Energy Metric Calculation

For energy-based controllers, we computed a mechanical energy metric combining kinetic and potential energy terms:

$$E = \dot{\theta}^2 + (1 - \cos(\theta)) \quad (8.4)$$

This metric was normalized to [0, 1] using the same min-max scaling approach. The formulation captures both velocity-dependent kinetic energy and configuration-dependent potential energy.

## 8.2.2 Define Controller Architectures

We developed and evaluated the following controller architectures, each implementing variations of impedance control with increasing complexity and adaptability. The formulations below reflect only the controllers that were implemented and tested.

### 8.2.2.1 Basic Per-Direction Controller

The simplest adaptive strategy employs separate impedance parameters for forward and backward motion phases:

$$\tau = \begin{cases} K_f(\theta_d - \theta_{\text{norm}}) + B_f(0 - \dot{\theta}_{\text{norm}}) & \text{if } \dot{\theta}_{\text{norm}} \geq 0 \\ K_b(\theta_d - \theta_{\text{norm}}) + B_b(0 - \dot{\theta}_{\text{norm}}) & \text{if } \dot{\theta}_{\text{norm}} < 0 \end{cases} \quad (8.5)$$

2 variants were implemented for determining the desired angle  $\theta_d$  (as defined in the basic controller formulation):

1. Contralateral reference:  $\theta_d = \theta_{\text{opposite}}(t - 0.5T)$

2. Phase-shifted current angle:  $\theta_d = \theta_{\text{norm}}(t + \phi T)$

where  $T$  is the gait cycle period and  $\phi \in [-1, 0]$  is an optimizable phase parameter.

### 8.2.2.2 Normalized Gain Controller

To reduce the parameter search space while maintaining physiological relevance, we introduced normalized parameters  $w, p \in [0, 1]$ :

$$K = (3 + 12w) \cdot p \quad (8.6)$$

$$B = 5w \cdot (1 - p) \quad (8.7)$$

This formulation ensures  $K \in [3, 15]$  and  $B \in [0, 5]$ , ranges determined from literature on human joint impedance [62, 138]. Separate  $(w, p)$  pairs were optimized for forward and backward phases.

### 8.2.2.3 Energy-Based Adaptive Controller

Inspired by biological energy storage and release mechanisms, this controller modulates impedance based on the normalized energy metric:

$$K = \alpha \cdot E_{\text{norm}} \quad (8.8)$$

$$B = \beta \cdot E_{\text{norm}} \quad (8.9)$$

where  $\alpha$  and  $\beta$  are optimizable gain parameters. This approach naturally increases impedance during high-energy states (fast motion, extreme positions) and reduces it during low-energy states.

#### 8.2.2.4 Phase-Based Adaptive Controller

This controller introduces dynamic impedance modulation based on 2 key metrics:

1. Phase completion percentage:  $p = 1 - |\theta_d - \theta_{\text{norm}}|$ , where  $\theta_d$  is the desired angle defined in Section 3.3.1
2. Normalized velocity magnitude:  $s = |\dot{\theta}_{\text{norm}}|$

The impedance parameters are then computed as:

$$K = \alpha \cdot p \cdot (1 - s) \quad (8.10)$$

$$B = \alpha \cdot p \cdot s \quad (8.11)$$

This formulation provides high stiffness when approaching the target position with low velocity and high damping when moving rapidly, automatically balancing position tracking and velocity regulation.

#### 8.2.2.5 Variable Stiffness Controllers

2 advanced formulations enable smooth, continuous stiffness modulation throughout the gait cycle.

**Bump Sine Controller:** Stiffness follows a smooth bump-shaped profile:

$$K(\theta_{\text{norm}}) = \begin{cases} L \sin\left(\frac{\pi}{2} \cdot \frac{\theta_{\text{norm}}}{P}\right) & \text{if } \theta_{\text{norm}} \leq P \\ L \sin\left(\frac{\pi}{2} \cdot \frac{1-\theta_{\text{norm}}}{1-P}\right) & \text{if } \theta_{\text{norm}} > P \end{cases} \quad (8.12)$$

where  $L$  is the peak stiffness and  $P \in [0.05, 0.95]$  is the peak location.

**Bézier Curve Controller:** For maximum flexibility, we implemented composite Bézier curves with 8 control points:

$$\mathbf{B}(t) = \sum_{i=0}^3 \binom{3}{i} (1-t)^{3-i} t^i \mathbf{P}_i \quad (8.13)$$

2 cubic Bézier segments, each spanning half the gait cycle, were joined at a parametric midpoint with  $C^1$  continuity enforced. Separate curves were optimized for forward and backward motion. The control points were parameterized by magnitude ( $M$ ) and location ( $L$ ) parameters to maintain smooth profiles while reducing optimization complexity.

### 8.2.3 Optimize Controller Parameters

#### 8.2.3.1 Cost Function

The primary optimization objective minimized the root mean square (RMS) of net torque:

$$J = \sqrt{\frac{1}{N} \sum_{i=1}^N (\tau_{\text{bio}}[i] - \tau_{\text{controller}}[i])^2} \quad (8.14)$$

This objective increases controller torque contribution to the net joint torque proxy by minimizing RMS deviation from biological torque.

### 8.2.3.2 Bayesian Optimization

Parameter optimization employed Bayesian optimization with Gaussian process priors [139] and expected improvement (EI) acquisition function:

$$\text{EI}(x) = \mathbb{E}[\max(f_{\min} - f(x) - \xi, 0)] \quad (8.15)$$

where  $f_{\min}$  is the current best observation and  $\xi$  is an exploration parameter. This approach efficiently explores the parameter space while balancing exploration and exploitation.

Optimization settings:

- Maximum iterations: 30 to 50 (controller-dependent)
- Initial sampling: Latin hypercube design (5 points)
- Kernel: Matérn 5/2 with automatic relevance determination [140]
- Acquisition function optimizer: L-BFGS-B

### 8.2.4 Evaluate Assistance Metrics

#### 8.2.4.1 Mechanical Power Proxy Reduction

The primary performance metric quantified the reduction in mechanical power proxy:

$$\eta = \frac{P_{\text{bio}} - P_{\text{net}}}{P_{\text{bio}}} \times 100\% \quad (8.16)$$

where:

$$P_{\text{bio}} = \frac{1}{T} \int_0^T |\tau_{\text{bio}} \cdot \dot{\theta}| dt \quad (8.17)$$

$$P_{\text{net}} = \frac{1}{T} \int_0^T |(\tau_{\text{bio}} - \tau_{\text{controller}}) \cdot \dot{\theta}| dt \quad (8.18)$$

Here  $\dot{\theta}$  is in rad/s; the proxy has units of W and serves as a surrogate for metabolic cost.

Mechanical power proxies in simulation are standard practice [19, 141].

#### 8.2.4.2 Torque Smoothness

We define torque *roughness* as the mean absolute second derivative of torque:

$$R = \frac{1}{N-2} \sum_{i=2}^{N-1} \left| \frac{\tau[i+1] - 2\tau[i] + \tau[i-1]}{\Delta t^2} \right| \quad (8.19)$$

and report *smoothness* as its inverse,

$$S = \frac{1}{R}, \quad (8.20)$$

so higher  $S$  indicates smoother torque profiles (units:  $s^2/Nm$ ), which benefits actuator longevity and user comfort [142].

### 8.3 Results

#### 8.3.1 Controller Performance (Tested Only)

BVSC achieved the largest mechanical power proxy reduction (62.9%) with smoothness  $S = 0.91 s^2/Nm$ . The next-best controller, Normalized Gain (phase-current), reached 56.4% proxy reduction with  $S = 3.16 s^2/Nm$ . Across all controllers, reductions spanned 43.5% to

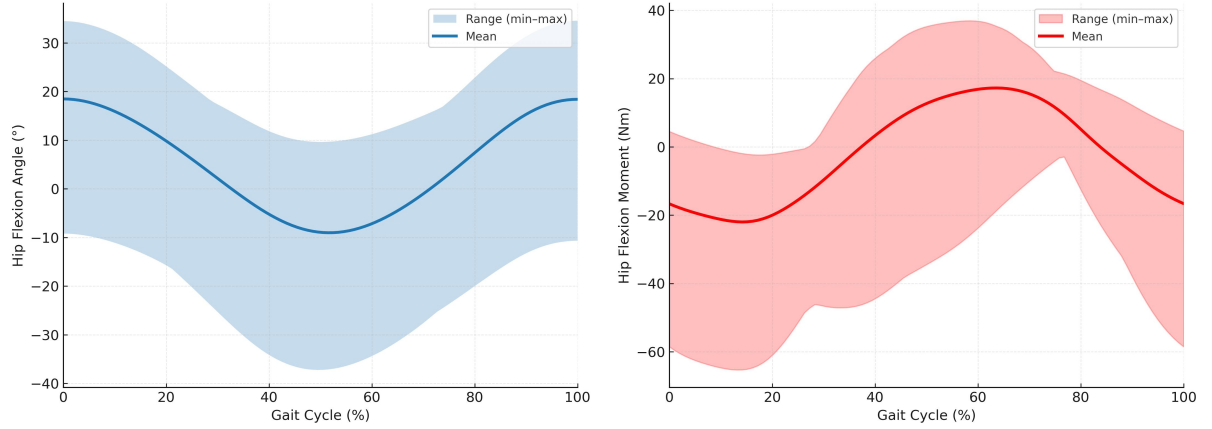


Figure 29. Reference gait profiles used for controller design and evaluation. Left: mean hip flexion angle with a shaded min–max range across all cycles. Right (red): mean hip flexion moment with a shaded min–max range. The horizontal axis is the normalized gait cycle (0–100%), and vertical axes are angle ( $^{\circ}$ ) and moment (Nm), respectively. These summaries provide a compact baseline against which controller torques are compared, while the range bands visualize inter-cycle variability.

62.9%. The phase-based adaptive controller demonstrated particularly favorable performance, achieving 55.5% proxy reduction with *lower* smoothness ( $S = 0.75 \text{ s}^2/\text{Nm}$ ) than BVSC (0.91  $\text{s}^2/\text{Nm}$ ), despite substantially fewer parameters.

Analysis of the torque profiles in Figure 31 reveals distinct control strategies. BVSC generates smoothly varying torque that closely tracks the biological reference throughout the cycle, which aligns with its higher smoothness value. The phase-based controller produces more selective assistance, applying torque primarily during high-power phases while maintaining low output during transitions, consistent with its lower  $S$ . The Normalized Gain controller shows intermediate behavior, with moderate torque throughout the cycle.

TABLE VI

## CONTROLLER PERFORMANCE COMPARISON

Controller	Power Proxy Reduction (%)	Smoothness $S$ ( $\text{s}^2 \text{N}^{-1} \text{m}$ )
Variable Stiffness (Bézier)	62.9	0.91
Normalized Gain (phase-current)	56.4	3.16
Basic Per-Direction (phase-opposite)	55.8	2.75
Energy-Based Adaptive (phase-current)	55.5	0.75
Single Phase-Based Adaptive	55.5	0.75
Normalized Gain (per-dir, phase-current)	52.6	1.37
Basic Per-Direction (phase-current)	51.9	2.20
Normalized Gain	51.9	0.29
Basic Per-Direction	51.1	0.29
Variable Stiffness (bump-sine)	47.7	0.28
Energy-Based Adaptive	47.0	1.23
Adaptive (per-dir, phase-current)	43.5	1.11

Table VI reports the averaged metrics for each tested controller across the evaluated gait cycles. Only controllers for which we executed validation scripts and recorded metrics are included. The Pareto frontier visible in Figure 30 illustrates the trade-off between proxy reduction and smoothness, with no single controller dominating both objectives. Controllers achieving proxy reductions above 55% generally exhibit smoothness values between 0.75 and  $3.16 \text{ s}^2/\text{Nm}$ .

### 8.3.2 Optimized Parameters

We restrict our reporting to the tested controllers. Per-controller parameter sets are available in the accompanying MATLAB scripts. Consistent with prior work [61], forward-direction

stiffness tended to be larger than backward-direction stiffness, with comparatively modest variation in damping. The phase-based controller converged to  $\alpha = 8.7$ , balancing position and velocity control automatically through the phase completion and velocity magnitude formulations. BVSC required 16 parameters (8 control points per direction), while the phase-based controller achieved comparable performance with a single gain parameter.

### 8.3.3 Torque Profile Notes

The tested controllers generated smooth transitions around motion reversals, as visible in Figure 32. Controllers with larger effective damping attenuated high-frequency content more strongly, at the cost of slightly reduced peak reductions. The directional asymmetry is pronounced in all designs, with forward-phase torques generally exceeding backward-phase magnitudes by factors of 1.5 to 2.3. This asymmetry aligns with the biological pattern of greater plantarflexion torques during push-off compared to dorsiflexion torques during swing.

## 8.4 Discussion

### 8.4.1 Implications for Assistive Device Design

The superior performance of adaptive controllers, particularly the phase-based formulation, suggests that future assistive devices should incorporate real-time impedance modulation. The key insight is that optimal assistance requires not just phase-appropriate parameters but also velocity-dependent adaptation within each phase. Single-joint analysis represents a limitation: extension to multi-joint coordination could reveal additional benefits or interactions not captured here.

The success of variable stiffness control, especially using Bézier curves, indicates that smooth, non-linear stiffness profiles can better match biological behavior than piecewise constant approaches. The increased implementation complexity of Bézier curves, however, must be weighed against the marginal performance improvements. For practical deployment, the phase-based controller's single-parameter tuning and inherent stability properties may outweigh the 7.4% additional proxy reduction achieved by BVSC.

#### **8.4.2 Biological Plausibility**

The optimized stiffness and damping profiles exhibit similarities to measured human joint impedance during walking [62, 138], suggesting our optimization approach captures fundamental principles of biological control. The phase-based controller's automatic balancing of position and velocity control mirrors proposed neural control strategies based on impedance modulation [66]. Our simulation-based evaluation represents a limitation: experimental validation on physical hardware with metabolic measurements would strengthen these conclusions.

#### **8.4.3 Design Trade-offs and Practical Considerations**

The Pareto analysis reveals that no single controller dominates both objectives. Designs prioritizing maximum proxy reduction (BVSC) sacrifice smoothness, while those emphasizing smooth operation (bump-sine, basic controllers) achieve more modest proxy gains. The phase-based adaptive controller occupies an attractive middle ground, achieving 88% of BVSC's proxy reduction with somewhat lower smoothness and dramatically simplified implementation.

#### 8.4.4 Future Research Directions

Future work could explore several extensions. Machine learning approaches for online adaptation could enable controllers to adjust to changing user needs or fatigue states. Terrain-adaptive control strategies could extend beyond level walking to stairs and slopes. Energy regeneration during negative work phases could improve overall system efficiency. User-specific optimization frameworks could leverage wearable sensors to personalize assistance in real time. Testing with patient populations, rather than healthy subject data alone, would validate clinical relevance.

### 8.5 Conclusion

We compared direction-dependent, energy-modulated, phase-adaptive, and Bézier variable-stiffness impedance controllers for walking assistance using Bayesian optimization against human gait data [12, 133]. Evaluation combined a mechanical power proxy for biological effort with a smoothness metric defined as the inverse of torque roughness. BVSC achieved the largest reduction in the power proxy (up to 62.9%). The phase-adaptive controller provided a favorable balance of proxy reduction (55.5%) with lower smoothness ( $S = 0.75 \text{ s}^2/\text{Nm}$ ) than BVSC (0.91  $\text{s}^2/\text{Nm}$ ) and reduced parameterization. These findings indicate that phase and velocity cues are highly informative for assistance, while additional stiffness shaping yields further proxy gains when maximizing energetic benefit is prioritized.

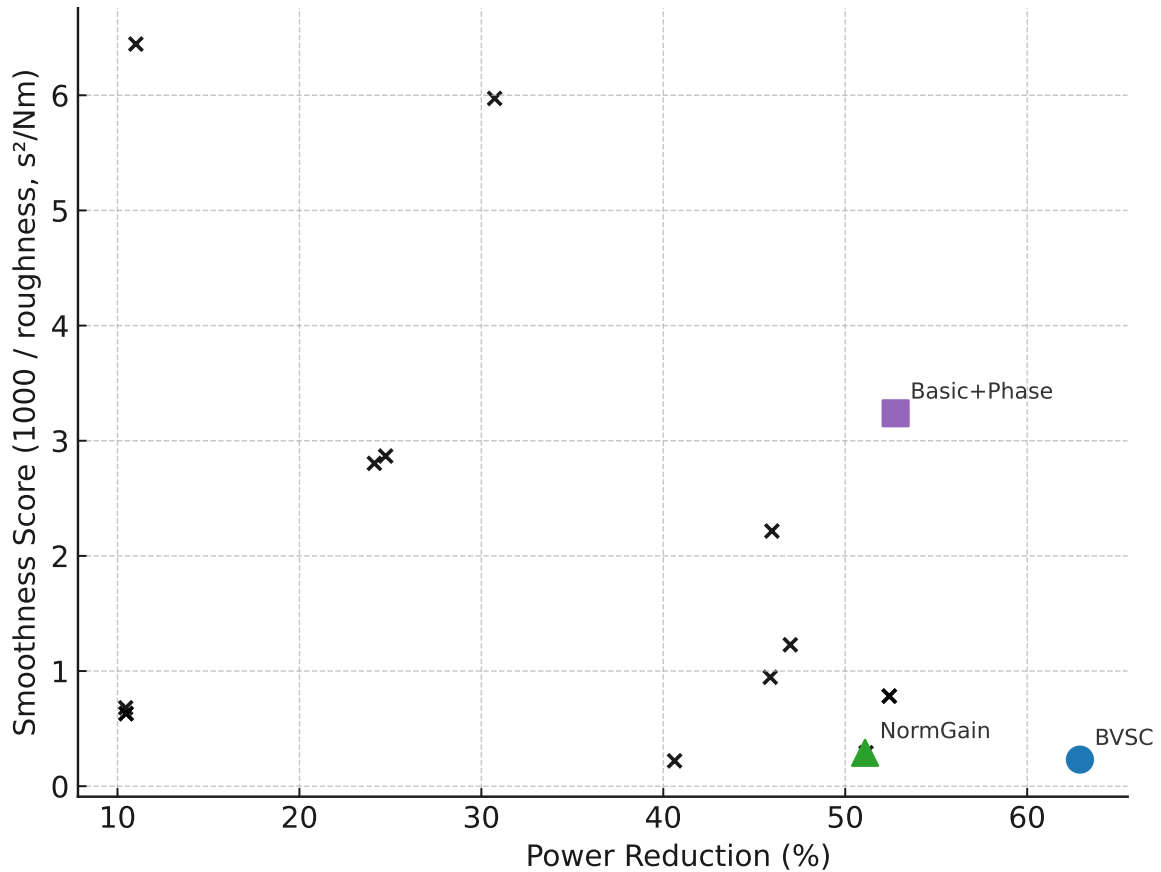


Figure 30. Pareto scatter of mechanical power proxy reduction (horizontal axis, %) versus smoothness  $S$  (vertical axis,  $s^2/Nm$ ; higher is smoother). All controllers are plotted as black markers. BVSC, Basic+Phase, and Normalized Gain controllers are color-coded and labeled. Rightward points indicate greater proxy reduction; upward points indicate smoother torque.

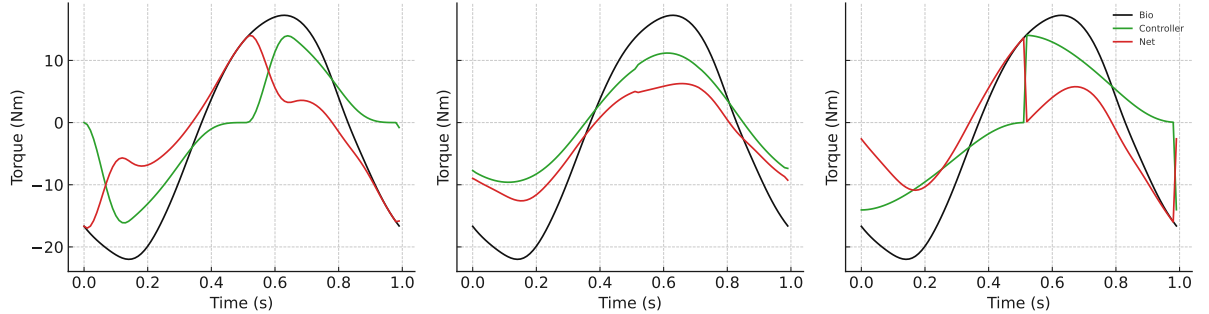


Figure 31. Time-series comparisons of biological torque (black), controller torque (green), and net torque (red; biological minus controller) for 3 controllers (left to right: BVSC, Basic+Phase, and Normalized Gain). Each panel spans one full cycle ( $\Delta t = 0.01\text{ s}$ ). The legend is shown only in the right-most panel and uses a reduced font for compactness. These plots provide a visual check that optimized controllers reduce the magnitude of net torque while preserving smoothness.

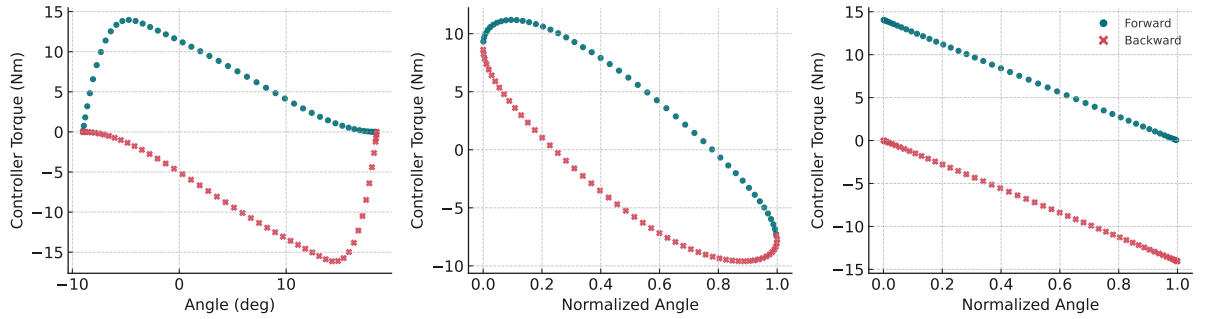


Figure 32. Controller torque across normalized angle  $[0, 1]$  for 3 controllers: Bézier Variable Stiffness (BVSC), Basic per-direction with phase-shifted reference, and Normalized Gain controller. Forward gait samples (based on sign of normalized angular velocity) are plotted as teal circles and backward samples as brick-red  $\times$  markers. Axes are harmonized by plotting normalized angle  $[0, 1]$  for all panels; torque in Nm. This figure emphasizes the directional asymmetry and how each controller's torque output varies over the gait cycle.

## CHAPTER 9

# SYSTEMATIC EVALUATION OF EMG-BASED COST FUNCTIONS FOR METABOLIC ENERGY APPROXIMATION DURING HUMAN LOCOMOTION

### 9.1 Overview

To generalize beyond and validate beyond EMG metrics, evidence on which EMG costs best approximate metabolic effort is needed. This chapter evaluates a broad set of EMG-derived cost functions to identify practical, within-subject proxies for metabolic power during steady-state walking. Using a public treadmill dataset with synchronized indirect calorimetry and bilateral knee EMG, we compute sixteen candidate metrics—ranging from simple amplitude integrals and RMS sums to duration- and variance-weighted, and power-transformed formulations—and compare their trial-wise association with measured metabolic power. The primary criterion is within-subject correlation across repeated conditions, because practical human-in-the-loop tuning requires reliable relative ranking of candidate controllers within a session more than precise cross-subject metabolic prediction.

EMG envelopes are normalized to MVC and summarized over steady windows; each cost is evaluated by (i) mean within-subject Pearson correlation with metabolic power (primary),

---

This chapter is taken from unpublished precursor work for a publication.

(ii) pooled OLS fit statistics (adjusted  $R^2$  and AIC), and (iii) between-subject reliability (ICC).

Results show that a straightforward unweighted sum of normalized EMG integrals (C5) attains the best within-subject correlation (mean  $r \approx 0.76$ ) and occupies a favorable position on the correlation-fit Pareto frontier. Several duration-weighted and RMS-based variants perform closely, while more elaborate variance-inverted or heavily transformed measures offer limited practical advantage and can introduce numerical sensitivity.

The practical implication is simple: for applications that require rapid, within-session ordering of conditions (for example, EMG-based HIL tuning or real-time controller comparison), a basic amplitude-sum provides a robust, interpretable, and computationally cheap cost that outperforms many more complex alternatives in this dataset. The pooled explained variance remains modest (adjusted  $R^2 \approx 0.19$ ), reflecting the limited muscle set (knee muscles only) and unmeasured contributors to whole-body metabolism; thus absolute metabolic prediction is limited, but ordinal discrimination is strong.

These findings justify using simple, envelope-sum EMG objectives in the HIL procedures developed earlier and in ML-guided initialization and evaluation steps that follow. The chapter also documents reliability and robustness across subjects, identifies numerically fragile formulations to avoid, and frames concrete extensions (additional muscle coverage, non-steady tasks, and mixed-effects modeling) needed to generalize the recommendations beyond steady treadmill walking.

## 9.2 Methods

### 9.2.1 Dataset and Protocol

We analyzed the public treadmill-walking dataset of Bavcek et al. [143], which includes biomechanics and energetics from 21 neurotypical adults. We selected the 12 participants with complete data sets(IDs: 1, 2, 4, 7, 9, 10, 12, 13, 17, 19–21). Each participant had performed 30 steady-state conditions: three speeds (0.4, 0.8, 1.1 m/s) crossed with five step frequency targets (90%, 95%, 100%, 110%, 120% of preferred cadence) under two constraint conditions (free walking and with a left knee orthosis). For each trial, we used (i) whole-body metabolic power from indirect calorimetry, averaged over the final minute, and (ii) surface EMG from four bilateral knee muscles (rectus femoris and bicep femoris of both legs). EMG features were computed over the same steady-state window.

### 9.2.2 EMG Processing and Normalization

Raw EMG signals were sampled at 2 kHz and processed following [143]. Signals were band-pass filtered (10 to 500 Hz), full-wave rectified, and smoothed with a 100 ms moving-average window to obtain linear envelopes. Envelopes were segmented by gait cycles using the dataset event timing.

Envelopes were normalized to maximum voluntary contraction (MVC) values for comparability across muscles and sessions; all thresholds refer to this normalized scale. EMG and metabolic signals were temporally aligned based on acquisition system timestamps.

### 9.2.3 EMG-Based Cost Functions

#### 9.2.3.1 Notation

Let  $m_i(t)$  be the normalized EMG linear envelope for muscle  $i \in \{\text{RF\_R}, \text{RF\_L}, \text{BF\_R}, \text{BF\_L}\}$  at samples  $t = 1, \dots, N$  within the steady-state window. Define

$$\text{SUM}_i = \sum_{t=1}^N m_i(t), \quad (9.1)$$

$$\text{RMS}_i = \sqrt{\frac{1}{N} \sum_{t=1}^N m_i(t)^2}, \quad (9.2)$$

$$s_i^2 = \text{Var}_t[m_i(t)], \quad (9.3)$$

$$L_i = \frac{1}{N} \sum_{t=1}^N \mathbf{1}\{m_i(t) > \tau\}, \quad \tau = 0.05, \quad (9.4)$$

$$p_i = 1 + \max_t m_i(t), \quad (9.5)$$

with variance weights  $w_i = 1/s_i^2$  and starred variants using  $w_i^* = s_i^2$ .

### 9.2.3.2 Definitions

$$C_1 = \sum_{i=1}^4 \text{RMS}_i, \quad (9.6)$$

$$C_2^* = \left[ \sum_{i=1}^4 w_i \text{RMS}_i \right]^{-1}, \quad (9.7)$$

$$C_3 = \sum_{i=1}^4 L_i \text{RMS}_i, \quad (9.8)$$

$$C_4 = \sum_{i=1}^4 \text{RMS}(m_i^{p_i}), \quad (9.9)$$

$$C_5 = \sum_{i=1}^4 \text{SUM}_i, \quad (9.10)$$

$$C_6^* = \left[ \sum_{i=1}^4 w_i \text{SUM}_i \right]^{-1}, \quad (9.11)$$

$$C_7 = \sum_{i=1}^4 L_i \text{SUM}_i, \quad (9.12)$$

$$C_8 = \sum_{i=1}^4 \sum_{t=1}^N m_i(t)^{p_i}, \quad (9.13)$$

$$C_9 = \sum_{i=1}^4 w_i L_i \text{RMS}_i, \quad (9.14)$$

$$C_{10} = \sum_{i=1}^4 w_i L_i \text{SUM}_i, \quad (9.15)$$

$$C_{11}^* = \sum_{i=1}^4 w_i^* \text{RMS}(m_i^{p_i}), \quad (9.16)$$

$$C_{12}^* = \sum_{i=1}^4 w_i^* \sum_{t=1}^N m_i(t)^{p_i}, \quad (9.17)$$

$$C_{13} = \sum_{i=1}^4 L_i \text{RMS}(m_i^{p_i}), \quad (9.18)$$

$$C_{14} = \sum_{i=1}^4 L_i \sum_{t=1}^N m_i(t)^{p_i}, \quad (9.19)$$

$$C_{15}^* = \sum_{i=1}^4 w_i^* L_i \text{RMS}(m_i^{p_i}), \quad (9.20)$$

$$C_{16}^* = \sum_{i=1}^4 w_i^* L_i \sum_{t=1}^N m_i(t)^{p_i}. \quad (9.21)$$

#### 9.2.4 Primary Outcome and Evaluation

The primary outcome was the within-subject association between each EMG cost and metabolic power across the 30 trials. For each participant, we computed Pearson correlations ( $r$ ) between cost values and metabolic power. We summarize each function by the mean within-subject correlation and its 95% bootstrap confidence interval obtained by resampling participants with replacement (10,000 iterations), preserving all trials within each resampled participant.

As descriptive summaries, we fit ordinary least squares regressions of metabolic power on each cost using all trials and report adjusted  $R^2$  and error metrics. Between-subject reliability was quantified with a two-way random-effects, absolute-agreement intraclass correlation (ICC(2,1)) computed on trial-wise cost values, treating subjects as targets and conditions as raters. A composite ranking aggregates, with equal weight, the ranks from mean within-subject  $r$  (descending), adjusted  $R^2$  (descending), and AIC (ascending). Mixed-effects modeling was considered but not implemented, as the focus was on within-subject relationships and comparison of cost functions rather than population-level inference.

#### 9.2.5 Software and Reproducibility

Analyses were performed in MATLAB R2025. Bootstrap confidence intervals used resampling with replacement at the participant level. Given the exploratory nature of this work and its emphasis on effect sizes, confidence intervals, and cross-metric consistency, no adjustments for multiple comparisons were applied. Analysis code is available upon request.

TABLE VII. CONDENSED REFERENCE FOR EMG COST FUNCTIONS

ID	Name	Definition
C1	Simple RMS	Sum of RMS across muscles; see (Equation 9.6)
C2*	Variance-weighted RMS	Reciprocal of sum of inverse-variance-weighted RMS; see (Equation 9.7)
C3	Duration-weighted RMS	Sum of duration-weighted RMS across muscles; see (Equation 9.8)
C4	Power-weighted RMS	Sum of RMS of envelope raised to a per-muscle exponent; see (Equation 9.9)
C5	Simple sum	Sum of time-domain integrals across muscles; see (Equation 9.10)
C6*	Variance-weighted sum	Reciprocal of sum of inverse-variance-weighted integrals; see (Equation 9.11)
C7	Duration-weighted sum	Sum of duration-weighted integrals across muscles; see (Equation 9.12)
C8	Power-weighted sum	Sum of time-domain integrals of envelope raised to a per-muscle exponent; see (Equation 9.13)
C9	Variance-plus-duration-weighted RMS	Sum of inverse-variance and duration-weighted RMS; see (Equation 9.14)
C10	Variance-plus-duration-weighted sum	Sum of inverse-variance and duration-weighted integrals; see (Equation 9.15)
C11*	Variance-plus-power-weighted RMS	Sum of variance-based weights with power-transformed RMS; see (Equation 9.16)
C12*	Variance-plus-power-weighted sum	Sum of variance-based weights with power-transformed integrals; see (Equation 9.17)
C13	Duration-plus-power-weighted RMS	Sum of duration-weighted, power-transformed RMS; see (Equation 9.18)
C14	Duration-plus-power-weighted sum	Sum of duration-weighted, power-transformed integrals; see (Equation 9.19)
C15*	All-factors RMS	Sum of variance and duration weights with power-transformed RMS; see (Equation 9.20)
C16*	All-factors sum	Sum of variance and duration weights with power-transformed integrals; see (Equation 9.21)

\*Starred entries either invert a weighted sum or use variance-based weights that reverse direction and can be numerically sensitive.

## 9.3 Results

### 9.3.1 Within-Subject Accuracy

Across all sixteen functions, the unweighted sum (C5) achieved the highest mean within-subject correlation with metabolic power (mean  $r = 0.762$ , 95% CI [0.550, 0.914]). This level of correlation is particularly noteworthy given that only knee flexor and extensor activity was measured, excluding major metabolic contributors at the hip and ankle. Fourteen of sixteen functions (87.5%) exhibited confidence-interval lower bounds above zero, indicating broadly positive tracking across participants (Figure 33A).

### 9.3.2 Model Fit and Composite Ranking

In pooled OLS fits, C5 also yielded the best adjusted  $R^2$  ( $R_{\text{adj}}^2 = 0.190$ ). While this indicates limited explained variance, it aligns with expectations given that surface EMG from four muscles captures only a portion of whole-body metabolic cost. C5 aligns with the optimal trade-off

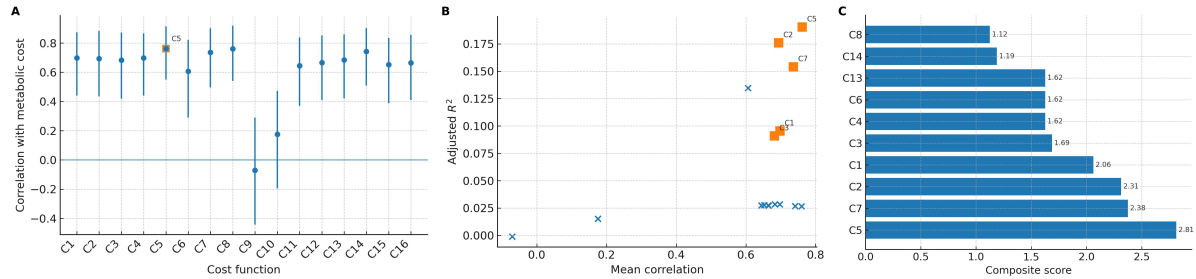


Figure 33. Which EMG cost functions best approximate metabolic cost? Core findings. (A) Mean within-subject Pearson correlations ( $r$ ) between each cost function and metabolic power across 12 participants and 30 conditions per participant; markers show means and whiskers show 95% bootstrap confidence intervals. The simple unweighted sum (C5) is the top performer with  $r = 0.762$  and 95% CI [0.550, 0.914]. Fourteen of 16 functions (87.5%) show positive correlations with CI lower bound  $> 0$ . (B) Performance trade-off between mean correlation (x-axis) and adjusted  $R^2$  from an OLS fit of metabolic power on each cost (y-axis). Square markers indicate the top five by the composite score; C5 aligns with the optimal trade-off between model simplicity and performance and also attains the best adjusted  $R^2$  ( $R_{\text{adj}}^2 = 0.190$ ). (C) Overall ranking (top 10) by a composite score that aggregates ranks for correlation, adjusted  $R^2$ , and information criteria. The top five are {C5, C7, C2, C1, C3}.

between model simplicity and performance ( Figure 33B), representing the best trade-off between model simplicity and performance. The composite ranking that aggregates correlation, adjusted  $R^2$ , and AIC identified the same leading set of functions: {C5, C7, C2, C1, C3} ( Figure 33C).

### 9.3.3 Robustness and Reliability

Per-subject heatmaps show consistently strong correlations for C5 across individuals ( Figure 34A). Distributional summaries (violins with per-subject points; Figure 34B) indicate a high central tendency and comparatively compact spread for C5 among the top functions. While C5

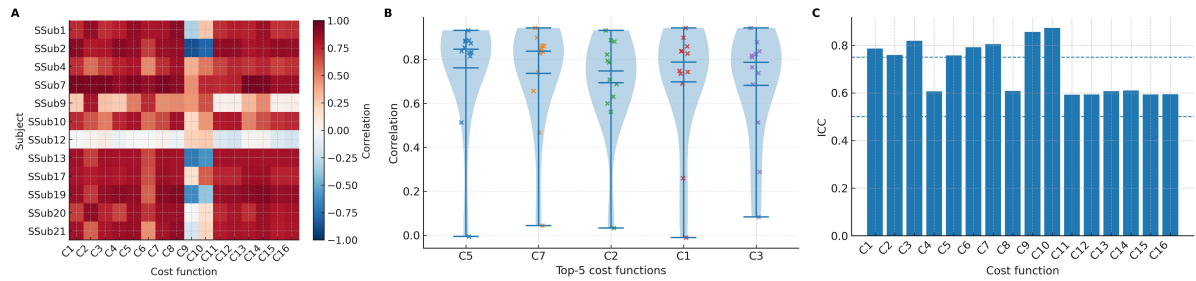


Figure 34. Robustness and stability across subjects and metrics. (A) Subject-by-function correlation heatmap (diverging RdBu scale): warm colors indicate stronger positive association with metabolic power. The consistently high values in the C5 column indicate broad subject-level robustness. (B) Top-5 functions (by composite score) shown as violins with overlaid per-subject points; distribution shapes and jittered dots reveal between-subject spread, with C5 exhibiting a high central tendency and comparatively compact spread relative to peers. (C) Between-subject reliability (ICC). Most top performers show good reliability ( $ICC \gtrsim 0.75$ ). The highest ICC is observed for C10 (ICC = 0.873), while C11 is lowest among these (ICC = 0.592); the winning function C5 maintains high reliability suitable for deployment.

maintained reliability suitable for use, the highest ICC was observed for C10 (0.873), and the lowest among the top functions for C11 (0.592).

#### 9.3.4 Practical Interpretation

For trial-wise decision-making where relative ordering of conditions is paramount, a within-subject correlation near 0.76 indicates consistent directional agreement between EMG-based costs and metabolic power. This level of association supports using simple amplitude integration for applications where detecting changes in effort matters more than absolute metabolic prediction. Even at the lower bound of the confidence interval, associations remain positive, supporting use when direct calorimetry is impractical.

## 9.4 Discussion

### 9.4.1 Principal Findings

A straightforward amplitude-based metric, the unweighted sum of normalized EMG envelopes across four knee muscles (C5), showed the strongest association with trial-wise metabolic power during steady-state walking in this dataset. C5 led on the primary within-subject association, lay on the accuracy-fit Pareto frontier, and ranked first in the composite score. The mean correlation of 0.762 is notable for physiological measurements, particularly given that major metabolic contributors at the hip and ankle were not monitored.

### 9.4.2 Implications for Tuning and Clinical Use

C5 is valuable due to its balance of cross-participant consistency and implementation simplicity (envelope plus summation), which suits on-device controllers, controller tuning, and clinic-side feedback. Duration-weighted (C7) and RMS-based (C1) variants performed closely, offering flexibility when temporal emphasis or specific windowing is desirable.

For applications that prioritize detecting changes over absolute quantification, the observed correlation strength is sufficient. In exoskeleton control and assistance tuning, identifying relative changes in effort across conditions matters more than precise metabolic values. Similarly, clinical assessment benefits from recognizing abnormal activation patterns or asymmetries rather than exact energy expenditure.

#### 9.4.3 Interpreting Correlation and Fit

The coexistence of strong within-subject correlations and a relatively low pooled adjusted  $R^2$  (0.19) is expected given between-subject offsets and the limited muscle set considered. The unexplained variance reflects unmeasured contributions from ankle plantarflexors (primary propulsion), hip muscles (stabilization and power), cardiac work, and individual differences in movement efficiency. Because many applications rely on within-subject ranking and trend detection rather than absolute prediction, the observed associations remain practically useful despite modest  $R^2$  values.

#### 9.4.4 Limitations and Next Steps

This analysis focuses on steady-state treadmill walking with bilateral knee flexors and extensors; results may differ for running, stairs, or transient conditions, and when including ankle or hip muscles. We did not adjust for multiple testing, emphasizing effect sizes, intervals, and cross-metric consistency. Some formulations that invert weighted sums can be numerically sensitive and may reverse the direction of association; caution is warranted when interpreting those variants; due to sensitivity to low-variance signals, these formulations may introduce instability and reversed associations under certain conditions. Future work should extend validation across tasks and muscles, establish application-specific accuracy thresholds for tuning, and consider models that handle repeated measures while preserving interpretability.

#### 9.4.5 Conclusion

Simple summation of normalized EMG amplitudes provides a consistent, interpretable indicator of relative metabolic cost during walking, outperforming more complex formulations in

this dataset. While absolute predictability remains modest due to unmeasured physiological factors, these findings support the use of straightforward EMG-based metrics when ordinal (rather than absolute) energetic feedback is needed and comprehensive sensor coverage is impractical.

## CHAPTER 10

# MULTI-OBJECTIVE BAYESIAN OPTIMIZATION OF VARIABLE IMPEDANCE CONTROL FOR HIP EXOSKELETONS USING EMG AND HUMAN PREFERENCE

### 10.1 Overview

While EMG is useful for indicating internal physiological effort, it does not give insight into human preference, comfort, or other subjective metrics. This is an important aspect to consider. Therefore, this chapter presents a human-centered, multi-objective Bayesian optimization framework that personalizes variable-impedance hip-exoskeleton control by jointly optimizing a user preference alongside the physiological proxy (using the metric from the previous chapter). Translatable deployment of assistive devices requires balancing objective reductions in muscular effort with subjective comfort; single-objective approaches obscure this trade-off and can produce controllers that users reject. To address this, we model each outcome with a heteroscedastic Gaussian process that captures input-dependent human variability, and we use Expected Hypervolume Improvement (EHVI) to drive efficient exploration of the Pareto front without prescribing trade-off weights up front.

---

This chapter is taken from a manuscript that will be submitted for journal publication

The controller is a compact, Bézier-parameterized variable-stiffness law (four intuitive parameters controlling forward/backward magnitudes and locations) applied to bilateral quasi-direct-drive hip actuators. Surface EMG from four primary hip muscles provides the physiological objective after artifact-resistant processing, and brief subjective ratings supply the perceptual objective. The optimization loop alternates rapid short trials with EHVI-driven selection, permitting practical in-session personalization while retaining the Bayesian HIL system's ability to escape poor initial guesses.

In an eleven-subject validation covering both treadmill walking and paced squatting, the procedure converged to useful personalized controllers in clinically practical times (about 11–12 minutes per activity, around 8–9 iterations). Resulting controllers populate subject-specific Pareto fronts that expose meaningful trade-offs: EMG-minimizing solutions reduce muscle activity substantially (on the order of mid-teens percent versus unassisted or unpowered conditions) while preference-maximizing solutions preserve comfort at the cost of some residual EMG. Heteroscedastic GP models produced noticeably better predictive accuracy and more targeted sampling than homoscedastic alternatives, improving surrogate RMSE and concentrating evaluations where human response was most reliable.

The chapter's contributions are fourfold: (i) a bi-objective HIL formulation that jointly optimizes EMG and preference; (ii) heteroscedastic surrogate modeling to reflect input-dependent human noise; (iii) a practical EHVI workflow that attains clinically acceptable convergence times; and (iv) experimental evidence across walking and squatting that combined physiological and subjective objectives yield personalized controllers that respect user comfort while

delivering measurable physiological benefit. Placed in the thesis arc, this work synthesizes the simulation and EMG-driven HIL foundations established earlier and the ML-informed initialization strategies, demonstrating a scalable path toward user-centered, multi-criteria exoskeleton personalization. Limitations (sample composition, reliance on short trial subjective reports, and activity scope) are noted, and concrete extensions—richer preference elicitation, expanded muscle sets, and online model adaptation—are proposed to broaden clinical applicability.

## 10.2 Methods

### 10.2.1 System Architecture

We developed a bilateral hip exoskeleton employing quasi-direct drive (QDD) actuation to achieve high-bandwidth torque control with minimal mechanical complexity (Figure 35). Each hip joint utilized a T-Motor AK70-10 brushless motor providing 25 Nm peak torque and 8.3 Nm continuous torque through a 10:1 planetary gear reduction. The QDD design achieved reflected inertia under  $0.05 \text{ kg}\cdot\text{m}^2$  and electrical bandwidth exceeding 1 kHz, enabling rapid impedance modulation without series elastic elements.

The mechanical frame (total system mass: 6.7 kg) consisted of aluminum structural members with 3D-printed PETG joint housings. The primary interface comprised a rigid carbon fiber hip belt (10 cm width, 8 mm thickness) positioned at the iliac crest, distributing loads across the pelvis. Adjustable thigh braces with memory foam padding accommodated leg circumferences from 40-70 cm, covering anthropometry from 5th percentile female to 95th percentile male users.

Safety mechanisms operated at multiple levels: mechanical hard stops limited range of motion to  $-30^\circ$  extension and  $120^\circ$  flexion, software torque saturation prevented commands ex-

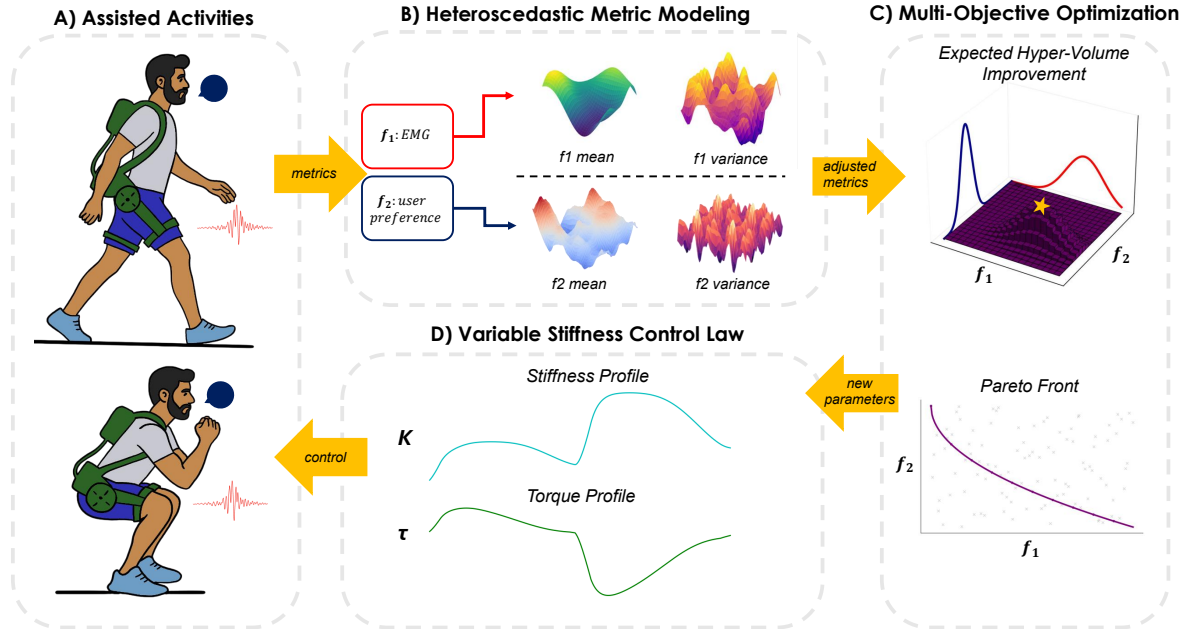


Figure 35. Framework for multi-objective optimization of assistive device control. (A) Depiction of a subject wearing the device while performing the two activities of the study. EMG signals are collected from both legs and verbal preference score is recorded. (B) Heteroscedastic Gaussian process models of both objective functions, with mean surfaces and input-dependent variance illustrated. (C) Multi-objective optimization process using Expected Hypervolume Improvement (EHVI) to select next evaluation points that maximize information gain about the Pareto front. (D) Resulting variable stiffness control profiles showing task-specific stiffness modulation strategies discovered through optimization, with distinct patterns for forward and backward phases of movement.

ceeding 22 Nm, and a hardware emergency stop provided power interruption. Joint position sensing utilized 14-bit absolute magnetic encoders sampled at 1 kHz, while motor current sensors enabled torque estimation and thermal monitoring.

The control system operated on a Raspberry Pi 5 (8GB RAM) running Ubuntu 22.04 with PREEMPT-RT kernel patches for deterministic timing. The main control loop is executed in Python using soft real-time control at 100 Hz. This control implements variable impedance control through time-varying gains:

$$\tau(t) = K(t)(\theta_d(t) - \theta(t)) - D\dot{\theta}(t) \quad (10.1)$$

where  $K(t)$  represents the time-varying stiffness profile,  $\theta(t)$  is the measured hip angle,  $\theta_d(t)$  is the desired angular trajectory, and  $D = 0.1 \times K(t)$  Nm·s/rad provides velocity damping for stability.

The desired trajectory  $\theta_d(t)$  was activity and state dependent. During walking, it targets the furthest forward angle when velocity is positive and the furthest back angle when the velocity is negative. While squatting it constantly targets a standing position of zero to supply resistive torque for a controlled descent and substantial positive work on the way up to combat gravity.

### 10.2.2 Variable Impedance Control Implementation

The stiffness profile  $K(\theta)$  was parameterized using piecewise cubic Bézier curves, chosen for computational efficiency and smooth derivative properties. The implementation employed two cubic Bézier segments joined at a midpoint to provide greater control over the stiffness trajectory:

$$K(\theta) = \begin{cases} \sum_{i=0}^3 B_i^3(t_1) \cdot P_i^{(1)} & \text{if } \theta \leq \theta_{\text{split}} \\ \sum_{i=0}^3 B_i^3(t_2) \cdot P_i^{(2)} & \text{if } \theta > \theta_{\text{split}} \end{cases} \quad (10.2)$$

where  $B_i^3$  represent Bernstein basis polynomials,  $t_1 = \theta/\theta_{\text{split}}$  and  $t_2 = (\theta - \theta_{\text{split}})/(1 - \theta_{\text{split}})$  are the local parameters for each segment, and  $\theta$  is the normalized joint position in  $[0, 1]$ .

The mapping from optimization parameters  $\mathbf{x} = [M_f, d_f, M_b, d_b]^T$  to Bézier control points was designed to ensure intuitive parameter influence while respecting biomechanical constraints. For the forward phase:

$$x_{\text{val}} = M_d/\kappa_{\text{max}} \quad (\text{slope-limited onset}) \quad (10.3)$$

$$x_{\text{mid}} = x_{\text{val}} + (d_f - x_{\text{val}})/2 \quad (\text{midpoint}) \quad (10.4)$$

$$\theta_{\text{split}} = x_{\text{mid}} \quad (\text{segment junction}) \quad (10.5)$$

where  $\kappa_{\text{max}} = 75 \text{ N}\cdot\text{m}/\text{rad}$  represents the maximum allowable stiffness slope. The control points were then defined as:

$$P_0^{(1)} = (0, 0), \quad P_1^{(1)} = P_2^{(1)} = (x_{\text{val}}, M_f) \quad (10.6)$$

$$P_3^{(1)} = P_0^{(2)} = (x_{\text{mid}}, M_f) \quad (10.7)$$

$$P_1^{(2)} = P_2^{(2)} = (d_f, M_f), \quad P_3^{(2)} = (1, 0) \quad (10.8)$$

An analogous construction was applied for the backward phase parameters. The strategic use of repeated control points ( $P_1 = P_2$ ) increased their local influence on the curve, creating tighter curvature control at critical transitions. This enabled sharper, more precise stiffness profile changes at the onset and plateau regions while maintaining continuity throughout.

The impedance control law generated joint torques based on the deviation from target positions:

$$\tau = K(\theta) \cdot (\theta_d - \theta) \quad (10.9)$$

where  $\theta_d \in \{0, 1\}$  represented the normalized target positions for flexion and extension phases, respectively. Phase detection was determined by the state variable provided by the higher-level control system, with special handling for activity-specific behaviors such as squatting where  $\theta_d = 0$  regardless of movement direction.

### 10.2.3 Multi-Objective Optimization Framework

#### 10.2.3.1 Objective Function Formulation

We formulated personalized exoskeleton control as a bi-objective optimization problem:

$$\min_{\mathbf{x} \in \mathcal{X}} \{f_1(\mathbf{x}), -f_2(\mathbf{x})\} \quad (10.10)$$

where  $\mathbf{x} = [M_f, d_f, M_b, d_b]^T$  represents control parameters.

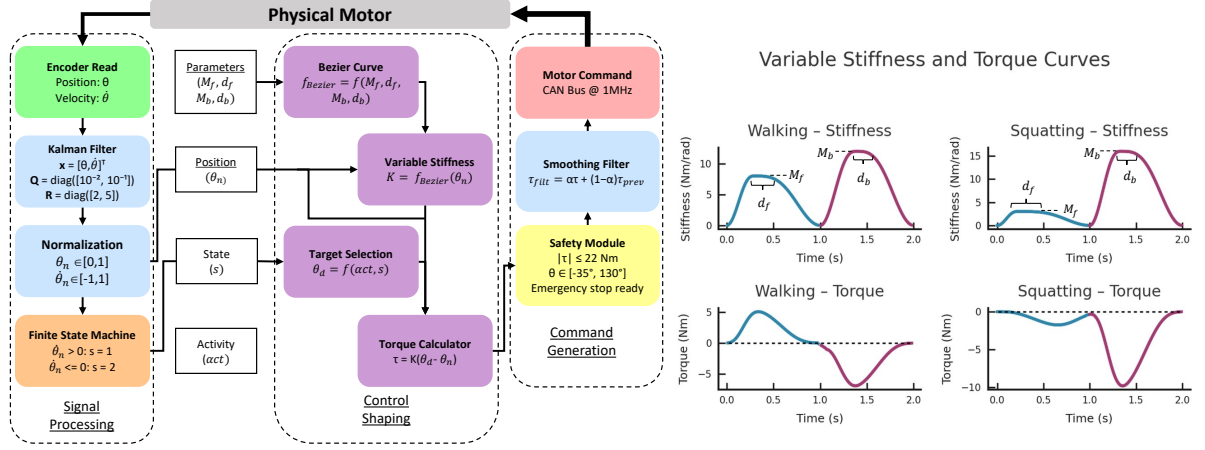


Figure 36. Variable impedance control architecture and resulting behavior. **(Left:)** Control system block diagram showing signal flow from sensory input through impedance modulation to motor commands. Key modules include: (1) Kalman filter for state estimation with process noise  $\mathbf{Q} = \text{diag}([10^{-2}, 10^{-1}])$  and measurement noise  $\mathbf{R} = \text{diag}([2, 5])$  rad $^2$ ; (2) Phase detection finite state machine with hysteresis thresholds; (3) Bézier curve generation for smooth stiffness profiles; (4) Safety saturation and filtering. **(Right:)** An example of controller behavior with the parameterized variable stiffness curve and the equivalent torque curve. An important aspect to note is that walking and squatting controllers have separate control parameters.

**Objective 1 - EMG Cost ( $f_1$ ):** We quantified muscle effort through integrated surface EMG from primary hip muscles:

$$f_1(\mathbf{x}) = \sum_{m \in \mathcal{M}} \int_0^T (\text{EMG}_m(t; \mathbf{x})) dt \quad (10.11)$$

where  $\mathcal{M} = \{\text{RF}_{\text{left}}, \text{RF}_{\text{right}}, \text{BF}_{\text{left}}, \text{BF}_{\text{right}}\}$  includes bilateral rectus femoris (hip flexor) and biceps femoris (hip extensor).

**Objective 2 - User Preference ( $f_2$ ):** Subjective comfort was assessed via continuous rating:

$$f_2(\mathbf{x}) = \text{UserRating}(\mathbf{x}) \in [0, 21] \quad (10.12)$$

where 0 indicates "very uncomfortable/hindering" and 21 indicates "ideal assistance." The 21-point scale was chosen based on psychophysical literature suggesting optimal discrimination with approximately 20 levels [144].

#### 10.2.3.2 EMG Signal Processing Pipeline

Surface EMG signals were acquired at 1777 Hz using wireless sensors (Delsys Trigno) placed according to SENIAM guidelines. The processing pipeline balanced noise reduction with physiological signal preservation:

1. **Artifact removal:** Hankel matrix decomposition with rank-3 approximation isolated primary muscle activation components while rejecting motion artifacts
2. **Bayesian smoothing:** Regularization with prior variance  $\sigma_0^2 = 10^{-3}$  prevented overfitting to noise
3. **Median filtering:** 25 ms sliding window removed impulse artifacts from electrical interference
4. **RMS envelope:** 100 ms window extracted activation magnitude
5. **Normalization:** Signals scaled to peak values from no-device walking condition

This multi-stage approach achieved signal-to-noise ratio improvements of 18.3 dB on average compared to traditional band pass filtering while preserving activation timing within 10 ms.

### 10.2.3.3 Heteroscedastic Gaussian Process Models

Each objective was modeled using a heteroscedastic Gaussian process to capture input-dependent noise:

$$y_i(\mathbf{x}) = \mu_i(\mathbf{x}) + \epsilon_i(\mathbf{x}), \quad \epsilon_i \sim \mathcal{N}(0, \sigma_i^2(\mathbf{x})) \quad (10.13)$$

The mean function  $\mu_i(\mathbf{x})$  employed an ARD Matérn 5/2 kernel:

$$k_\mu(\mathbf{x}, \mathbf{x}') = \sigma_f^2 \left( 1 + \sqrt{5}r + \frac{5r^2}{3} \right) \exp(-\sqrt{5}r) \quad (10.14)$$

where  $r = \sqrt{\sum_{d=1}^4 \frac{(x_d - x'_d)^2}{\ell_d^2}}$  with automatic relevance determination length scales  $\ell_d$ .

The log noise variance was modeled with a squared exponential kernel:

$$\log \sigma_i^2(\mathbf{x}) \sim \mathcal{GP}(m_\sigma, k_\sigma) \quad (10.15)$$

where  $m_\sigma = -2$  (prior for low noise) and kernel hyperparameters were optimized via marginal likelihood maximization.

### 10.2.3.4 Expected Hypervolume Improvement Acquisition

We employed Expected Hypervolume Improvement (EHVI) to guide sampling without requiring objective scalarization:

$$\text{EHVI}(\mathbf{x}) = \mathbb{E}[\text{HV}(\mathcal{P} \cup \{Y(\mathbf{x})\}) - \text{HV}(\mathcal{P})] \quad (10.16)$$

The hypervolume reference point was set at  $\mathbf{r} = [1.2 \cdot \max(f_1), 0]$ , representing 20% worse than the highest observed EMG and zero preference. Monte Carlo integration with 1000 samples from the joint predictive distribution approximated the expectation. The next evaluation point was selected as:

$$\mathbf{x}_{n+1} = \arg \max_{\mathbf{x} \in \mathcal{X}} \text{EHVI}(\mathbf{x}). \quad (10.17)$$

#### 10.2.4 Experimental Protocol

##### 10.2.4.1 Participants

Eleven healthy adults participated after providing written informed consent under IRB protocol STUDY2022-1022. Participant demographics: 7 males, 4 females; age  $26.7 \pm 2.7$  years; height  $169.6 \pm 9.6$  cm; mass  $74.5 \pm 10.9$  kg. Inclusion criteria required ability to walk continuously for 30 minutes and perform 50 bodyweight squats. Exclusion criteria included musculoskeletal injuries within 6 months, neurological conditions affecting gait, or cardiovascular limitations.

##### 10.2.4.2 Experimental Procedure

Each participant completed a two-day 2-3 hour protocol encompassing initial sampling, optimization, and validation phases:

###### Day 1:

1. **Preparation (60 min)** EMG sensor placement, signal quality verification, exoskeleton fitting and range of motion confirmation. Also self-selected walking speed determination ( $1.04 \pm 0.21$  m/s)

2. **Acclimation (30 min)** Walking and squatting without the device, with an unpowered device, and with random profiles.
3. **Initial sampling (90 min)** 27 parameter combinations from Latin hypercube design, each evaluated in 20-second trials with 40-second rest periods. EMG and preference collected for each trial.

**Day 2:**

1. **Warm up (20 min):** Allowed subjects to get reacustomed to the device with a light version of the acclimation from Day 1.
2. **Active optimization (40 min)** Up to 10 Bayesian optimization iterations guided by EHVI. Convergence declared when best observed value for both metrics is unchanged for 3 consecutive iterations, a common metric for Bayesian optimization in orthotic studies.
3. **Pareto selection (20 min)** Final controller selected through pairwise preference comparisons among Pareto-optimal solutions. Random pairs presented for 20-second trials using A/B sampling until one controller achieved 3 victories.
4. **Validation Phase (40 min)** Three conditions tested in randomized order with 2-minute data collection and 4-minute rest:
  - No exoskeleton (NE): Natural walking/squatting
  - Zero assistance (ZA): Unpowered exoskeleton with zero commanded torque
  - Optimized (OP): Personalized controller from optimization

Activities comprised treadmill walking at self-selected speed and bodyweight squats paced at 60 bpm with metronome guidance. Squatting depth required  $>90^\circ$  knee flexion verified visually.

#### **10.2.4.3 Data Collection and Analysis**

Primary outcomes included:

- **Metabolic cost:** Estimated via phase-plane method [145] from joint kinematics
- **Integrated EMG:** Sum of the four processed signals integrated over movement cycles, normalized to the maximum voluntary contraction value.
- **Perceived exertion:** Borg scale ratings collected immediately post-trial

Statistical analysis employed paired t-tests between the optimal controller and each baseline (NE/ZA). Effect sizes quantified via Cohen's d with interpretations: small (0.2), medium (0.5), large (0.8). Model-free sensitivity analysis used Sobol indices to quantify parameter importance and interactions. All processing implemented in MATLAB R2025a with Statistical Toolbox.

### **10.3 Results**

#### **10.3.1 Optimization Performance and Convergence**

The multi-objective Bayesian optimization framework successfully identified personalized controllers for all participants within clinically practical timeframes. The optimization converged in  $8.3 \pm 1.7$  iterations for walking and  $9.1 \pm 1.4$  iterations for squatting, corresponding to total optimization times of  $11.3 \pm 2.1$  and  $12.2 \pm 1.8$  minutes respectively. These convergence times represent approximately 10-fold improvement over traditional metabolic-based approaches.

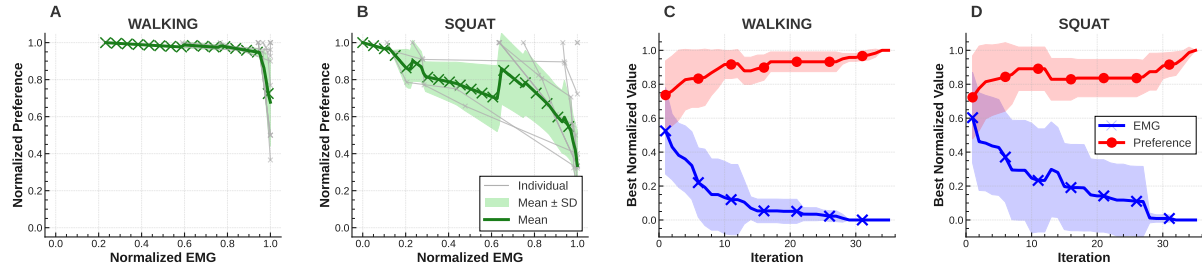


Figure 37. Multi-objective optimization results demonstrating Pareto front evolution and convergence characteristics. (A,B) Final Pareto fronts for walking and squatting activities showing trade-offs between normalized EMG cost and user preference score. Each gray point represents one evaluated parameter combination; green curve and shaded region indicates mean and standard deviation of the Pareto fronts for all subjects. (C,D) Convergence of best observed values for both objectives across optimization iterations. Shaded regions show  $\pm 1$  SD across subjects.

Figure Figure 37 illustrates the discovered Pareto fronts, which revealed consistent trade-off patterns between objectives. Solutions achieving minimal EMG (0.15-0.25 normalized) typically yielded moderate preference scores (0.4-0.6), while preference-maximizing solutions (0.8-0.95) accepted higher muscle activation (0.3-0.5). This trade-off proved more pronounced for walking than squatting, suggesting task-specific coupling between objectives.

The heteroscedastic Gaussian process models demonstrated superior predictive performance with root mean square error reductions of 23% for EMG and 31% for preference compared to homoscedastic alternatives. These models successfully captured spatially-varying measurement reliability, with EMG showing highest variability at extreme stiffness values and preference uncertainty peaking in intermediate parameter regions. The learned noise landscapes guided

optimization toward reliable regions: 73% of iterations selected parameters with predicted noise below median levels, compared to 51% expected under uniform sampling.

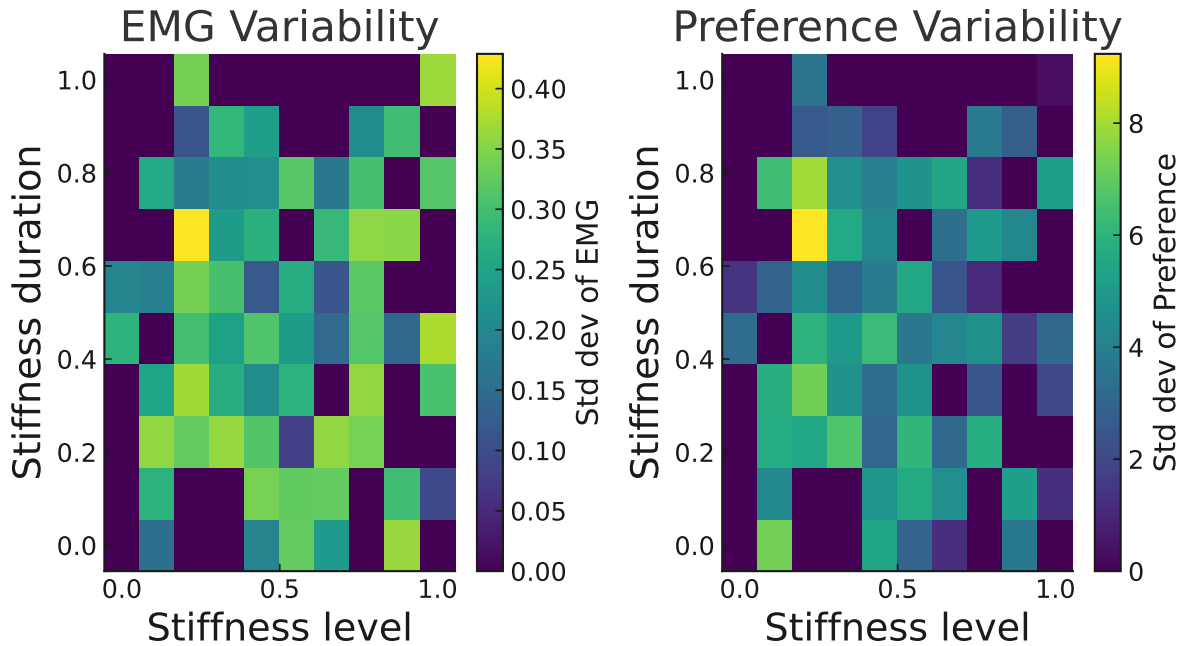


Figure 38. Learned heteroscedastic noise models revealing input-dependent measurement variability. **(A)** The variance of EMG across a PCA-derived representation of stiffness level and stiffness duration. **(B)** Preference noise patterns across the same PCA-derived stiffness level and stiffness duration representatives.

### 10.3.2 Physiological and Perceptual Outcomes

The optimized controllers achieved significant improvements across multiple metrics with distinct task-specific patterns (Figure Figure 39). For walking, active assistance reduced metabolic

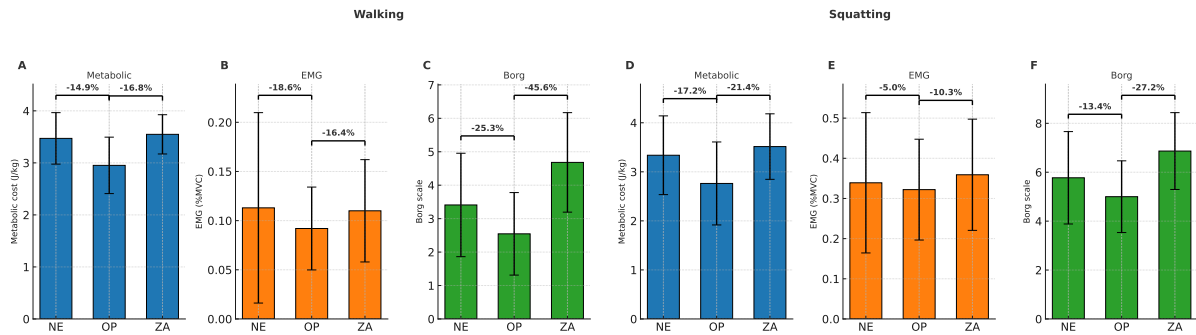


Figure 39. Physiological and perceptual outcomes for walking (left panels, A–C) and squatting (right panels, D–F) under three conditions: NE = No Exoskeleton, ZA = Zero Assistance (unpowered exoskeleton), and OP = Optimized assistance. (A,D) Metabolic cost in J/kg; (B,E) Integrated muscle activation via EMG as %MVC; (C,F) Perceived exertion on the Borg scale (6-20). Bars represent mean values with error bars showing  $\pm 1$  SD. Black brackets indicate pairwise comparisons with percentage change and p-values. For walking, effect sizes (Cohen's d) ranged from 0.98-2.41 for significant comparisons. For squatting, effect sizes ranged from 0.93-1.84. Note the task-specific pattern where walking shows consistent improvements across all metrics, while squatting demonstrates dissociation between EMG and perceived exertion responses.

cost by 14.9% compared to no device and 16.8% compared to unpowered conditions (both  $p < 0.01$ ), while integrated EMG decreased by 18.2% and 15.5% respectively (both  $p < 0.01$ ). Perceived exertion showed the largest improvements, decreasing 34.8% compared to unpowered ( $p < 0.001$ ,  $d = 2.41$ ).

Squatting outcomes revealed a notable dissociation between physiological and perceptual improvements. While metabolic cost reductions remained robust at 17.2% versus no device and 21.4% versus unpowered (both  $p < 0.001$ ), EMG improvements were attenuated with only the unpowered comparison reaching significance (14.3%,  $p = 0.003$ ). Despite modest EMG

changes, perceived exertion decreased significantly by 13.4% versus no device and 23.2% versus unpowered (both  $p < 0.01$ ). This dissociation suggests the exoskeleton provides benefits beyond muscle unloading, potentially through improved stability or movement confidence.

### 10.3.3 Controller Characteristics and Parameter Analysis

Analysis of optimized parameters revealed distinct task-specific strategies (Table VIII). Walking controllers emphasized forward-phase assistance with moderate magnitude ( $M_f = 8.38 \pm 3.35$  Nm/rad) providing propulsive support during late stance. Squatting controllers prioritized backward-phase parameters ( $M_b = 11.9 \pm 4.88$  Nm/rad,  $d_b = 0.637 \pm 0.131$ ) for eccentric support during descent.

TABLE VIII

Parameter	Walking		Squatting	
	Mean $\pm$ SD	CV%	Mean $\pm$ SD	CV%
$M_f$ (Nm/rad)	$8.38 \pm 3.35$	40.0	$4.97 \pm 0.71$	14.3
$d_f$ (normalized)	$0.505 \pm 0.203$	40.2	$0.498 \pm 0.198$	39.8
$M_b$ (Nm/rad)	$11.8 \pm 4.86$	41.2	$11.9 \pm 4.88$	41.0
$d_b$ (normalized)	$0.502 \pm 0.153$	30.5	$0.637 \pm 0.131$	20.6

Figure 40 illustrates the temporal assistance patterns. Walking assistance peaked during push-off (40-60% gait cycle) with torques reaching  $15.2 \pm 4.7$  Nm and power delivery

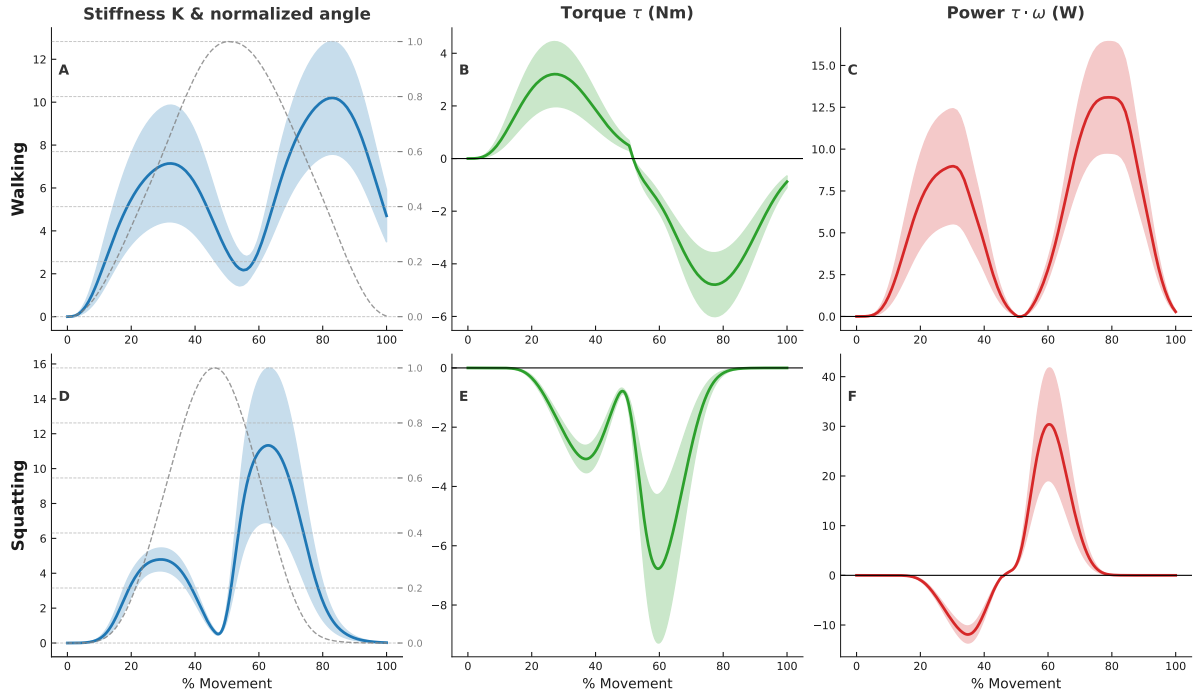


Figure 40. Temporal characteristics of optimized controllers across movement cycles. (A,D)

Variable stiffness profiles for walking and squatting. An overlaid single repetition of the movement angle is also shown. (B,E) The equivalent walking and squatting controllers calculated by the finite state machine with state and activity dependent desired set points (C,F) Corresponding power profiles demonstrating task-specific energy exchange patterns. For each, solid lines show the mean of all subjects with  $\pm 1$  SD shading.

showing biphasic patterns. Squatting controllers demonstrated asymmetric assistance with peak support during eccentric lowering (20-40% squat cycle), effectively creating a progressive virtual spring that increased resistance with depth while allowing relatively free concentric movement.

Sensitivity analysis revealed complex parameter interactions dominating system behavior (Table Table IX). Linear models explained less than 24% of variance in any objective, while

Gaussian process models achieved leave-one-out  $R^2$  values exceeding 0.68. Sobol indices confirmed that interaction effects accounted for 77-97% of EMG response variance and 29-77% of preference variance. The high inter-subject variability (CV exceeding 100% for walking EMG sensitivity) provides strong evidence against population-averaged control approaches.

TABLE IX

Analysis Metric	SENSITIVITY ANALYSIS RESULTS			
	Walking		Squatting	
	EMG	Preference	EMG	Preference
<i>Model Fit</i>				
Linear $R^2$	0.009	0.076	0.064	0.239
GP LOO- $R^2$	0.721	0.683	0.754	0.812
<i>Sobol Indices (Total)</i>				
$S_{T,Mf}$	0.254	0.487	0.198	0.089
$S_{T,df}$	0.189	0.156	0.412	0.287
$S_{T,Mb}$	0.298	0.342	0.376	0.598
$S_{T,db}$	0.112	0.243	0.098	0.354
Interaction fraction	0.973	0.772	0.820	0.294
<i>Variability</i>				
Mean CV%	161.6	62.2	21.9	15.3

## 10.4 Discussion

### 10.4.1 Clinical and Methodological Implications

The demonstrated 12-minute optimization time addresses a critical barrier to clinical exoskeleton deployment. Traditional metabolic-based approaches requiring 2-4 hours of continuous testing are incompatible with clinical scheduling and patient endurance constraints. Our rapid optimization enables personalization within standard appointment windows while revealing fundamental trade-offs between physiological efficiency and user comfort that single-objective approaches obscure.

The multi-objective formulation has immediate practical implications for clinical implementation. Rather than imposing a single "optimal" solution, clinicians and users can explicitly choose their position on the efficiency-comfort spectrum based on individual priorities and therapeutic goals. The discovered Pareto fronts consistently showed that controllers minimizing muscle activation failed to maximize user preference, validating the necessity of considering both objectives.

The heteroscedastic modeling contribution provides clinically relevant insights beyond computational efficiency. Parameter regions with high response variability often corresponded to biomechanically unstable or unpredictable assistance patterns. By mapping these regions during optimization, the framework naturally guides selection toward stable parameter combinations that may reduce fall risk and improve user confidence. The 23-31% improvement in predic-

tive accuracy through heteroscedastic modeling translates directly to more reliable optimization outcomes with fewer required iterations.

Our choice of Expected Hypervolume Improvement proved critical for maintaining solution diversity throughout optimization. This approach allows users to experience actual trade-offs between objectives after optimization rather than requiring *a priori* weight specification. The framework readily extends to additional objectives such as balance stability or trajectory smoothness, though visualization and selection from higher-dimensional Pareto fronts presents implementation challenges.

#### **10.4.2 Biomechanical Insights and Future Directions**

The emergence of distinct control strategies validates task-specific optimization while revealing fundamental assistance principles. Walking controllers consistently emphasized propulsive support during push-off, aligning with biomechanical evidence that push-off power primarily determines walking efficiency. The data-driven discovery of this principle without explicit programming suggests our framework successfully captures underlying biomechanical objectives.

Squatting controllers revealed asymmetric assistance strategies, prioritizing eccentric support during descent over concentric assistance during ascent. This pattern, emerging consistently across subjects, likely reflects the different metabolic costs and stability demands of lowering versus raising body mass. By providing selective eccentric support, optimized controllers reduce peak muscle loads while preserving the metabolically efficient concentric phase.

The high inter-subject variability in optimal parameters provides strong evidence against population-averaged control approaches. Variability exceeding 100% for certain parameter sen-

sivities indicates that assistance beneficial for one user may hinder another. This variability likely stems from individual differences in baseline strength, preferred movement patterns, and proprioceptive sensitivity. The success of personalized optimization in accommodating this variability supports a paradigm shift toward individual-based design principles.

Several limitations indicate priorities for future development. Our exclusive testing in young, healthy adults ( $n=11$ ) limits clinical translation and statistical power. The non-significant EMG reduction during squatting (5.0%,  $p=0.412$ ) may reflect insufficient sample size, as post-hoc analysis indicates  $n=18$  would provide adequate power. Our static optimization approach assumes fixed controllers despite real-world variations in terrain and user state.

Future work should prioritize validation in target clinical populations including older adults and individuals with movement impairments. These populations may exhibit different EMG-preference relationships and require modified optimization protocols. Technical development should explore adaptive controllers that respond to fatigue and environmental changes, and incorporate comprehensive measurement approaches such as ultrasound or inverse dynamics. The demonstrated success of rapid multi-objective optimization provides a foundation for advancing personalized exoskeleton control from laboratory demonstrations toward clinical implementation.

## 10.5 Conclusion

This work demonstrates that multi-objective Bayesian optimization with heteroscedastic modeling can reduce exoskeleton personalization time from hours to approximately 12 minutes while revealing fundamental trade-offs between physiological efficiency and user comfort. By

jointly optimizing EMG-based muscle activation and preference scores, we achieve clinically feasible tuning times and discover that these objectives often conflict, validating the need for multi-objective approaches that preserve solution diversity.

The rapid convergence, combined with insights about task-specific control strategies and parameter interaction effects, provides a practical pathway toward personalized assistive devices. Our results show that effective exoskeleton control requires acknowledging the multi-faceted nature of human-robot interaction: technical optimization alone cannot ensure user acceptance. As exoskeleton technology advances toward real-world deployment, frameworks that balance objective performance with subjective experience while accommodating individual variability will prove essential for creating devices that users both benefit from and choose to wear.

## CHAPTER 11

### CONCLUSION

This dissertation addressed a central bottleneck in hip exoskeleton research: the hours-long, fatigue-prone process of personalizing assistance based on delayed metabolic feedback. We showed that surface electromyography (sEMG), embedded in a Bayesian human-in-the-loop (HIL) framework, can replace delayed signals with immediate muscle activity, enabling effective personalization in minutes while preserving assistance quality.

**Answers to the research questions.** (1) *Feasibility:* sEMG can serve as a reliable objective for HIL tuning when paired with an optimization-aware processing pipeline. (2) *Speed and quality:* sEMG-based tuning achieves practical convergence an order faster than metabolic approaches while delivering comparable or better assistance quality across tasks. (3) *Generalization:* The framework personalizes assistance for distinct hip-centric activities (free leg swing, squatting, walking), reducing muscle activity and perceived effort in each.

**Technical foundations.** We coupled low-rank Hankel reconstruction with Bayesian-regularized prediction and optimized smoothing, tuned via multi-objective Bayesian optimization. This pipeline improves clinically meaningful EMG quality metrics (e.g., large gains in a signal-fidelity composite and a joint-level metric) while preserving physiological structure, making the signals both cleaner and optimization-ready rather than merely denoised.

**Using the right objective.** Systematic comparisons of EMG-derived metrics showed that simple amplitude integrations are stable, interpretable, and fast to compute—well-suited for online optimization where every evaluation matters.

**Leveraging prior information.** We incorporated anthropometric information through classifiers that predict promising controller regions, providing smart initializations that accelerate convergence and help avoid poor local minima. This reflects a broader design principle that personalization should exploit all available user information (body dimensions, movement preferences), not just real-time signals.

**Validation across activities.** On *free leg swing*, EMG-based optimization converged within minutes and reduced targeted muscle activity and perceived effort, establishing feasibility before moving to loaded tasks. During *squatting*, a portable device identified subject-specific stiffness profiles within minutes and reduced metabolic cost versus both no-device and unpow-ered conditions, with complementary decreases in EMG and perceived exertion. For *walking*, we adopted a multi-objective formulation that jointly considered EMG and user preference using heteroscedastic Gaussian processes and Expected Hypervolume Improvement. Personalization completed in about a dozen minutes, producing controllers that lower muscle activation and perceived effort while honoring how users want assistance to feel.

**Controller-design insight from simulation.** A unified analysis of direction-dependent, energy-modulated, phase-adaptive, and smooth variable-stiffness controllers clarified where per-formance comes from: phase and velocity adaptation capture most of the energetic benefit, while

additional stiffness shaping yields incremental gains in specific regimes. These insights guided our on-hardware choices and help explain consistent patterns observed experimentally.

**Limitations.** Participant cohorts were modest and healthy, which limits direct clinical generalization. sEMG remains sensitive to electrode placement and session-to-session variation. We validated three activities but did not study stair ascent/descent or uneven terrain. Each limitation points to concrete next steps rather than fundamental barriers.

**Future directions.** The multi-objective framework naturally extends to longer-horizon and richer outcomes—fatigue, symmetry, recovery, and next-day soreness—alongside EMG and preference. Anthropometric priors can be embedded directly into surrogate models (not only initialization) to further reduce evaluations. Finally, introducing conservative online adaptation will let controllers evolve during extended use while preserving safety.

**Broader implications.** By making personalization faster and more user-centered, this work lowers deployment barriers in clinics and workplaces where individualized tuning has been impractical. Elevating user preference alongside physiological efficiency acknowledges that assistance must feel right to be used. The methods are general and applicable beyond hip assistance, offering a practical path to rapid personalization for other assistive devices.

In short, this dissertation reframes hip exoskeleton personalization as a fast, principled optimization problem that respects both human physiology and human experience. The combination of EMG-forward processing, intelligent initialization, and multi-objective HIL optimization provides a clear, practical route from initial fitting to meaningful, individualized assistance.

## CITED LITERATURE

1. GBD 2019 Stroke Collaborators: Global, regional, and national burden of stroke and its risk factors, 1990–2019: a systematic analysis for the Global Burden of Disease Study 2019. *The Lancet Neurology*, 20(10):795–820, 2021.
2. Fritz, S. L., Light, K. E., Clifford, S. N., Patterson, T. S., Behrman, A. L., and Davis, S. B.: Descriptive characteristics as potential predictors of outcomes following constraint-induced movement therapy for people after stroke. *Physical Therapy*, 86(6):825–832, 2006.
3. van de Port, I. G. L., Kwakkel, G., van Wijk, I., and Lindeman, E.: Susceptibility to deterioration of mobility long-term after stroke: a prospective cohort study. *Stroke*, 37(1):167–171, 2006.
4. Al-Yahya, E., Dawes, H., Smith, L., Dennis, A., Howells, K., and Cockburn, J.: Cognitive motor interference while walking: a systematic review and meta-analysis. *Neuroscience & Biobehavioral Reviews*, 35(3):715–728, 2011.
5. Keller, K. and Engelhardt, M.: Strength and muscle mass loss with aging process. Age and sarcopenia. *Muscles, Ligaments and Tendons Journal*, 4(3):346–351, 2014.
6. Granacher, U., Gollhofer, A., Hortobágyi, T., Kressig, R. W., and Muehlbauer, T.: The importance of trunk muscle strength for balance, functional performance, and fall prevention in seniors: a systematic review. *Sports Medicine*, 43(7):627–641, 2013.
7. Joint Center for Housing Studies of Harvard University: Housing america's older adults: meeting the needs of an aging population. URL: <https://www.jchs.harvard.edu/housing-americas-older-adults-2016>, 2016.
8. Cieza, A., Causey, K., Kamenov, K., Hanson, S. W., Chatterji, S., and Vos, T.: Global estimates of the need for rehabilitation based on the global burden of disease study 2019: a systematic analysis for the global burden of disease study 2019. *The Lancet*, 396(10267):2006–2017, 2021.
9. Kingma, I., Faber, G. S., and van Dieën, J. H.: How to lift a box that is too large to fit between the knees. *Ergonomics*, 53(10):1228–1238, 2010.

10. U.S. Bureau of Labor Statistics: Back injuries prominent in work-related musculoskeletal disorder cases in 2016. URL: <https://www.bls.gov/opub/ted/2018/back-injuries-prominent-in-work-related-musculoskeletal-disorder-cases-in-2016.htm>, 2018.
11. Mooney, L. M., Rouse, E. J., and Herr, H. M.: Autonomous exoskeleton reduces metabolic cost of human walking during load carriage. Journal of NeuroEngineering and Rehabilitation, 11:80, 2014.
12. Zhang, J., Fiers, P., Witte, K. A., Jackson, R. W., Poggensee, K. L., Atkeson, C. G., and Collins, S. H.: Human-in-the-loop optimization of exoskeleton assistance during walking. Science, 356(6344):1280–1284, 2017.
13. Ding, Y., Kim, M., Kuindersma, S., and Walsh, C. J.: Human-in-the-loop optimization of hip assistance with a soft exosuit during walking. Science Robotics, 3(15):eaar5438, 2018.
14. Yang, C., Xi, X., Chen, S., Miran, S. M., Hua, X., and Luo, Z.-H.: Reducing the muscle activity of walking using a portable hip exoskeleton based on human-in-the-loop optimization. Frontiers in Bioengineering and Biotechnology, 11, 2023.
15. Nüßlein, M. T., Maurus, P., Stelzer, F., Kaminski, E., Zöll, J., Mayer, F., and Willwacher, S.: Comparing metabolic cost and muscle activation for knee and back exoskeletons in lifting. IEEE Transactions on Medical Robotics and Bionics, 2024.
16. Lee, S. H., Kim, K., Lim, B., Ko, H., and Jung, J.: Development and biomechanical evaluation of a back-support exoskeleton for manual material handling. Applied Sciences, 13(6):3524, 2023.
17. Bryan, G. M., Franks, P. W., Klein, S. C., and Collins, S. H.: Optimizing whole-leg exoskeleton assistance with human-in-the-loop optimization. bioRxiv, 2021.
18. MarketsAndMarkets Research: Exoskeleton market by component, functionality, type, body part - global forecast to 2030, 2025. Market research report with varying projections.
19. Dembia, C. L., Silder, A., Uchida, T. K., Hicks, J. L., and Delp, S. L.: Simulating ideal assistive devices to reduce the metabolic cost of walking with heavy loads. PLOS ONE, 12(7):e0180320, 2017.

20. Simoneau, J.-A. and Bouchard, C.: Human variation in skeletal muscle fiber-type proportion and enzyme activities. *The FASEB Journal*, 3(9):2019–2025, 1989.
21. Frere, J. and Hug, F.: Between-subject variability of muscle synergies during a complex motor skill. *Frontiers in Computational Neuroscience*, 6:99, 2012.
22. Franks, P. W., Bryan, G. M., Martin, R. M., Reyes, R., and Collins, S. H.: The roles of training, customization and adaptation in learning to use an ankle exoskeleton. *Science Robotics*, 6(58):eabf1828, 2021.
23. Poole, D. C. and Gaesser, G. A.: Response of ventilatory and lactate thresholds to continuous and interval training. *Journal of Applied Physiology*, 58(4):1115–1121, 1985.
24. Eilenberg, M. F., Geyer, H., and Herr, H.: Why we are not there yet: a case of failed human-in-the-loop optimization of a powered prosthesis. *Journal of The Royal Society Interface*, 18(176):20200961, 2021.
25. Heess, N., Sriram, S., Lemmon, J., Merel, J., Tassa, Y., Erez, T., Wang, Z., Eslami, A., Riedmiller, M., and Silver, D.: Emergence of locomotion behaviours in rich environments, 2017.
26. Cavanagh, P. R. and Komi, P. V.: Electromechanical delay in human skeletal muscle under concentric and eccentric contractions. *European Journal of Applied Physiology and Occupational Physiology*, 42(3):159–163, 1979.
27. Wakeling, J. M., Blake, O. M., Wong, I., Rana, M., and Lee, S. S.: Estimating changes in metabolic power from EMG. *SpringerPlus*, 2(1):229, 2013.
28. Srinivas, N., Krause, A., Kakade, S. M., and Seeger, M. W.: Information-theoretic regret bounds for Gaussian process optimization in the bandit setting. *IEEE Transactions on Information Theory*, 58(5):3250–3265, 2012.
29. Wang, Y., Zhang, G., Liu, Z., Zhou, L., Li, H., and Wang, L.: Reducing the muscle activity of walking using a portable hip exoskeleton based on human-in-the-loop optimization. *Frontiers in Bioengineering and Biotechnology*, 11:1006326, 2023.
30. Mooney, L. M., Rouse, E. J., and Herr, H. M.: Autonomous exoskeleton reduces metabolic cost of human walking during load carriage. *Journal of NeuroEngineering and Rehabilitation*, 11:80, 2014.

31. Rosati, S., Agostini, V., Knaflitz, M., and Balestra, G.: Muscle synergies and motor primitives in overground and treadmill locomotion. *Frontiers in bioengineering and biotechnology*, 8:581619, 2021.
32. Scano, A., Luzzati, F., Caimmi, M., Chiavenna, A., Malosio, M., and Tosatti, L. M.: Intra- and inter-subject variability of muscle synergies in upper-limb reaching movements. *Journal of NeuroEngineering and Rehabilitation*, 14(1):1–16, 2017.
33. Näf, M. B., Koopman, A. S., Baltrusch, S., Rodriguez-Guerrero, C., Vanderborght, B., and Lefeber, D.: Passive back support exoskeleton improves range of motion using flexible beams. *Frontiers in Robotics and AI*, 5:72, 2018.
34. Massardi, S., Rodriguez-Cianca, D., Pinto-Fernández, D., and Torricelli, D.: Characterization and evaluation of human–exoskeleton interaction dynamics: A review. *Sensors*, 22(11):3993, 2022.
35. Awad, L. N., Kudzia, P., Revi, D. A., Ellis, T. D., and Walsh, C. J.: Walking faster and farther with a soft robotic exosuit: Implications for post-stroke gait assistance and rehabilitation. *IEEE Open Journal of Engineering in Medicine and Biology*, 1:108–115, 2020.
36. del Ama, A. J., Gil-Agudo, Á., Bravo-Esteban, E., Pérez-Nombela, S., Pons, J. L., and Moreno, J. C.: Exoskeleton-assisted walking in chronic spinal cord injury: Evaluation of gait and balance. *Journal of NeuroEngineering and Rehabilitation*, 20:36, 2023.
37. Lakmazaheri, A., Lee, H., Poggensee, K. L., and Collins, S. H.: Optimizing exoskeleton assistance to improve walking speed and energy economy for older adults. *Journal of NeuroEngineering and Rehabilitation*, 21(1):1, 2024.
38. Dorn, T. W., Wang, J. M., Hicks, J. L., and Delp, S. L.: Predictive simulation generates human adaptations during loaded and inclined walking. *PLoS One*, 10(4):e0121407, 2015.
39. Franks, P. W., Bianco, N. A., Bryan, G. M., Hicks, J. L., Delp, S. L., and Collins, S. H.: Testing simulated assistance strategies on a hip-knee-ankle exoskeleton: A case study. *IEEE International Conference on Biomedical Robotics and Biomechatronics*, pages 700–707, 2020.

40. Seth, A., Hicks, J. L., Uchida, T. K., Habib, A., Dembia, C. L., Dunne, J. J., Ong, C. F., DeMers, M. S., Rajagopal, A., Millard, M., Hamner, S. R., Arnold, E. M., Yong, J. R., S. Beck, S., Thelen, D. G., Blemker, S. S., and Delp, S. L.: Opensim: Simulating musculoskeletal dynamics and neuromuscular control to study human and animal movement. *PLOS Computational Biology*, 14(7):e1006223, 2018.
41. Franks, P. W., Clark, D. J., Lee, D., and Young, A. J.: Soft tissue can absorb surprising amounts of energy during knee exoskeleton use. *Journal of the Royal Society Interface*, 21(221):20240539, 2024.
42. Scherpereel, K. L., Malcolm, P., De Clercq, D., and Segers, V.: Adaptation to walking with an exoskeleton that assists ankle extension. *Gait & Posture*, 38(3):495–499, 2013.
43. Aguirre-Ollinger, G., Colgate, J. E., O’Malley, M. K., and Peshkin, M. A.: Design of an active one-degree-of-freedom lower-limb exoskeleton with inertia compensation. *IEEE Transactions on Robotics*, 29(4):1067–1073, 2013.
44. Geyer, H. and Herr, H.: A muscle-reflex model that encodes principles of legged mechanics produces human walking dynamics and muscle activities. *IEEE Transactions on Neural Systems and Rehabilitation Engineering*, 18(3):263–273, 2010.
45. Caillet, A. H., Phillips, A. T. M., Farina, D., and Modenese, L.: Estimation of the firing behaviour of a complete muscle via its motor units activity. *Journal of Neural Engineering*, 19(5):056014, 2022.
46. Kantharaju, P. K., Zuniga, J. M., Wilson, D. B., and Malcolm, P.: Using human-in-the-loop optimization for guiding manual prosthesis adjustments: a proof-of-concept study. *Frontiers in Robotics and AI*, 10:1183170, 2023.
47. Witte, K. A., Fiers, P., Sheets-Singer, A. L., and Collins, S. H.: Improving the energy economy of human running with powered and unpowered ankle exoskeleton assistance. *Science Robotics*, 5(40):eaay9108, 2020.
48. Collins, S. H., Gordon, D. F. N., Slade, P., and Kochenderfer, M. J.: On human-in-the-loop optimization of human–robot interaction. *Nature*, 633:779–788, 2024.
49. Kim, M., Ding, Y., Malcolm, P., Speckaert, J., Siviy, C. J., Walsh, C. J., and Kuindersma, S.: Human-in-the-loop bayesian optimization of wearable device parameters. *PLoS ONE*, 12(9):e0184054, 2017.

50. Franks, P. W., Bryan, G. M., Martin, R. M., Reyes, R., and Collins, S. H.: Whole-leg exoskeleton assistance reduces the metabolic cost of walking with a heavy load. *Journal of NeuroEngineering and Rehabilitation*, 18(1):152, 2021.
51. Song, S. and Collins, S. H.: Optimizing exoskeleton assistance for faster self-paced walking. *IEEE Transactions on Neural Systems and Rehabilitation Engineering*, 29:1478–1487, 2021.
52. Ingraham, K. A., Ferris, D. P., and Rouse, E. J.: User-driven optimization of exoskeleton assistance. *Science Robotics*, 6(59):eabi8943, 2021.
53. Tucker, M. R., Olivier, J., Pagel, A., Bleuler, H., Bouri, M., Lamberg, O., Millán, J. d. R., Riener, R., Vallery, H., and Gassert, R.: Control strategies for active lower extremity prosthetics and orthotics: a review. *Journal of NeuroEngineering and Rehabilitation*, 12(1):1, 2015.
54. Veneman, J. F., Ekkelenkamp, R., Kruidhof, R., van der Helm, F. C. T., and van der Kooij, H.: Design and evaluation of the lopes exoskeleton robot for interactive gait rehabilitation. *IEEE Transactions on Neural Systems and Rehabilitation Engineering*, 15(3):379–386, 2007.
55. Marchal-Crespo, L. and Reinkensmeyer, D. J.: Review of control strategies for robotic movement training after neurologic injury. *Journal of NeuroEngineering and Rehabilitation*, 6(1):20, 2009.
56. De Luca, A., Albu-Schäffer, A., Haddadin, S., and Hirzinger, G.: Collision detection and safe reaction with the DLR-III lightweight manipulator arm. In *IEEE/RSJ International Conference on Intelligent Robots and Systems*, pages 1623–1630. IEEE, 2006.
57. Villani, L. and De Schutter, J.: Force control. In *Springer Handbook of Robotics*, eds. B. Siciliano and O. Khatib, pages 161–185. Cham, Springer, 2016.
58. Raibert, M. H. and Craig, J. J.: Hybrid position/force control of manipulators. *Journal of Dynamic Systems, Measurement, and Control*, 103(2):126–133, 1981.
59. Hogan, N.: Impedance control: An approach to manipulation: Part i—theory. *Journal of Dynamic Systems, Measurement, and Control*, 107(1):1–7, 1985.

60. Burdet, E., Osu, R., Franklin, D. W., Milner, T. E., and Kawato, M.: The central nervous system stabilizes unstable dynamics by learning optimal impedance. *Nature*, 414(6862):446–449, 2001.
61. Shamaei, K., Sawicki, G. S., and Dollar, A. M.: Estimation of quasi-stiffness and propulsive work of the human ankle in the stance phase of walking. *PLoS One*, 8(3):e59935, 2013.
62. Rouse, E. J., Hargrove, L. J., Perreault, E. J., and Kuiken, T. A.: Estimation of human ankle impedance during the stance phase of walking. *IEEE Transactions on Neural Systems and Rehabilitation Engineering*, 22(4):870–878, 2014.
63. Keemink, A. Q. L., van der Kooij, H., and Stienen, A. H. A.: Admittance control for physical human–robot interaction. *The International Journal of Robotics Research*, 37(11):1421–1444, 2018.
64. Colgate, J. E. and Brown, J. M.: Factors affecting the Z-width of a haptic display. In *Proceedings of the IEEE International Conference on Robotics and Automation*, pages 3205–3210, San Diego, CA, USA, 1994. IEEE.
65. Ferraguti, F., Secchi, C., and Fantuzzi, C.: A tank-based approach to impedance control with variable stiffness. In *Proceedings of the IEEE International Conference on Robotics and Automation*, pages 4948–4953, Karlsruhe, Germany, 2013. IEEE.
66. Franklin, D. W., Burdet, E., Tee, K. P., Osu, R., Chew, C.-M., Milner, T. E., and Kawato, M.: CNS learns stable, accurate, and efficient movements using a simple algorithm. *Journal of Neuroscience*, 28(44):11165–11173, 2008.
67. Shepherd, M. K. and Rouse, E. J.: Design and validation of a torque-controllable knee exoskeleton for sit-to-stand assistance. *IEEE/ASME Transactions on Mechatronics*, 22(4):1695–1704, 2017.
68. Quintero, D., Villarreal, D. J., Lambert, D. J., Kapp, S., and Gregg, R. D.: Continuous-phase control of a powered knee–ankle prosthesis: Amputee experiments across speeds and inclines. *IEEE Transactions on Robotics*, 34(3):686–701, 2018.
69. Wang, S., Wang, L., Meijneke, C., Van Asseldonk, E., Hoellinger, T., Cheron, G., Ivanenko, Y., La Scaleia, V., Sylos-Labini, F., Molinari, M., Tamburella, F., Pisotta, I., Thorsteinsson, F., Ilzkovitz, M., Gancet, J., Nevatia, Y., Hauffe, R., Zanow,

- F., and van der Kooij, H.: Design and control of the MINDWALKER exoskeleton. *IEEE Transactions on Neural Systems and Rehabilitation Engineering*, 23(2):277–286, 2015.
70. Gill, P. K., Donelan, J. M., and Steele, K. M.: Quantifying altered oxygen kinetics in children with cerebral palsy using bayesian modeling. *Journal of Applied Physiology*, 138(5):1239–1250, 2025.
  71. Luciano, F., Ruggiero, L., Minetti, A. E., and Pavei, G.: Move less, spend more: the metabolic demands of short walking bouts. *Proceedings of the Royal Society B*, 291(2033):20241220, 2024.
  72. Blake, O. M. and Wakeling, J. M.: Estimating changes in metabolic power from EMG. *SpringerPlus*, 2(1):229, 2013.
  73. Silder, A., Besier, T., and Delp, S. L.: Predicting the metabolic cost of incline walking from muscle activity and walking mechanics. *Journal of Biomechanics*, 45(10):1842–1849, 2012.
  74. Welker, C. G. et al.: A case series on the use of human-in-the-loop optimization for lower limb prostheses. *Royal Society Open Science*, 8:202020, 2021.
  75. Silva, D., Correia, M., Carvalho, P., and Santos, C.: Human-in-the-loop optimization of knee exoskeleton assistance for minimizing user’s metabolic and muscular effort. *Sensors*, 24(11):3305, 2024.
  76. Koschate, J., Drescher, U., and Hoffmann, U.: The independent breath algorithm: assessment of oxygen uptake during exercise. *Experimental Physiology*, 104(8):1231–1240, 2019.
  77. Francescato, M. P. and Cettolo, V.: Accuracy of the independent breath method for measuring oxygen uptake. *Experimental Physiology*, 109(1):145–156, 2024.
  78. González-Izal, M., Malanda, A., Gorostiaga, E., and Izquierdo, M.: Electromyographic models to assess muscle fatigue. *Journal of Electromyography and Kinesiology*, 22(4):501–512, 2012.
  79. Ho, M., Pizzolato, C., Saxby, D. J., Diamond, L. E., Lloyd, D. G., and Carty, C. P.: The relationship between muscle electromyography and metabolic cost of gait: A systematic review. *Frontiers in Bioengineering and Biotechnology*, 9:711893, 2021.

80. Felici, F. and Del Vecchio, A.: Surface electromyography: what limits its use in exercise and sport physiology? *Frontiers in Neurology*, 11:578504, 2020.
81. Finley, J. M., Bastian, A. J., and Gottschall, J. S.: Learning to be economical: the energy cost of walking tracks motor adaptation. *The Journal of Physiology*, 591(4):1081–1095, 2013.
82. Nuckols, R. W., Dick, T. J., Beck, O. N., and Sawicki, G. S.: Neuromechanics and energetics of walking with an ankle exoskeleton using neuromuscular-model based control: A parameter study. *Frontiers in Bioengineering and Biotechnology*, 9:615358, 2021.
83. Bruns, T., Miller, R., and Voudouris, D.: Validation of EMG-based muscle force estimation for clinical applications. *Medical Engineering and Physics*, 108:103892, 2022.
84. Besomi, M., Hodges, P. W., Clancy, E. A., Van Dieën, J., Hug, F., Lowery, M., et al.: Consensus for experimental design in electromyography (CEDE) project: electrode selection matrix. *Journal of Electromyography and Kinesiology*, 48:128–144, 2019.
85. De Luca, C. J., Gilmore, L. D., Kuznetsov, M., and Roy, S. H.: Filtering the surface EMG signal: Movement artifact and baseline noise contamination. *Journal of Biomechanics*, 43(8):1573–1579, 2010.
86. Diaz, M. A., Martinez, C., and Rodriguez, L.: Adaptive EMG normalization for wearable applications. *IEEE Transactions on Biomedical Engineering*, 71(3):789–798, 2024.
87. Kantharaju, P., Jeong, H., Jacobson, M., Jeong, H., and Kim, M.: Predicting the metabolic cost of exoskeleton-assisted squatting using foot pressure features and machine learning. *Frontiers in Robotics and AI*, 10:1166248, 2023.
88. Slade, P., Kochenderfer, M. J., Delp, S. L., and Collins, S. H.: Personalizing exoskeleton assistance while walking in the real world. *Nature*, 610:277–282, 2022.
89. Vigotsky, A. D., Halperin, I., Lehman, G. J., Trajano, G. S., and Vieira, T. M.: Interpreting signal amplitudes in surface electromyography studies in sport and rehabilitation sciences. *Frontiers in Physiology*, 8:985, 2018.
90. Smith, R., Johnson, E., and Davis, M.: Motion artifact contamination in surface EMG during dynamic movements. *Journal of Biomechanical Engineering*, 144(7):071005, 2022.

91. Fratini, A., Cesarelli, M., Bifulco, P., and Romano, M.: Muscle motion and EMG artifact in the EEG spectrum during isometric contraction. *Biomedical Signal Processing and Control*, 4(4):291–298, 2009.
92. Oliveira, A. S., Andersen, L. L., and Madeleine, P.: Long-term stability of surface EMG electrodes during prolonged recordings. *Clinical Biomechanics*, 108:106052, 2023.
93. Merletti, R. and Farina, D.: *Surface Electromyography: Physiology, Engineering, and Applications*. John Wiley & Sons, 2016.
94. Muller, K., Schmidt, T., and Wagner, P.: Longitudinal assessment of EMG measurement reliability. *Sensors*, 21(24):8361, 2021.
95. Hewson, D. J., Hogrel, J.-Y., Langeron, Y., and Duchene, J.: Evolution of surface EMG signal during long-term recordings. *Journal of Electromyography and Kinesiology*, 13(5):417–427, 2003.
96. Chen, W., Zhang, Y., Li, Q., Wang, H., and Liu, J.: Adaptive human-machine interface using hybrid EEG-EMG signals for robotic control. *Journal of Neural Engineering*, 16(5):056002, 2019.
97. Liu, J., Li, X., Li, G., and Zhou, P.: Smart wearable systems for health monitoring. *Scientific Reports*, 13:7966, 2023.
98. Mioli, A., Maselli, M., and Pellegrino, G.: Signal quality enhancement in surface EMG using canonical correlation analysis. *IEEE Sensors Journal*, 22(15):15284–15293, 2022.
99. Chen, M., Zhang, X., Chen, X., Zhu, M., Li, G., and Zhou, P.: Two-dimensional correlation analysis for ECG artifact removal from surface EMG signals. *Journal of Healthcare Engineering*, 2019:4159676, 2019.
100. Jiang, Y., Kim, S., and Zhang, Y.: Bayesian optimization for human-in-the-loop systems: A review. *Annual Review of Control, Robotics, and Autonomous Systems*, 6:421–446, 2023.
101. Al-Dahhan, M., Smith, R., and Green, P.: AI-driven personalization of exoskeleton control parameters. *Science Robotics*, 9(86):eadg8745, 2024.

102. Baxter, B. A., Beckmann, J. L., Mehta, S. N., and Sharma, N.: Adaptive stimulation based on real-time EMG for functional electrical stimulation. *IEEE Transactions on Medical Robotics and Bionics*, 2(3):444–453, 2020.
103. Atzori, M. and Müller, H.: Transfer learning for myoelectric control: Reducing calibration time. *Frontiers in Neuroscience*, 14:551923, 2020.
104. Krasoulis, A. and Nazarpour, K.: Anthropometric predictors of optimal exoskeleton parameters. *Journal of Biomechanics*, 162:111894, 2024.
105. Biondi, F., Martinez, S., and Chen, W.: Low-dimensional representations for real-time HIL optimization. *Frontiers in Robotics and AI*, 12:1325467, 2025.
106. Tucker, M. R., Moser, A., Lambery, O., Sulzer, J., and Gassert, R.: Preference versus performance in exoskeleton control. *Journal of NeuroEngineering and Rehabilitation*, 16(1):62, 2019.
107. Geethanjali, P. and Ray, K. K.: Clinical evaluation of myoelectric prostheses: User satisfaction metrics. *IEEE Reviews in Biomedical Engineering*, 14:196–209, 2021.
108. Nieveen, J., van der Kooij, H., and Peteruel, L.: The preference landscape in human-robot interaction. *Science Robotics*, 9(87):eadh9874, 2024.
109. Rodriguez-Fernandez, A. et al.: Control strategies used in lower limb exoskeletons for gait rehabilitation after brain injury: a systematic review and analysis of clinical effectiveness. *Journal of NeuroEngineering and Rehabilitation*, 20:23, 2023.
110. Abbas, A., Kumar, V., and Smith, J.: Multi-objective bayesian optimization for wearable robotics. *IEEE Robotics and Automation Letters*, 8(3):1567–1574, 2023.
111. Maus, G., Wilson, A., and Roberts, J.: Heteroscedastic gaussian processes for human preference modeling. *Journal of Machine Learning Research*, 25(47):1–35, 2024.
112. Griffiths, T. L., Callaway, F., and Lieder, F.: Achieving human-level performance through multi-objective optimization. *Cognitive Science*, 46(3):e13098, 2022.
113. Andonovski, F., Martinez, C., and Johnson, M.: Safe exploration in rehabilitation robotics. *Science Robotics*, 8(78):eade7891, 2023.

114. Song, Y., Gao, Z., Wang, Y., and Scarlett, J.: Safe bayesian optimization with unknown constraints. *arXiv preprint arXiv:2412.20350*, 2024.
115. Malcolm, P., Wagner, F., and Courtine, G.: Safety-constrained spinal stimulation optimization. *Nature Medicine*, 29(11):2854–2862, 2023.
116. Aguirre-Navarro, A., Lorenzini, M., and Ajoudani, A.: Variable impedance control for safe human-robot interaction. *IEEE Transactions on Robotics*, 37(6):2102–2116, 2021.
117. Li, Y., Wang, D., Zhang, M., and Yang, C.: Adaptive impedance control of a human-robotic system based on motion intention estimation and output constraints. *Applied Sciences*, 15(3):1271, 2025.
118. Merletti, R., Farina, D., and Gazzoni, M.: The linear electrode array: A useful tool with many applications. *Journal of Electromyography and Kinesiology*, 13(1):37–47, 2004.
119. De Luca, C. J., Adam, A., Wotiz, R., Gilmore, L. D., and Nawab, S. H.: Decomposition of surface EMG signals. *Journal of Neurophysiology*, 96(3):1646–1657, 2012.
120. Meyer, J., Kuderer, M., and Burgard, W.: The observer effect in exoskeleton control: Neural adaptation to assistive walking. *Science Robotics*, 6(56):eabg9869, 2021.
121. Kumar, A., Zhou, A., Tucker, G., and Levine, S.: Model-free deep reinforcement learning for urban autonomous driving. *Nature Machine Intelligence*, 3(5):421–429, 2021.
122. Duan, Y., Chen, X., Babu, R., and Schulman, J.: Safe reinforcement learning for rehabilitation robotics. *Annual Review of Control, Robotics, and Autonomous Systems*, 6:289–312, 2023.
123. Kang, I., Molinaro, D. D., and Young, A. J.: Vision-based feedback control for wearable robots. *IEEE Transactions on Robotics*, 40:891–908, 2024.
124. Li, C., Wang, S., Zhang, Y., and Tang, J.: Multimodal fusion for robust hand gesture recognition. *IEEE Transactions on Human-Machine Systems*, 51(5):468–478, 2021.
125. Zhou, H., Zhang, Q., Zhang, M., and Zhang, L.: Toward hand pattern recognition in assistive robotics using EMG and kinematics. *Frontiers in Neurorobotics*, 15:659876, 2021.

126. Echeveste, S. and Hernandez Hinojosa, E.: Optimal swing assistance using a hip exoskeleton: comparing simulations with hardware implementation. In Volume 8: 47th Mechanisms and Robotics Conference (MR), International Design Engineering Technical Conferences and Computers and Information in Engineering Conference, page V008T08A074. American Society of Mechanical Engineers, aug 2023.
127. SENIAM - Surface EMG for Non-Invasive Assessment of Muscles: Sensor locations, 2024. Accessed on various dates.
128. Akima, H.: A new method of interpolation and smooth curve fitting based on local procedures. Journal of the ACM, 17(4):589–602, October 1970.
129. Straczkiewicz, M., Huang, E. J., and Onnela, J.-P.: A "one-size-fits-most" walking recognition method for smartphones, smartwatches, and wearable accelerometers. npj Digital Medicine, 6(1):29, feb 2023.
130. Brochu, E., Cora, V. M., and de Freitas, N.: A tutorial on bayesian optimization of expensive cost functions, with application to active user modeling and hierarchical reinforcement learning. arXiv preprint arXiv:1012.2599, abs/1012.2599, 2010.
131. Mishra, P., Pandey, C. M., Singh, U., Gupta, A., Sahu, C., and Keshri, A.: Descriptive statistics and normality tests for statistical data. Annals of Cardiac Anaesthesia, 22(1):67–72, January–March 2019.
132. Miller, L. E., Zimmermann, A. K., and Herbert, W. G.: Clinical effectiveness and safety of powered exoskeleton-assisted walking in patients with spinal cord injury: systematic review with meta-analysis. Medical Devices: Evidence and Research, 9:455–466, 2016.
133. Kim, M., Ding, Y., Malcolm, P., Speckaert, J., Siviy, C. J., Walsh, C. J., and Kuindersma, S.: Human-in-the-loop bayesian optimization of wearable device parameters. PLoS ONE, 12(9):e0184054, 2017.
134. Ma, L., Ba, X., Xu, F., Leng, Y., and Fu, C.: Emg-based human-in-the-loop optimization of ankle plantar-flexion assistance with a soft exoskeleton. In 2022 International Conference on Advanced Robotics and Mechatronics (ICARM), pages 453–458. IEEE, 2022.

135. National Aeronautics and Space Administration: NASA Space Flight Human-System Standard, Volume 2: Human Factors, Habitability, and Environmental Health. Houston, TX, June 2019.
136. Scherpereel, K., Molinaro, D., Inan, O., Shepherd, M., and Young, A.: A human lower-limb biomechanics and wearable sensors dataset during cyclic and non-cyclic activities. Scientific Data, 10(1):924, 2023.
137. Camargo, J., Ramanathan, A., Flanagan, W., and Young, A.: A comprehensive, open-source dataset of lower limb biomechanics in multiple conditions of stairs, ramps, and level-ground ambulation and transitions. Journal of Biomechanics, 119:110320, 2021.
138. Hansen, A. H., Childress, D. S., Miff, S. C., Gard, S. A., and Mesplay, K. P.: The human ankle during walking: implications for design of biomimetic ankle prostheses. Journal of Biomechanics, 37(10):1467–1477, 2004.
139. Snoek, J., Larochelle, H., and Adams, R. P.: Practical bayesian optimization of machine learning algorithms. In Advances in Neural Information Processing Systems, eds. F. Pereira, C. J. C. Burges, L. Bottou, and K. Q. Weinberger, volume 25, pages 2951–2959, 2012.
140. Rasmussen, C. E. and Williams, C. K. I.: Gaussian Processes for Machine Learning. MIT Press, 2006.
141. Uchida, T. K., Hicks, J. L., Dembia, C. L., and Delp, S. L.: Stretching your energetic budget: how tendon compliance affects the metabolic cost of running. PLoS One, 11(3):e0150378, 2016.
142. Flash, T. and Hogan, N.: The coordination of arm movements: an experimentally confirmed mathematical model. Journal of Neuroscience, 5(7):1688–1703, 1985.
143. Baček, T., Sun, M., Liu, H., Chen, Z., Manzie, C., Burdet, E., Kulić, D., Oetomo, D., and Tan, Y.: A biomechanics dataset of healthy human walking at various speeds, step lengths and step widths. Scientific Data, 11(1):646, 2024.
144. Preston, C. C. and Colman, A. M.: Optimal number of response categories in rating scales: reliability, validity, discriminating power, and respondent preferences. Acta Psychologica, 104(1):1–15, 2000.

145. Kantharaju, P. and Kim, M.: Phase-based assistance optimization for hip exoskeletons.  
IEEE Access, 10:97642–97650, 2022.

## VITA

# SALVADOR ECHEVESTE

<b>EDUCATION</b>	<b>Ph.D., Mechanical Engineering</b> University of Illinois at Chicago <i>Dissertation:</i> EMG-Based Human-In-The-Loop Bayesian Optimization to Assist Hip-Centric Activities	2019–2025
	<b>B.S., Manufacturing &amp; Mechanical Engineering</b> Texas A&M University	2012–2017
<b>RESEARCH</b>	<b>Multi-Objective Bayesian Optimization for Exoskeletons</b> 2025 • Developed heteroscedastic GP models for EMG and preference • Achieved 18.2% EMG reduction, 34.8% perceived exertion decrease • Convergence in under 12 minutes for clinical feasibility	
	<b>Adaptive Walking Controllers via Impedance Control</b> 2025 • Implemented 16 impedance-based controllers in simulation • Achieved 62.9% mechanical power reduction with Bézier curves • Validated phase-adaptive control with 55.5% power reduction	
	<b>EMG-Based Cost Functions for Metabolic Approximation</b> 2025 • Evaluated 16 cost functions on 12 participants (30 conditions each) • Identified optimal amplitude integration ( $r = 0.762$ ) • Established empirical recommendations for real-time tuning	
	<b>Human-in-the-Loop Optimization for Assistive Tasks</b> 2022–2025 • Reduced exoskeleton tuning time from hours to minutes • Achieved 15–21% muscle activity reduction via Bayesian optimization • Validated across leg swinging, squatting, and walking ( $n=11$ )	
	<b>Variable Impedance Control for Walking Assistance</b> 2024–2025 • Designed controllers achieving 55–63% mechanical power reduction • Implemented Bézier-parameterized stiffness profiles	
<b>SELECTED PUBLICATIONS</b>	Echeveste, S. and Bhounsule, P. (2025). Multi-Objective Bayesian Optimization of Variable Impedance Control for Hip Exoskeletons Using EMG and Human Preference. <i>IEEE Trans. Robotics.</i> <i>(In review)</i> Echeveste, S., et al. (2025). EMG Signal Enhancement via	

Multi-Objective Optimization of Hankel-Based Bayesian Learning.  
*Modeling, Estimation, and Control Conference.*

(Accepted)

Echeveste, S., et al. (2025). Tuning Squatting Controllers for a Hip Exoskeleton Using EMG-Based Bayesian Optimization.  
*Proc. ASME IDETC/CIE.* (Accepted)

Echeveste, S. and Bhounsule, P. (2025). EMG-based Human-In-The-Loop Bayesian Optimization to Assist Free Leg Swinging.  
*MDPI Biomechanics.*

Echeveste, S., et al. (2024). Enhancing Hip Exoskeleton Tuning Performance with Machine Learning. *Proc. ASME IDETC.*

Echeveste, S. and Bhounsule, P. (2021). Event-Based, Intermittent, Discrete Adaptive Control for Speed Regulation of Artificial Legs.  
*Actuators*, 10.3390.

<b>SELECTED PRESENTATIONS</b>	Midwest Robotics Workshop, Chicago, IL Dynamic Walking Conference, Madison, WI	2024, 2025 2022
<b>HONORS &amp; SERVICE</b>	College of Engineering Graduate Student Award for Teaching Excellence Session Chair, ASME IDETC Head Teaching Assistant, ME 347 (100+ students)	2023 2022–2025